

NEW QUINOXALINE AND SELENOPHENE BASED BENZODITHIOPHENE  
BEARING CONJUGATED POLYMERS FOR PHOTOVOLTAIC  
APPLICATIONS

A THESIS SUBMITTED TO  
THE GRADUATE SCHOOL OF NATURAL AND APPLIED SCIENCES  
OF  
MIDDLE EAST TECHNICAL UNIVERSITY

BY

MERİÇ ÇALIŞKAN

IN PARTIAL FULFILLMENT OF THE REQUIREMENTS  
FOR  
THE DEGREE OF MASTER OF SCIENCE  
IN  
CHEMISTRY

DECEMBER 2019



Approval of the thesis:

**NEW QUINOXALINE AND SELENOPHENE BASED  
BENZODITHIOPHENE BEARING CONJUGATED POLYMERS FOR  
PHOTOVOLTAIC APPLICATIONS**

submitted by **MERİÇ ÇALIŞKAN** in partial fulfillment of the requirements for the degree of **Master of Science in Chemistry Department, Middle East Technical University** by,

Prof. Dr. Halil Kalıpçılar  
Dean, Graduate School of **Natural and Applied Sciences**

\_\_\_\_\_

Prof. Dr. Cihangir Tanyeli  
Head of Department, **Chemistry**

\_\_\_\_\_

Prof. Dr. Ali Çırpan  
Supervisor, **Chemistry, METU**

\_\_\_\_\_

**Examining Committee Members:**

Prof. Dr. Levent Kamil Toppare  
Chemistry, METU

\_\_\_\_\_

Prof. Dr. Ali Çırpan  
Chemistry, METU

\_\_\_\_\_

Prof. Dr. Yasemin Arslan Udum  
Technical Sciences Vocational School, Gazi University

\_\_\_\_\_

Assoc. Prof. Dr. İrem Erel Göktepe  
Chemistry, METU

\_\_\_\_\_

Assoc. Prof. Dr. Görkem Günbaş  
Chemistry, METU

\_\_\_\_\_

Date: 24.12.2019

**I hereby declare that all information in this document has been obtained and presented in accordance with academic rules and ethical conduct. I also declare that, as required by these rules and conduct, I have fully cited and referenced all material and results that are not original to this work.**

Name, Surname: Meri Çalıřkan

Signature:

## ABSTRACT

### NEW QUINOXALINE AND SELENOPHENE BASED BENZODITHIOPHENE BEARING CONJUGATED POLYMERS FOR PHOTOVOLTAIC APPLICATIONS

Çalışkan, Meriç  
Master of Science, Chemistry  
Supervisor: Prof. Dr. Ali Çırpan

December 2019, 95 pages

The current research trends have greatly focused on the development of new low band gap conjugated polymers featuring alternating donor-acceptor unities to achieve remarkable power conversion efficiencies for OPV devices. For this purpose, a series of new quinoxaline and selenophene based BDT bearing conjugated polymers namely P1, P2 and P3 were synthesized using Stille cross coupling reaction. The 2-(2-Octyldodecyl)selenophene ring was attached to 4<sup>th</sup> and 8<sup>th</sup> positions of phenyl ring in BDT to obtain donor moiety and three different quinoxaline moieties as acceptors were introduced into the BDT backbone. After completion of synthesis of D-A polymers, their structures were identified with H<sup>1</sup> NMR spectroscopy and their molecular weights were examined with GPC. Moreover, electrochemical, spectroelectrochemical kinetic and thermal studies of polymers were carried out. The photovoltaic properties and blend film morphologies of resulting polymers were also investigated. The synthesized polymers were utilized as donor segment in active layer and they were combined with PC<sub>71</sub>BM ([6,6]-phenyl C<sub>71</sub>-butyric acid methyl ester) acceptor to fabricate bulk heterojunction solar cells, that produced highest power conversion efficiencies as following: 2.36% for P1, 2.07% for P2 and 2.45% for P3 under AM 1.5 G (100 mW/cm<sup>2</sup>) conditions.

**Keywords:** Quinoxaline, benzodithiophene, bulk heterojunction solar cells, Stille cross coupling reaction

## ÖZ

### **FOTOVOLTAİK UYGULAMALAR İÇİN YENİ KİNOKSALİN VE SELENOFEN BAZLI BENZODİTİYOFEN İÇEREN KONJÜGE POLİMERLER**

Çalışkan, Meriç  
Yüksek Lisans, Kimya  
Tez Danışmanı: Prof. Dr. Ali Çırpan

Aralık 2019, 95 sayfa

Mevcut araştırma akımları OPV cihazları için kayda değer güç verimleri elde etmek için alternatif donör-akseptör içeren yeni düşük bant aralıklı konjüge polimerlerin geliştirilmesine büyük ölçüde odaklanmıştır. Bu amaçla Stille çapraz bağlanma reaksiyonu kullanılarak bir dizi yeni kinoksalin ve selenofen bazlı BDT içeren konjüge polimerler P1, P2 ve P3 sentezlendi. 2-(2-Oktildodesil) selenofen halkası, donör kısmı elde etmek için BDT'deki fenil halkasının 4. ve 8. pozisyonlarına tutturuldu ve BDT yapısına akseptör grup olarak üç farklı kinoksalin grubu eklendi. D-A polimerlerinin sentezi tamamlanmasından sonra yapıları  $H^1$  NMR spektroskopisi ile tanımlanmış ve moleküler ağırlıkları GPC ile incelenmiştir. Ayrıca, polimerlerin elektrokimyasal, spektroelettrokimyasal, kinetik ve ısıl çalışmaları yapılmıştır. Elde edilen polimerlerin fotovoltaiik özellikleri ve blend film morfolojileri de incelenmiştir. Sentezlenen polimerler, aktif katman içinde donör segmenti olarak kullanıldı ve polimerler standart AM1.5 G ( $100 \text{ mW/cm}^2$ ) koşulları altında, P1 için %2.36, P2 için %2.07 ve P3 için %2.45 şeklinde en yüksek güç dönüşüm verimi üreten yığın heterobağlantılı güneş hücrelerinin üretilmesi için PC<sub>71</sub>BM ([6,6]-fenil C<sub>71</sub>-butirik asit metal ester) akseptörü ile birleştirildi.

**Anahtar Kelimeler:** Kinoksalin, benzoditiyofen, yığın heterobaęlantılı güneş hücreleri, Stille çapraz kenetlenme reaksiyonu

To my beloved family...

## ACKNOWLEDGEMENTS

First and foremost, my deepest appreciation to my supervisor Prof. Dr. Ali Çırpan for giving me the opportunity to carry out this thesis in his group and for supervision and guidance along my study. I genuinely thank him for his encouraging attitude and his collaboration throughout my master study. The experience I have gained in Çırpan Research Group was invaluable.

I would also express my special thanks for Prof. Dr. Levent Toppare for his scientific expertise and his valuable comments on this thesis.

I sincerely thank Prof. Dr. Yasemin Arslan Udum for electrochemical studies of polymers. Sultan Taşkaya Aslan is thanked for her contribution in some experiments and her precious guidance in the laboratory environment.

I am grateful to Mert Can Erer both for photovoltaic studies of polymers and his friendship. He was one of my best supporters to handle difficulties in both my academic and personal life since we met. My highest gratitude goes to my best friend Gülten Özkul. Our friendship doesn't always need togetherness, as long as the relationship lives in the heart, true friends will never apart. Particularly, I would like to thank my lovely lab mates Merve, Berrin, Yeşim, Ece, Selin and Oğuzhan for their friendship and providing such a good working environment.

Finally, I would like to express my thankfulness to my family for their endless love, encourage, support and understanding. It is remarkable to feel your love always by my side.

This study supported by the Scientific and Technological Research Council of Turkey (TUBITAK) (Project number: 115F604).

## TABLE OF CONTENTS

ABSTRACT .....	v
ÖZ .....	vii
ACKNOWLEDGEMENTS .....	x
TABLE OF CONTENTS .....	xi
LIST OF TABLES .....	xv
LIST OF FIGURES .....	xvi
LIST OF ABBREVIATIONS .....	xix
CHAPTERS	
1. INTRODUCTION .....	1
1.1. Solar Energy .....	1
1.2. Conjugated Polymers .....	2
1.3. Band Theory .....	4
1.4. Doping Process .....	5
1.5. Band Gap Engineering .....	7
1.6. Donor-Acceptor Approach .....	8
1.7. Moieties in Donor-Acceptor Approach Conjugated Polymers .....	9
1.7.1. Quinoxaline Moiety .....	9
1.7.2. Benzodithiophene Moiety .....	10
1.8. Organic Photovoltaics .....	11
1.8.1. Bulk Heterojunction Device Construction .....	13
1.8.2. Working Principle in BHJ OPV Devices .....	15
1.8.3. Characterization of Organic Photovoltaics .....	16

1.8.3.1. Air Mass.....	17
1.8.4. Fundamental Parameters of Organic Photovoltaics .....	18
1.8.4.1. Power Conversion Efficiency .....	18
1.8.4.2. Open Circuit Voltage .....	19
1.8.4.3. Short Circuit Current .....	20
1.8.4.4. Fill Factor.....	21
1.8.4.5. External Quantum Efficiency .....	22
1.9. Quinoxaline and Benzodithiophene Containing $\pi$ Conjugated Polymers for Organic Photovoltaics .....	23
1.10. Aim of the Study .....	24
2. EXPERIMENTAL .....	27
2.1. Materials.....	27
2.2. Synthesis of Monomers.....	27
2.2.1. Synthesis of tributyl(4-hexylthiophen-2-yl)stannane .....	27
2.2.2. Synthesis of 4,7-dibromobenzo[c][1,2,5]thiadiazole .....	28
2.2.3. Synthesis of 3,6-dibromo-1,2-benzenediamine.....	29
2.2.4. Synthesis of 5,8-dibromo-2,3-diphenylquinoxaline.....	29
2.2.5. Synthesis of 5,8-bis(4-hexylthiophen-2-yl)-2,3-diphenylquinoxaline .....	30
2.2.6. Synthesis of 5,8-bis(5-bromo-4hexylthiophen-2-yl)-2,3-diphenylquinoxaline .....	31
2.2.7. Synthesis of 10,13-dibromodibenzo[a,c]phenazine .....	32
2.2.8. Synthesis of 10,13-bis(4-hexylthiophen-2-yl)dibenzo[a,c]phenazine .....	33
2.2.9. Synthesis of 10,13-bis(5-bromo-4-hexylthiophen-2-yl)dibenzo[a,c] phenazine .....	34
2.2.10. Synthesis of 3,6-dibromo-4-fluorobenzene-1,2-diamine .....	35

2.2.11. Synthesis of 5,8-dibromo-6-fluoro-2,3-diphenylquinoxaline.....	35
2.2.12. Synthesis of 5,8-bis(4-hexylthiophen-2yl)-6-fluoro-2,3-diphenylquinoxaline .....	36
2.2.13. Synthesis of 5,8-bis(5-bromo-4-hexylthiophen-2yl)-6-fluoro-2,3-diphenylquinoxaline .....	37
2.2.14. Synthesis of 9-(bromomethyl)nonadecane .....	38
2.2.15. Synthesis of 2-(2-octyldodecyl)selenophene .....	39
2.2.16. Synthesis of 4,8-bis(5(2-octyldodecyl)selenophen-2-yl)benzo[1,2-b:4,5-b'] dithiophene.....	40
2.2.17. Synthesis of 4,8-bis(5(2-octyldodecyl)selenophen-2-yl)benzo[1,2-b:4,5-b'] dithiophene-2,6-diyl)bis(trimethylstannane).....	41
2.3. Synthesis Polymers.....	43
2.3.1. Synthesis of P1.....	43
2.3.2. Synthesis of P2.....	45
2.3.3. Synthesis of P3.....	47
2.4. Characterization of Conducting Polymers .....	48
2.4.1. Nuclear Magnetic Resonance Spectroscopy.....	48
2.4.2. Gel Permeation Chromatography .....	49
2.4.3. Electrochemical Studies.....	49
2.4.4. Spectroelectrochemical Studies .....	50
2.4.5. Kinetic Studies.....	50
2.4.6. Thermal Studies .....	51
2.4.7. Fabrication and Photovoltaic Studies of Organic Photovoltaics .....	51
3. RESULTS AND DISCUSSIONS.....	53
3.1. Optical Studies .....	53

3.2. Electrochemical Studies .....	55
3.3. Spectroelectrochemical Studies .....	58
3.4. Kinetic Studies .....	61
3.5. Thermal Studies .....	63
3.6. Photovoltaic Studies.....	64
3.7. Morphology.....	71
4. CONCLUSIONS.....	73
REFERENCES .....	75
APPENDICES	
A. NMR DATA.....	81
B. THERMAL ANALYSIS RESULTS.....	93

## LIST OF TABLES

### TABLES

<b>Table 3.1.</b> Maximum wavelength ( $\lambda_{\max}$ ) values of all polymers both in solution and thin film.....	55
<b>Table 3.2.</b> Representative electrochemical results of polymers derived from the cyclic voltammograms.....	58
<b>Table 3.3.</b> The recorded values of $E_{g}^{op}$ and $\lambda_{\max}^{onset}$ for each polymer. ....	60
<b>Table 3.4.</b> The values of optical contrasts ( $\Delta T\%$ ) and switching times (s) at dominant wavelengths for P1, P2 and P3.....	63
<b>Table 3.5.</b> Device parameters of P1 containing OPV cells .....	65
<b>Table 3.6.</b> Device parameters of P2 containing OPV cells .....	66
<b>Table 3.7.</b> Device parameters of P3 containing OPV cells .....	66

## LIST OF FIGURES

### FIGURES

<b>Figure 1.1.</b> Repeating units and conductivities of common conjugated polymers.....	3
<b>Figure 1.2.</b> Band gap overview of a) metal, b) semiconductor, c) insulator.....	4
<b>Figure 1.3.</b> Illustration of doping mechanisms for p-type and n-type materials.....	6
<b>Figure 1.4.</b> Proposed structures of polythiophene including neutral state, polaron and bipolaron.....	7
<b>Figure 1.5.</b> Molecular orbital design of D-A approach.....	9
<b>Figure 1.6.</b> Chemical structures of quinoxaline and its some of derivatives .....	10
<b>Figure 1.7.</b> Chemical structure of benzodithiophene unit.....	11
<b>Figure 1.8.</b> Active layer representations of single layer, bilayer and BHJ solar devices .....	12
<b>Figure 1.9.</b> Device architecture of BHJ solar cell, composed of two finely intermixed phases of an acceptor (in blue) and a donor (in gray).....	13
<b>Figure 1.10.</b> Schematic representation of the working principle steps occurring in BHJ OPV devices .....	15
<b>Figure 1.11.</b> Schematic representation of the four quadrants and most important parameters derivable from the J-V curve of a solar cell under dark (in blue) and illumination (in orange) .....	17
<b>Figure 1.12.</b> Representation of air mass changes with zenith angle .....	18
<b>Figure 1.13.</b> Chemical structures of literature examples including PBQ-3, PBQ-4, P3 and P4 .....	24
<b>Figure 1.14.</b> Chemical structures of synthesized polymers P1, P2 and P3 .....	26
<b>Figure 2.1.</b> Synthetic route of tributyl(4-hexylthiophen-2-yl)stannane .....	27
<b>Figure 2.2.</b> Synthetic route of 4,7-dibromobenzo[c][1,2,5]thiadiazole .....	28
<b>Figure 2.3.</b> Synthetic route of 3,6-dibromo-1,2-benzenediamine.....	29
<b>Figure 2.4.</b> Synthetic route of 5,8-dibromo-2,3-diphenylquinoxaline .....	29

<b>Figure 2.5.</b> Synthetic route of 5,8-bis(4-hexylthiophen-2-yl)-2,3-diphenylquinoxaline.....	30
<b>Figure 2.6.</b> Synthetic route of 5,8-bis(5-bromo-4hexylthiophen-2yl)-2,3 diphenyl quinoxaline.....	31
<b>Figure 2.7.</b> Synthetic route of 10,13-dibromodibenzo[a,c]phenazine.....	32
<b>Figure 2.8.</b> Synthetic route of 10,13-bis(4-hexylthiophen-2-yl)dibenzo[a,c]phenazine .....	33
<b>Figure 2.9.</b> Synthetic route of 10,13-bis(5-bromo-4-hexylthiophen-2-yl)dibenzo [a,c] phenazine.....	34
<b>Figure 2.10.</b> Synthetic route of 3,6-dibromo-4-fluorobenzene-1,2-diamine.....	35
<b>Figure 2.11.</b> Synthetic route of 5,8-dibromo-6-fluoro-2,3-diphenylquinoxaline.....	35
<b>Figure 2.12.</b> Synthetic route of 5,8-bis(4-hexylthiophen-2yl)-6-fluoro-2,3-diphenyl quinoxaline.....	36
<b>Figure 2.13.</b> Synthetic route of 5,8-bis(5-bromo-4-hexylthiophen-2yl)-6-fluoro-2,3di phenylquinoxaline .....	37
<b>Figure 2.14.</b> Synthetic route of 9-(bromomethyl)nonadecane .....	38
<b>Figure 2.15.</b> Synthetic route of 2-(2-octyldodecyl)selenophene .....	39
<b>Figure 2.16.</b> Synthetic route of 4,8-bis(5(2-octyldodecyl)selenophen-2-yl)benzo [1,2-b:4,5-b']dithiophene.....	40
<b>Figure 2.17.</b> Synthetic route of 4,8-bis(5(2-octyldodecyl)selenophen-2-yl)benzo [1,2-b:4,5-b'] dithiophene-2,6-diyl)bis(trimethylstannane).....	41
<b>Figure 2.18.</b> Synthetic route of P1.....	43
<b>Figure 2.19.</b> Synthetic route of P2.....	45
<b>Figure 2.20.</b> Synthetic route of P3.....	47
<b>Figure 3.1.</b> Normalized UV-Vis absorption spectra of synthesized polymers a) P1, b) P2, c) P3 in CHCl <sub>3</sub> solutions (in red) and thin-films spin-coated from CHCl <sub>3</sub> (in black) .....	54
<b>Figure 3.2.</b> Cyclic voltammograms of polymers a) P1 b) P2 c) P3 in the thin films at a scan rate 100 mV/s and in 0.1 M supporting electrolyte/ solvent couple (TBAPF <sub>6</sub> /ACN).....	56

<b>Figure 3.3.</b> The change in the electronic absorption spectra of corresponding polymers a) P1, b) P2 and c) P3 upon oxidative doping potentials in supporting electrolyte/solvent couple (0.1 M TBAPF <sub>6</sub> /ACN).....	60
<b>Figure 3.4.</b> The colors and L, a, b values of corresponding polymers a) P1, b) P2 and c) P3 .....	61
<b>Figure 3.5.</b> Transmittance changes at dominant wavelengths for a) P1 b) P2 c) P3	62
<b>Figure 3.6.</b> Energy level diagrams of all polymers using data derived from cyclic voltammograms with device architecture .....	65
<b>Figure 3.7.</b> J-V curve of PSCs based on P1:PC <sub>71</sub> BM a) with different D/A ratios b) with different spin coating rates .....	69
<b>Figure 3.8.</b> J-V curve of PSCs based on P2:PC <sub>71</sub> BM with different D/A ratios .....	69
<b>Figure 3.9.</b> J-V curve of PSCs based on P3:PC <sub>71</sub> BM with different D/A ratios .....	69
<b>Figure 3.10.</b> EQE curves of P1, P2 and P3 based best performing solar cells .....	71
<b>Figure 3.11.</b> The surface morphologies of photoactive layers obtained from AFM measurements; a) P1:PC <sub>71</sub> BM (1:3, w:w), b) P2:PC <sub>71</sub> BM (1:2, w:w) c) P3 : PC <sub>71</sub> BM (1:4, w:w). Scale bar represents 200 nm.....	72

## LIST OF ABBREVIATIONS

### ABBREVIATIONS

PV	Photovoltaic
PCE	Power Conversion Efficiency
CP	Conjugated Polymer
PA	Polyacetylene
D	Donor
A	Acceptor
OLED	Organic Light Emitting Diode
OFET	Organic Field Effect Transistor
OSC	Organic Solar Cell
HOMO	Highest Occupied Molecular Orbital
LUMO	Lowest Unoccupied Molecular Orbital
VB	Valence Band
CB	Conduction Band
E <sub>g</sub>	Band Gap
BDT	Benzodithiophene
BHJ	Bulk Heterojunction
WF	Work Function
ITO	Indium Tin Oxide
PEDOT	Poly(3,4-ethylenedioxythiophene)

PSS	Polystyrene Sulfonate
ICT	Internal Charge Transfer
HTL	Hole Transport Layer
ETL	Electron Transport Layer
J	Current Density
V	Voltage
J <sub>sc</sub>	Short circuit current density
V <sub>oc</sub>	Open circuit voltage
J <sub>MAX</sub>	Maximum current density
V <sub>MAX</sub>	Maximum voltage
P <sub>MAX</sub>	Maximum power
P <sub>in</sub>	Incident power
FF	Fill Factor
TLC	Thin Layer Chromatography
THF	Tetrahydrofuran
DCM	Dichloromethane
AM	Air Mass
EQE	External Quantum Efficiency
RE	Reference Electrode
WE	Working Electrode
CE	Counter Electrode
TBAPF <sub>6</sub>	Tetrabutylammoniumhexafluorophosphate

ACN	Acetonitrile
UV	Ultraviolet
Vis	Visible
IR	Infrared
CV	Cyclic Voltammetry
GPC	Gel Permeation Chromatography
PDI	Polydispersity Index
M <sub>n</sub>	Number Average Molecular Weight
M <sub>w</sub>	Weight Average Molecular Weight
NMR	Nuclear Magnetic Resonance
TGA	Thermal Gravimetry Analysis
DSC	Differential Scanning Calorimetry
AFM	Atomic Force Microscopy
E <sub>g</sub> <sup>el</sup>	Electronic band gap
E <sub>g</sub> <sup>op</sup>	Optical band gap
PC <sub>71</sub> BM	Phenyl-C <sub>71</sub> -butyric acid methyl ester



# CHAPTER 1

## INTRODUCTION

### 1.1. Solar Energy

The world power consumption has raised incrementally day by day owing to increase in demand of energy, limited availability of reserves of non-renewable energy, continuous rising human population in developing countries and global warming [1]. According to recent studies, excessive depletion of exhaustible sources mainly fossil fuels causes environmental pollution due to high quantity of carbon dioxide (CO<sub>2</sub>) emission in the Earth's atmosphere [2]. As the quality of human life is strongly affected by environmental factors including climate change and air pollution, generation of energy from alternative clean sources is the most important topic in today's world. The urgency of power production allows scientist to search new future energy sources: the renewable energy. Nowadays, the most environmentally friendly, clean and sustainable renewable energy is known as solar energy. The sunlight provides vast amount of radiation (about 120000 terawatts) to the surface of earth at the certain time intervals of the day and these huge radiation is 6000 times greater than the energy consumption rate of the world [3]. These fascinating properties make solar energy as the best accessible candidate for energy production.

All around the world solar energy is the most commonly utilized for the generation of electricity but the main concern is the harnessing light in a cost-effective way. Conversion of sunlight into the electrical energy can be generated by photovoltaic effects. Furthermore, organic and inorganic based semiconducting materials are used in photovoltaic (PV) applications. Si-based inorganic semiconductors in other words first generation solar cells are mainly used to produce high power conversion efficiency (PCE) devices (around 20-25%) as they exhibit high conductivity, stability

in the air also high mobility [4]. However, it is claimed that first generation PV production is very expensive, energy consuming and laborious process. Moreover, the processing step of inorganic material based solar cells requires high temperatures (400-1400 °C) and high vacuum conditions. Hence, the scientific studies were pointed organic based photovoltaics to decrease production cost in a safety way [5], [6]. Most specially, in both industrial and scientific areas  $\pi$  conjugated polymer based organic photovoltaics play a crucial role to electricity production. Before going to extensive analysis of organic photovoltaics, it could be useful to understand and investigate properties of conjugated polymers (CPs).

## 1.2. Conjugated Polymers

The basic description of polymers is that the macromolecules comprise repeating chains of molecules. These macromolecules exist in nature as a non-conductive material and they have long been used as an insulator. In 1977, Shirakawa and his co-workers synthesized polyacetylene (PA) from ethyne by doping with halogen vapor and they recognized that PA exhibits significantly high electrical conductivity ( $10^3$  S/cm). In accordance with this experiment, scientists concentrated on studies about development of conductivity in polymers (CPs) [7], [8]. Later, conducting polymers were defined as Nobel Prize winning materials owing to the Nobel Prize in Chemistry were given to three scientists namely Alan J. Heeger, Alan G. MacDiarmid and Hideki Shirakawa in 2000 [9], [10]. Conducting polymers form a type of conjugated polymers. Conjugated polymers possess alternating double and single bonds within the unsaturated polymer backbone and  $\pi$ -electrons of these materials can be easily delocalized along the chain axis. Free movement of  $\pi$ -electrons build an electrical pathway for charge carriers and hereby CPs can conduct electricity.

Recently, these materials have gained significant academic and industrial interest due to their unique properties such as solution processability, low cost, ease in band gap tailoring by structural design modification and flexibility [11], [12]. Their fascinating

characteristics especially electrical conductivities and conjugated structures create new research areas and CPs have been widely studied in Organic Solar Cells (OSCs), Organic Light Emitting Diodes (OLEDs), Electrochromic Devices (ECDs), Organic Effect Transistors (OFETs) over the last decades [12]–[14].

The repeating units and electrical conductivities of most commonly used conjugated  $\pi$  conductive polymers which are polyacetylene, polypyrrole, poly(3,4-ethylenedioxythiophene), polythiophene, polyphenylene, poly(p-phenylenevinylene) and polyaniline were illustrated in Figure 1.1 [12], [14].

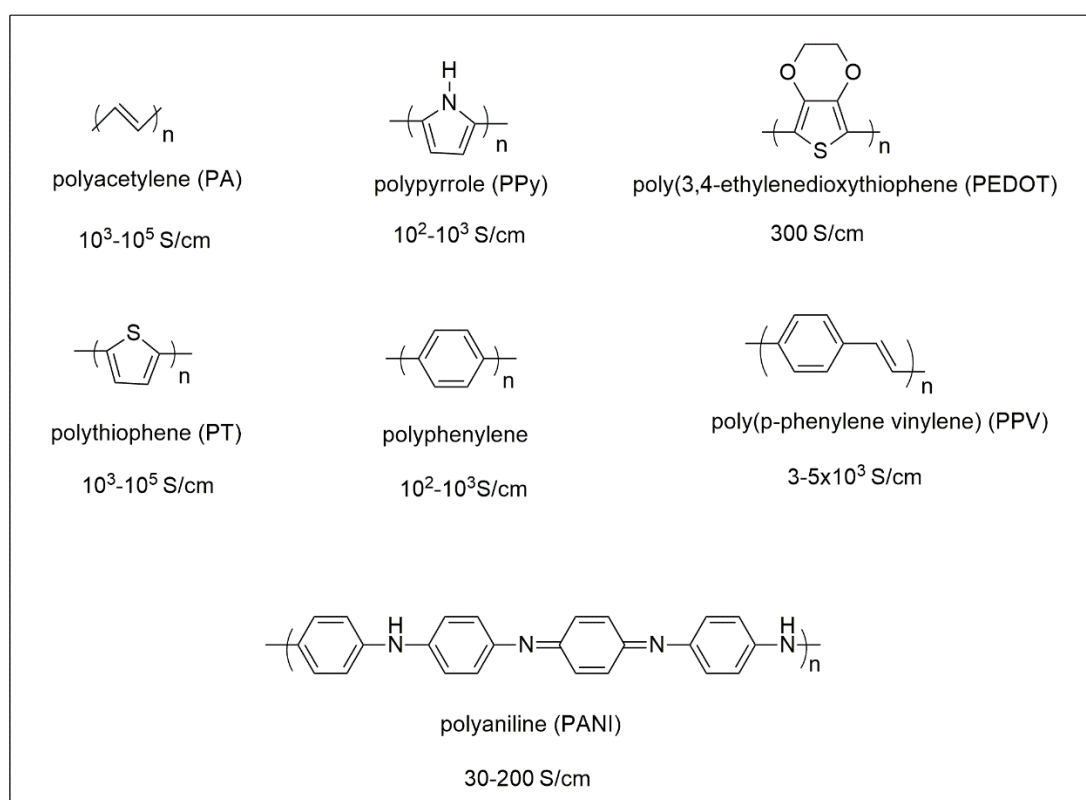


**Figure 1.1.** Repeating units and conductivities of common conjugated polymers

### 1.3. Band Theory

The energy spacing between the highest occupied molecular orbital (HOMO) of the valence band (VB) and the lowest unoccupied molecular orbital (LUMO) of the conduction band (CB) is described as the band gap ( $E_g$ ) and this term is the demonstrator of the electrical conductivities of the materials. Basically,  $E_g$  represents minimum energy that is needed to excite valence electrons to the conduction band. Band theory explains the conduction process and characteristic difference between insulators, semiconductors and conductors. In other words, this theory deals with materials whether or not have electrons in their conduction band [15]. In order to get better understanding of some of the distinct properties of materials, their size of band gaps were visualized in the following Figure 1.2.

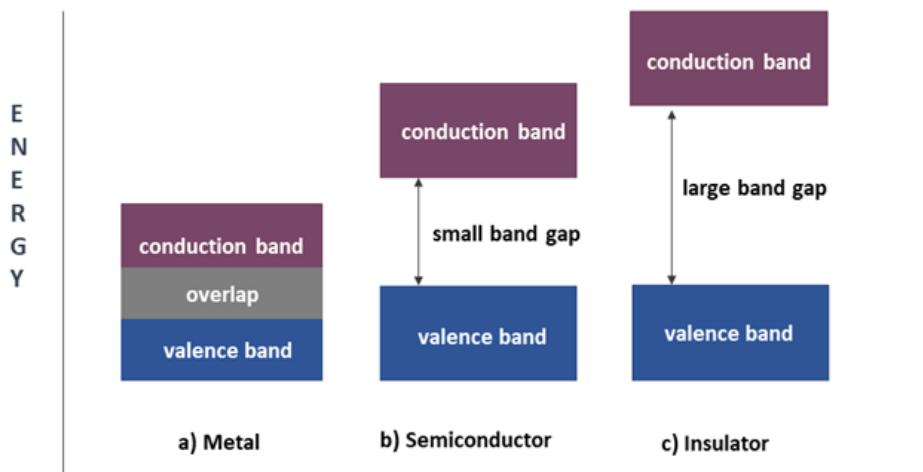


**Figure 1.2.** Band gap overview of a) metal, b) semiconductor, c) insulator

The valence band of conductors (or metals) is partially filled and their conduction band is empty. With an applied electric field, valence electrons can travel to the empty positions of conduction band since there is no energy difference between VB and CB. The overlapping between these two bands leading conduction of electricity by free movements of electrons. In the case that, the valence band is separated by a large band

gap from the conduction band, the material is called as an insulator. A large gap denotes that too much energy is needed to excite valence electrons to form a current. This gap prevents movements of electrons through the material moreover insulator does not conduct electricity. On the other hand, the size of band gap of semiconductors is in between that of insulator and conductor. Due to small band gap, electrons can reach to the empty CB from the fully filled VB and this property allows semiconductors to conduct electricity. Conducting  $\pi$  conjugated polymer is one the of example of semiconducting materials and small gap provides travelling of electrons through the chain axis of the polymer [15], [16].

#### **1.4. Doping Process**

Doping is the fundamental process to enhance the conductivity of the polymeric materials since most of the conjugated polymers do not have charge carriers in their neutral state. Moreover, a small amount of doping process can increase dramatically the electrical conductivities of these materials by converting neutral conjugated system into an ionic state which contains charge carriers [17]. Chemical doping and electrochemical doping are the most commonly used two methods to gain conductive ability for the polymers. First technique relies on a reaction between the vapor of reductive or oxidative agent (dopant) with CPs and latter based on redox reaction by applying potential to the CPs. The basic principle of doping is that introduction of charge carriers to the polymer backbone of organic semiconductors by oxidation or reduction reaction. In this concept electrons are either transferred to the LUMO states to generate negatively charged anions or they are removed from the HOMO states to create free holes. When an electron is introduced into the polymer chain, this is called as n-type doping, whereas the removal of electron from the chain is called as p-type doping [17], [18]. Two types of doping mechanisms (p-type, n-type) are depicted in following Figure 1.3.

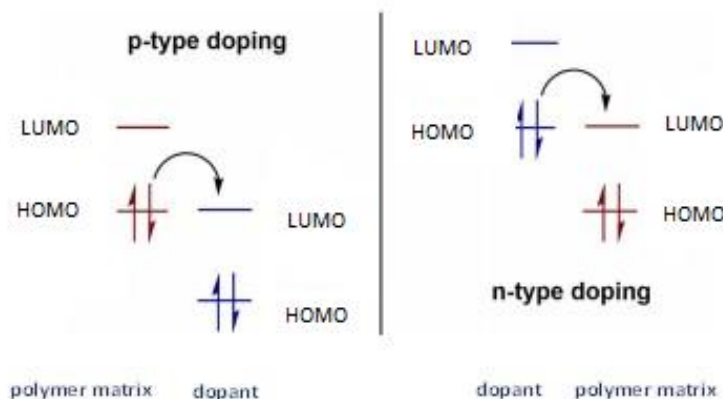


**Figure 1.3.** Illustration of doping mechanisms for p-type and n-type materials

As a result of n-type and p type doping, charge defects which are polaron, bipolaron and soliton are formed. These defects are named with respect to ground state degeneracy of the conjugated materials. As compared to degenerate ground state linear molecules like polyacetylene (PA), most of the conjugated polymers do not possess degenerate ground states. Furthermore, polaron and bipolaron formation can be seen in the non-degenerated ground state materials, negatively and positively charged soliton formation occurs in materials which have degenerated ground state molecules. Removal of one  $\pi$ - electron by oxidation creates a polaron (radical cation) and further oxidation produces bipolaron (dication) structure and generated positive charges (polaron, bipolaron) ensure conduction in non-degenerate ground state conjugated polymers [17]–[19].

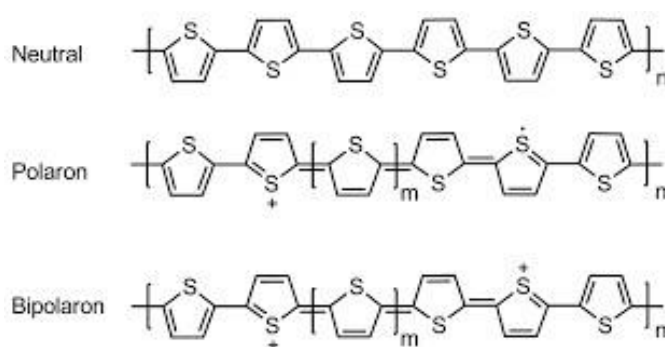


**Figure 1.4.** Proposed structures of polythiophene including neutral state, polaron and bipolaron

### 1.5. Band Gap Engineering

The process which includes several design strategies to control band gap of the conducting polymers is called as band gap engineering. Furthermore, tuning of the band gap of  $\pi$  conjugated polymers shows critical importance to get better knowledge about the electronic properties of these delocalized systems. Molecular engineering of fine tune of the  $E_g$  ultimately depends on the five essential parameters namely bond length alternation pattern ( $E_{BLA}$ ), aromaticity ( $E_{Res}$ ), planarity ( $E_{\theta}$ ), electron releasing or withdrawing substituents ( $E_{Sub}$ ) and intermolecular interactions ( $E_{Int}$ ). The magnitude of band gap of conjugated systems can be expressed by following formula which is the sum of these parameters [15], [16], [20], [21].

$$\text{Eg: } E_{BLA} + E_{Res} + E_{\theta} + E_{Int} + E_{Sub}$$

As mentioned before, CPs have a non-degenerate ground state and they possess two mesomeric forms (aromatic and quinoid) with different stabilization energies. Delocalization of  $\pi$  electrons through the polymer chain leads switching of aromatic form into the quinoid form. Destruction of the aromaticity via lowering stabilization energy results less stable quinoid structure and smaller HOMO-LUMO gap as compared to aromatic structure [22]. Bond length alternation can be represented by the ratio of aromatic to quinoid population of conjugated material and this term excessively depends on aromatic stabilization energy of conjugated systems. The more quinoid population in the ground state means less BLA and lower band gap since electron mobility on quinoid structure also double bond character between two adjacent rings increase at the same time [21].

In order to enhance delocalization and conjugation of backbone, planarity should be functionalized by checking p orbital attractions of molecules. Parallel p-orbital interaction is preferred rather than perpendicular one since former interaction extends length of conjugation also ease electron delocalization on conjugation main chain. Hence tailoring planarity leads reduction of HOMO-LUMO levels via lowering BLA [20], [23].

One of the most substantial way to modulate band gap is the introduction of substituents to the conjugated systems. If the electron withdrawing (accepting) group is attached to the polymer matrix, it causes a decrease in electron density and the LUMO energy level, so band gap also decreases. Conversely the electron releasing (donating) group results in enhancement in electron density on the polymer chain this results in the raise of HOMO energy level thus band gap increases [20], [21].

Intermolecular interactions have impact on the band gap since they cause more crystalline structure and more covalent rigidification for solid state of material via individual polymer chain interactions. Moreover, the  $\pi$ - $\pi$  stacking in red shift on the ground state spectrum of solid materials increases as a contribution of interactions. Polymer chains interact with each other by secondary forces such as Van Der Waals and dipole interactions. These interactions creates enhancement of electron delocalization along the chain axis, so magnitude of band gap decreases [21].

## **1.6. Donor-Acceptor Approach**

Molecular design strategy is utilized to the electrically CPs to afford low band gap. Havinga and his co-workers were created a new structural concept on the polymer backbone using electron-rich donor (D) moieties and electron deficient acceptor (A) moieties in 1993 [24]. With this phenomenon, they claimed alternation of donor and acceptor unities showing hybridization of CB and VB of the materials via intermolecular interactions. Combination of electron donor with higher HOMO and electron acceptor with lower LUMO results in reduction of band gap owing to

interchain charge transfer between neighboring molecules. In the new concept, the lowest unoccupied molecular orbital of the polymer belongs to LUMO level of the acceptor group and the highest occupied molecular orbital of the polymer belongs to HOMO level of the donor group [24], [25]. Besides lowering  $E_g$ , it has been proven that D-A approach provides some new optical and electronic properties to the  $\pi$  conjugated systems such as enhancement of charge mobility and longer wavelength absorption [26], [27].

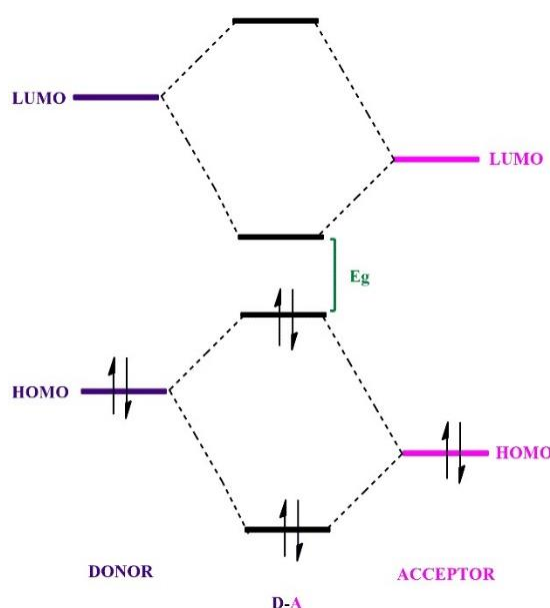


**Figure 1.5.** Molecular orbital design of D-A approach

## 1.7. Moieties in Donor-Acceptor Approach Conjugated Polymers

### 1.7.1. Quinoxaline Moiety

The stable quinoid structures and electron deficient characters of quinoxaline unities make them promising candidates for utilizing acceptor part of the conjugated D-A polymers. Quinoxalines can also be called as benzopyrazines since these aromatic heterocycles contain pyrazine and benzene rings on their chemical backbone. Strong

electron withdrawing nature comes from the imine nitrogens at the 1,4 positions of the pyrazole ring and this property provides high electron transporting ability to the quinoxaline derivatives [28], [29]. These moieties have been commonly employed to construct low band gap copolymers with high solubility as quinoxalines can be easily functionalized from 2<sup>nd</sup> and 3<sup>rd</sup> positions. Hence the control of solubility becomes easy with this functionalization characteristic of strong acceptor unities [28].

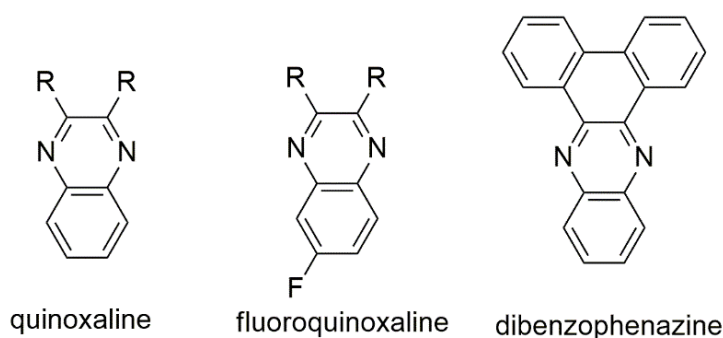


**Figure 1.6.** Chemical structures of quinoxaline and its some of derivatives

### 1.7.2. Benzodithiophene Moiety

Since the paper of Hou and Yang et al. on the synthesis of benzo[1,2-b:4,5-b']dithiophene (BDT) with various conjugated structures was published, BDT moiety has attracted great interest in the photovoltaic studies as a donor unity [30]. BDT building block has structural symmetry with a rigid fused aromatic system that contains benzene ring with two flanking thiophene. This fused unit shows excellent electron donating property since large planar conjugated backbone provide easy formation of  $\pi$ - $\pi$  stacking [31]. Hence charge carrier mobility of BDT containing polymers expected to be high in solar applications owing to continuous electron delocalization on the polymer axis. Also, by attaching several substituents (alkyl or alkoxy) at the 4 and 8 positions of BDT, some properties of this donor moiety such as solubility, absorption maxima and band gap can be controlled [32].

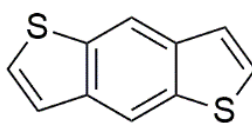


**Figure 1.7.** Chemical structure of benzodithiophene unit

### 1.8. Organic Photovoltaics

Organic photovoltaics can be basically defined as diode systems that absorb light to generate current by collecting of charges. As it was stated previously compared to inorganic counterparts, conjugated organic semiconducting materials exhibit properties like low cost fabrication, flexibility, high absorption coefficient in the visible range, solution processability. Unlike inorganic materials, they need much lower temperatures (20–200 °C) for processing. Also, delocalized  $\pi$  electron system of conjugated organic semiconductors build electrical pathway for charge carriers through the polymer backbone [6]. For these reasons, they are preferred for utilizing active layer of photovoltaics. However, the main drawback of organic semiconductors upon applying to solar cells is low power conversion efficiency (PCE). This drawback led scientist to construct and develop different solar device architectures like single layer, bilayer or bulk heterojunction solar cells. The typical structure of organic photovoltaics contains stack of layers. Generally, active layer which was comprised of donor and acceptor moieties is sandwiched between two electrodes (transparent and non-transparent) [33]. Figure 1.8. represents active layers of the single layer, bilayer and bulk heterojunction solar devices.



**Figure 1.8.** Active layer representations of single layer, bilayer and BHJ solar devices

Single layer solar device is known as the simplest and most basic architecture in the literature and it contains a single layer of active organic material between two electrodes. However, the reported charge mobilities and interfacial area between active layer and electrodes are both significantly low, hence device yields very low efficiencies (around 0.1%) in PV applications [34]. Later, the successful bilayer device construction pertaining to enhancement efficiency of organic photovoltaics (OPVs) were done by C. Tang and his co-workers in 1986. In this report, they construct bilayer solar device with 1% PCE which contains two distinct organic semiconductors; p-type and n-type also known as donor (D) and acceptor (A) materials respectively [35]. This device was designed in order to achieve effective charge separation with an improvement of photoconversion efficiency. However, efficiency of device is limited due to low donor-acceptor interfacial area and low diffusion pathway which leads recombination of free charges. A reasonable way for enhancing efficiency of bilayer photovoltaics is to adjust diffusion length while maximizing the donor-acceptor interfacial area. In the view of this idea, Yu, Heeger and their co-workers designed Bulk Heterojunction (BHJ) device where the acceptor and donor semiconductors are blended in a bulk forming morphology in the active layer. As compared to bilayer device, BHJ device overcomes the charge generation and exciton diffusion problems since matrix of donor-acceptor provides long diffusion length and effective charge separation and also prevents charge recombination at the interface [36]. More detailed information about the working principle and the device architecture of bulk heterojunction devices will be discussed in the following sections.

### 1.8.1. Bulk Heterojunction Device Construction

As it was mentioned before, active layer BHJ solar cells contains acceptor and donor materials in a bulk forming morphology and this layer sandwiched between two electrodes with different work functions (WF) namely anode and cathode. Generally, transparent indium tin oxide (ITO) glass substrate functions as the anode and LiF/Al or Ag metals served as cathode. A basic device structure can be represented from bottom to top as ITO coated glass/hole transport layer/donor-acceptor blend/cathode and it was schematically depicted in Figure 1.9.

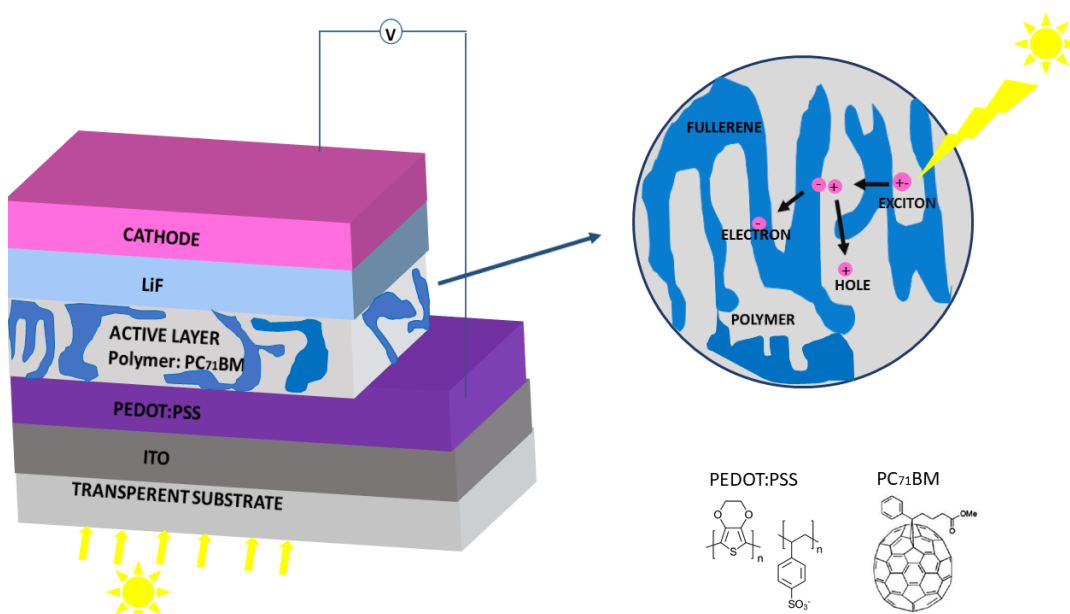


**Figure 1.9.** Device architecture of BHJ solar cell, composed of two finely intermixed phases of an acceptor (in blue) and a donor (in gray)

Firstly, anode is formed by coating ITO onto the transparent glass. Conducting ITO coated transparent glass exhibits features like high work function (WF) (around 4.70 eV) and high transparency (90% in visible) [37]. While the high WF of ITO allow collection of holes, high transparency eases transmission of light to the photoactive

layer. Then second layer that contains polyethylenedioxythiophene: polystyrene sulfonate (PEDOT:PSS) is coated on the top of anode. This layer also known as the hole transport layer since PEDOT:PSS eases the removing of holes by reducing WF of ITO at the same time it helps to smoothen the surface of ITO.

The blend containing active layer is spin coated onto the hole transport layer. Blends can be formed by mixing conjugated polymer and fullerene derivatives with different concentrations. The idea of combining polymer and fullerene (C<sub>60</sub>) derivatives belongs to Sariciftci and Heeger. These blend materials have been widely applied in the active layer of bulk heterojunction cells since ultrafast photoinduced charge transfer (ICT) from donor (conjugated polymer) to the acceptor (buckminster fullerene) was proven by these two scientists in 1992 [38]. In the BHJ photovoltaics, electron rich conjugated polymers or small molecules act as a donor and fullerene derivatives act as an acceptor molecule owing to their special characteristics. As mentioned before, conjugated polymer that is synthesized with respect to D-A approach shows new features such as high absorption in solar spectrum with a narrow band gap [39]. Moreover, these electron rich materials that are blended in photoactive layer are responsible for absorbing the incoming solar light in BHJ devices due to good absorption ability. On the other hand, fullerene containing molecules exhibits triply degenerate excited state and they can accept up to six electrons thus they exhibit good electron withdrawing property [40], [41]. Also, these electron deficient materials can be modified chemically for example solubility of modified fullerene namely phenyl-C<sub>71</sub>-butyric acid methyl ester (PC<sub>71</sub>BM) is much higher than the unmodified one [42]. As a final step of the construction of BHJ solar cells, aluminum metal is thermally evaporated to build the cathode layer on the top of the device. An ideal cathode material should exhibit low work function in order to collect electrons. However, Al metal has relatively high work function and LiF which is the hole blocking layer is coated to between active layer surface and metal contact in order to decrease WF of metal.[43]. In this way, electron transportation to the cathode becomes easier since electrons can excite higher energy levels. Besides lowering work

function of the Al, LiF supplies smooth surface for deposition of metal contact onto the photoactive layer.

### 1.8.2. Working Principle in BHJ OPV Devices

As schematically represented in Figure 1.10. four basic steps are necessary for functioning of BHJ solar cells in other words for generation of electrical power under illumination [40], [44].

- Absorption of incident light by the photoactive material with the generation of coulombically bound electron hole pair (exciton)
- Diffusion of exciton toward the D/A interface
- Exciton dissociation into free carriers (electron and hole) at the interface between D/A and migration of electrons and holes through the donor or acceptor phases
- Collection of electrons at one electrode (cathode) and holes at the opposite electrode (anode) [44].

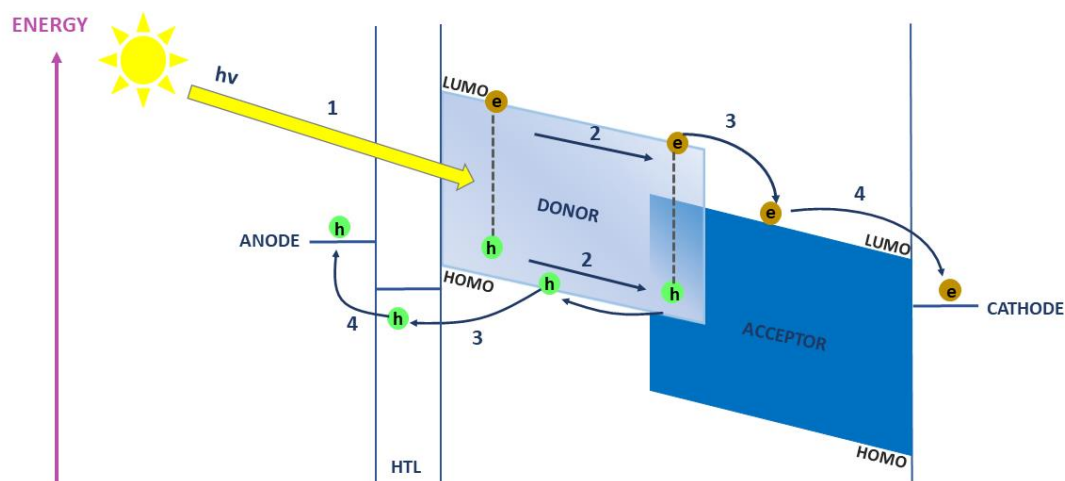


**Figure 1.10.** Schematic representation of the working principle steps occurring in BHJ OPV devices

The incoming sunlight penetrates into D/A blend and light absorption occurs in photoactive layer. In most cases donor material is the main absorber since it has higher absorption coefficient than acceptor. Absorption of light causes excitation of electrons to the higher energy level (LUMO) while leaving holes in the HOMO level but electrons and holes still bounded by coulombic interactions [45]. This bounded electron hole pair generates a Frenkel exciton. Then, exciton diffusion process occurs via transportation of Frenkel exciton through the D-A interface. In this step, exciton diffusion length should be adjusted about 5-20 nm in order to prevent recombination of charges for organic materials [46]. Exciton dissociation into free carriers can happen only if the driving force is adequate to overcome coulombic interaction energy of exciton which ranges from 0.3 to 1.4 eV for organic systems [47]. Since the interphase between D-A being well dispersed throughout the bulk, small exciton diffusion lengths are expected for BHJ solar cells and all excitons will be dissociated with their lifetime. After dissociation process, separation of exciton into the electron and hole is accomplished at the D-A interface, free charges migrate through the D and A phases. Then, collection of free charges at the respective electrodes takes place. As it was stated before, work functions of electrodes should be different for efficient charge extraction [48]. As can be seen in the above figure, the WF of anode should have higher energy than the HOMO level of the donor material and the WF of cathode material should have lower energy than the LUMO level of acceptor material [45], [49]. Hence, the high work function of ITO allows collection of holes at the anode and the low work function of LiF coated metal eases collection of electrons at the anode [43].

### **1.8.3. Characterization of Organic Photovoltaics**

The right-hand side of below Figure 1.11. represents the typical current density (J) versus voltage (V) curve both under light and dark for a photovoltaic characterization of solar devices. The curve represents key parameters which describe performance of the solar cells namely open circuit voltage ( $V_{OC}$ ), short circuit current ( $J_{SC}$ ), the

maximum power ( $P_{MAX}$ ), the voltage at max power point ( $V_{MAX}$ ) and the current at max power point ( $J_{MAX}$ ) [50],[44].

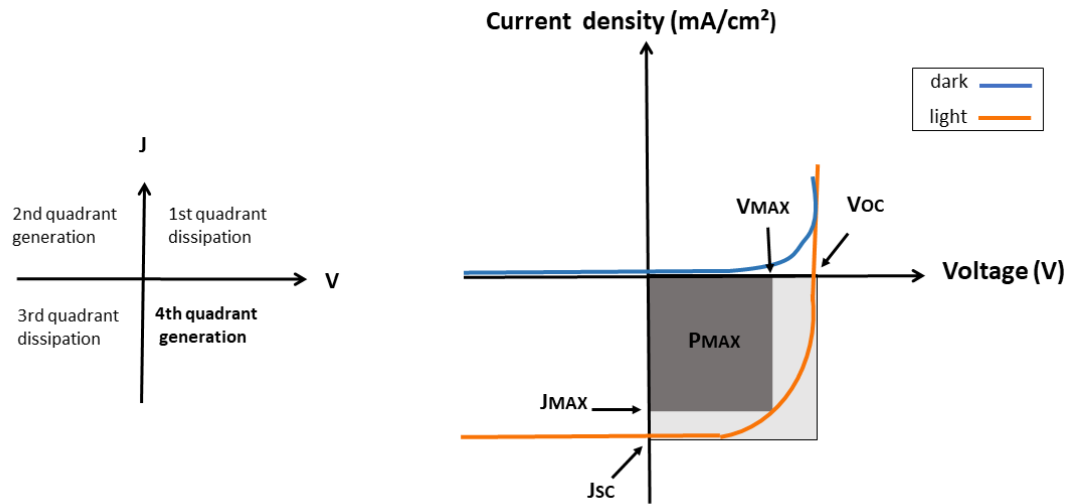


**Figure 1.11.** Schematic representation of the four quadrants and most important parameters derivable from the J-V curve of a solar cell under dark (in blue) and illumination (in orange)

As seen at the left side of Figure 1.11., J-V curve possesses four quadrants. If the illuminated solar cell applications are performed in the 4<sup>th</sup> quadrant of the graph where current is negative and voltage is positive, power is generated. However, under the dark conditions since power generation cannot be observed without illumination graph crosses over the origin with almost zero potential [50].

### 1.8.3.1. Air Mass

A measure of how much sun rays should pass through to reach the earth surface is the definition of air mass (AM). A mathematical relationship between solar angle and air mass can be described as the inverse of cosine of the zenith angle (ZA) of the sunlight and it can be formulated as following;

$$AM = 1/\cos(ZA^\circ)$$

Air mass is a varying parameter since the sun moves through the sky and changes its path during day and seasons. Spectral distribution of solar radiation at the surface of earth relies on some atmospheric constituents like clouds, water vapor or aerosols. Moreover, these conditions cause reduction of solar power which directly affect the air mass measurements. For these reasons, it is necessary to select air mass for standard reference spectra so called AM1.5 global (G). The solar angle of reference spectra is measured as  $48^\circ$  as can be seen in the Figure 1.12. In order to characterize photovoltaic devices AM1.5 G spectrum with total intensity of  $1000 \text{ W/m}^2$  is used. If the sun is directly crossed the earth's surface AM1 G spectrum is utilized as standard and AM0 G spectrum is used for space applications [51].

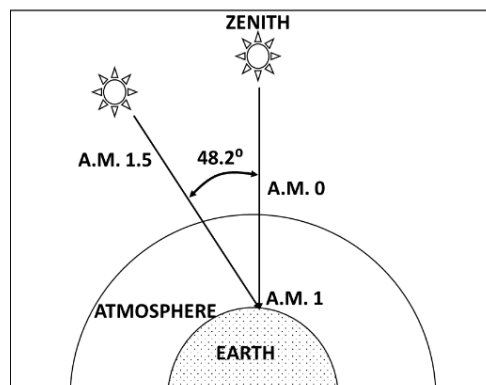


**Figure 1.12.** Representation of air mass changes with zenith angle

## 1.8.4. Fundamental Parameters of Organic Photovoltaics

### 1.8.4.1. Power Conversion Efficiency

The power conversion efficiency (PCE) that is briefly called as efficiency of the solar cells is the ratio of maximum power ( $P_{MAX}$ ) generated by the cell to the power that the cell is exposed in other words incident power ( $P_{IN}$ ). By using J-V curve PCE of cells

can be determined and all the measurement to yield J-V curve were done under AM1.5G illumination spectrum with intensity of 1000 W/m<sup>2</sup>. PCE of devices are quantified with the use of given equations;

$$\text{PCE}\% = \frac{P_{MAX}}{P_{IN}} \times 100 \quad \text{PCE} = \text{FF} \times J_{SC} \times V_{OC}$$

Fill factor (FF) can be basically identified as the indicator of the quality of a solar cell since this parameter play a crucial role to determine the efficiency of the devices. FF and its effects on the performance of the cell will be discussed deeply in the following sections. Before mentioning FF, the terms that are V<sub>OC</sub> and J<sub>SC</sub> should be well understood.

#### 1.8.4.2. Open Circuit Voltage

Open circuit voltage (V<sub>OC</sub>) is read from the potential value measured for the illuminated photovoltaic systems when the current is zero. Due to migration of free charges to the anode and cathode, the potential difference is created between two electrodes and this recorded voltage is called as V<sub>OC</sub> [44]. The mathematical value of the V<sub>OC</sub> can be computed approximately from the following equation;

$$V_{OC} = \frac{1}{e} (E_{\text{donorHOMO}} - E_{\text{acceptorLUMO}}) - 0.3 \text{ V}$$

E<sub>donor HOMO</sub> and E<sub>acceptorLUMO</sub> stand for the HOMO level of donor material and LUMO level of the acceptor material respectively and e is the elementary charge. As shown in the equation V<sub>OC</sub> has linear dependence with energy difference between the LUMO of the acceptor and HOMO of the donor with an approximate loss of 0.3 V. Moreover, energetic alignment of the LUMO and HOMO levels between acceptor and donor materials provides large V<sub>OC</sub> and efficient exciton dissociation within environmental stability. Recombination process is the very important limiting factor for the open circuit voltage value. When the electrons and holes meet before being

collected at the electrodes, recombination takes place as a result of this process  $V_{OC}$  decreases [52]. Appropriate morphology of donor acceptor blend and morphology of electrodes should be adjusted well to prevent recombination of charges [49]. Hole transport layer (HTL) and electron transport layer (ETL) are utilized in the BHJ solar cell architecture in order to enhanced  $V_{OC}$  value by providing effective charge collection in the corresponding electrodes [53].

#### **1.8.4.3. Short Circuit Current**

The short circuit current ( $J_{SC}$ ) read from current value measured for the illuminated photovoltaic system when there is no external field applied. This value is the maximum current that flows through cell and it can be measured from the area of the solar cell thus it is denoted as the short circuit current density[44]. Equation below is the basic equation of  $J_{SC}$  where  $e$  is the elementary charge,  $E$  is the applied electric field,  $n$  stands for the density of charge carrier and lastly  $\mu$  corresponds charge carrier mobility;

$$J_{SC} = eEn\mu$$

$J_{SC}$  is substantially related with number of photons absorbed by active layer, the band gap, the quantum efficiency for separation of free charges and migration of charge carriers in the photovoltaic applications [54]. As it was stated before, donor material is the main absorber in the photoactive layer and the features of donor molecule to absorb light directly affects the  $J_{SC}$  value. If the donor ratio in the D-A blend increases, absorption and  $J_{SC}$  values are expected to rise as well. Short circuit current density also highly depends on the charge mobility in the donor acceptor phases hereby on morphology of the blend and charge collection [53], [50]. Generally in photovoltaic devices, the enhancement of  $J_{SC}$  value results in higher hole mobility and this situation enables the better hole transport through the active layer [50].

#### 1.8.4.4. Fill Factor

For the quantification of PCE, the parameter that is fill factor (FF) should be well described. The ratio of maximum power ( $P_{MAX}$ ) generated from device to the theoretical maximum power obtained from cell gives the value of fill factor [44]. Maximum power is the product of maximum voltage ( $V_{MAX}$ ) and current ( $J_{MAX}$ ) and theoretical maximum power is the multiplication of short circuit current ( $J_{SC}$ ), and open circuit voltage ( $V_{OC}$ ). Based on following equation FF can be calculated;

$$FF \% = \frac{J_{MAX} \times V_{MAX}}{J_{SC} \times V_{OC}} \times 100$$

As mentioned before fill factor is the indicator of quality of solar cells which means this parameter explains the performance of devices with respect to its full capacity. From the J-V curve which was stated in Figure 1.11, FF can be illustrated as the area of the largest grey rectangle thus FF is so called as the squareness of the photovoltaic cells. The FF is equal to unity for an ideal case, but this is unachievable value since  $P_{MAX}$  of cell always lower than the ideal maximum power. Deviation of cells from ideal case arises from its electrical resistances namely shunt resistance ( $R_{sh}$ ) and series resistance ( $R_s$ ). Shunt resistance includes power loss of a cell by leakage of current. On the other hand, series resistance involves all the interfaces in the separated layers of solar cells including resistance of contacts between photoactive layer and the electrodes and self-resistance of photoactive layer. In order to achieve efficient charge separation, the contact resistance in other words series resistance should be low and shunt resistance should be high [55]. These adjustments of resistances are necessary for the optimization of FF and PCE of solar cells. Indeed, lower  $R_s$  value and higher  $R_{sh}$  value result in higher FF and consequently higher efficiency. The FF value also related with the D-A containing active layer morphology. As mentioned previously controlling D-A blend morphology is the most important process for the charge separation and collection as well as for the improvement of  $V_{OC}$  and FF [53],[48]. Also, the factors affecting the  $J_{SC}$  values are also affect the fill factor such as number

of photons absorbed and the efficiency for separation of free charges. As the current passing through the system increases, fill factor also increases. As a result, FF is mainly affected by several factors like  $R_s$ ,  $R_{sh}$  and the morphology of photoactive layer and to obtain optimized solar performance all these factors should be tuning and controlling very well [55].

#### 1.8.4.5. External Quantum Efficiency

External quantum efficiency (EQE), also denoted as incident photon to current efficiency (IPCE) is another important parameter for the characterization of photovoltaics. It represents quality of energy conversion. The ratio of number of carriers extracted out of the cell to the number of all incoming photons on the cell gives the EQE value of the solar device. If there are no losses of charges owing to recombination process, EQE is equal to unity that means every incident photon absorbed by active layer and results in generation of charge carriers at the corresponding electrodes. The EQE value is directly related with two terms short circuit current ( $J_{SC}$ ) of the device and intensity of incoming light ( $J_I$ ) at the same wavelength ( $\lambda$ ) [56]. Moreover, quantum efficiency can be formulated as a function of wavelength as following;

$$EQE(\lambda) = \frac{J_{SC}(\lambda)}{J_I(\lambda)} \times \frac{hc}{\lambda q}$$

In the above formula,  $h$  represents the Planck constant and  $c$  stands for the speed of light. As mentioned before,  $J_{SC}$  is correlated with absorption capacity of active layer and any losses owing to reflection and scattering in the absorption process cause reduction of current density hence decreases in EQE value. Generally, EQE is far from unity for most BHJ based photovoltaic applications [50].

## 1.9. Quinoxaline and Benzodithiophene Containing $\pi$ Conjugated Polymers for Organic Photovoltaics

The design and synthesis of new low band gap conjugated polymers based on donor-acceptor approach has been proven to be an effective strategy to achieve high PCE. Therefore, researchers try to couple the appropriate moieties for the synthesis of donor and acceptor subunits on the main chain of polymers [39]. BDT unit has commonly implemented as an attractive donor building block for bulk heterojunction solar cells owing to its coplanarity, rigidity, extended  $\pi$  conjugation. It also demonstrates substantial PCEs when coupled with various acceptors such as benzothiadiazole (BT), thienopyrroledione (TPD) and quinoxaline [57]. On the other hand, derivatives of quinoxalines have been utilized as an acceptor due to the electron withdrawing property of imine nitrogen and relatively stable quinoid form. Quinoxalines have led high efficiencies when copolymerized with various electron donor materials, including carbazole and benzodithiophene [58]. The first BDT and quinoxaline containing polymer was synthesized by Hou and coworkers with a very low PCE of 0.23% in 2008 [30]. The further studies and strategies were performed to enhance the PCE of the quinoxaline and BDT based  $\pi$  conjugated polymers for solar cells.

In 2015, Liu and co-workers coupled BDT and 2,3-diphenyl-5,8-di(thiophen-2-yl) quinoxaline units to construct active layer of following conventional BHJ solar cell architecture; ITO/PEDOT:PSS/BHJ blend/Ca/Al. They recorded PCE of these copolymers namely PBQ-3 and PBQ-4 as 7.39% and 8.55% respectively under same and optimum conditions. In this work, they proved that the introduction of fluorine(F) atom onto both acceptor (quinoxaline) and donor (BDT) units has an enhancing effect on the  $V_{OC}$  of the devices since the devices of PBQ-3 and PBQ-4 showed  $V_{OC}$  of 0.76 V and 0.80 V, respectively [59]. Sun et al. published an article on the synthesis of BDT and phenanthrene quinoxaline based conjugated polymers for OSCs in 2015. In order to enhance photovoltaic performance of the devices, they designed and synthesized P3 and P4. In comparison with P3, alkoxy chains at the acceptor unit was translated into alkyl chain at thiophene bridge of P4 and as expected P4 was

demonstrated higher PCE than P3 with smaller band gap. The device based on P3 showed PCE of 3.68% with a  $J_{SC}$  of 9.21 mA/cm<sup>2</sup>,  $V_{OC}$  of 0.80 V and FF of 0.50. and, the device based on P4 exhibited higher  $J_{SC}$  of 11.6 mA/cm<sup>2</sup> and PCE of 4.32% [60]. Figure 1.13 illustrated chemical structures of PBQ-3, PBQ-4, P3 and P4;

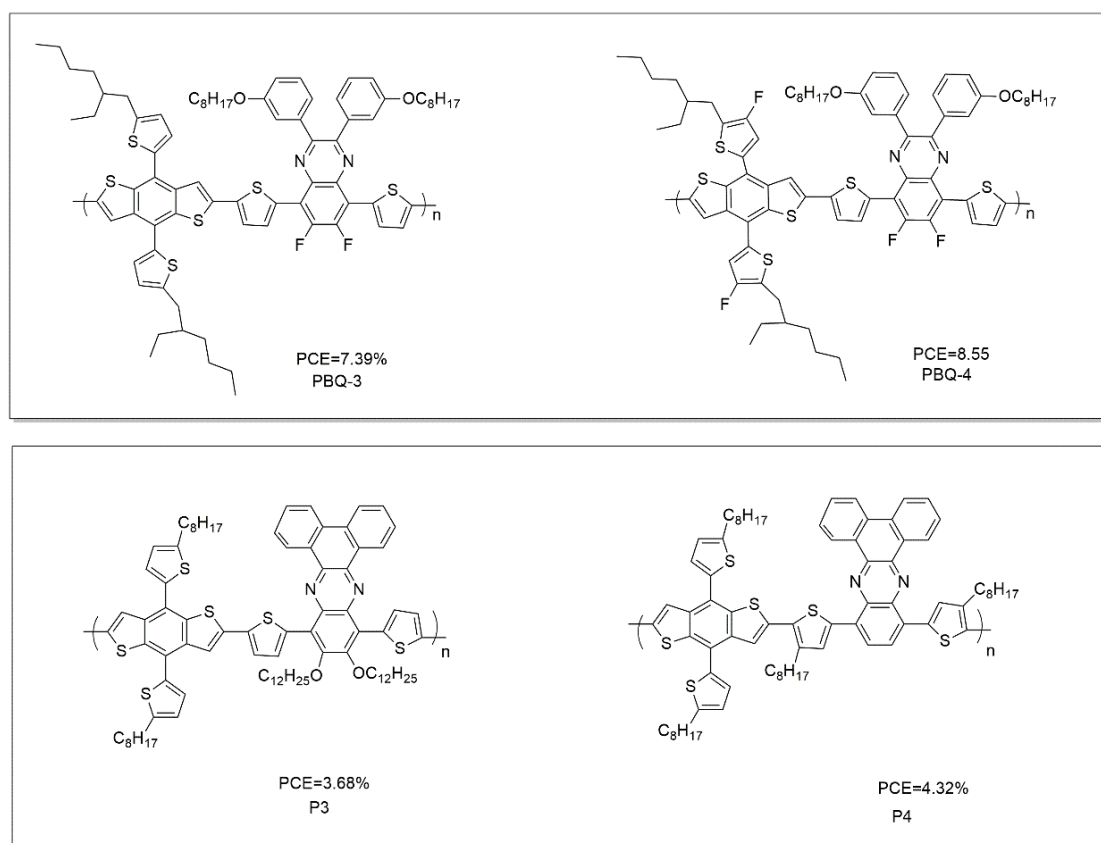


**Figure 1.13.** Chemical structures of literature examples including PBQ-3, PBQ-4, P3 and P4

### 1.10. Aim of the Study

Recently, conjugated polymers based on alternating donor-acceptor type solar devices have exhibited more research interest with promising photovoltaic performance. The reasonable selection and optimization of donor-acceptor units allow the band gap tuning as well as the light absorption abilities and energy levels of the active layer of the desired conjugated polymers for BHJ solar applications [39]. In this work, in order

to explore the relationship between chemical structure and photovoltaic performance of the solar devices that contain BDT and quinoxalines moieties, three conjugated polymers with alkylselenophene based BDT as the donor unit and thiophene substituted quinoxaline building blocks as the acceptor unit were synthesized via Stille coupling polycondensation reaction. In order to minimize steric interactions between D and A moieties 3-hexylthiophene as an  $\pi$  bridge were added between BDT and quinoxaline unities. The reason of introduction of selenophene side chain to the BDT unit is achieving high conductivity and mobility due to intermolecular Se-Se interactions [61]. Moreover, three different quinoxaline structures including fluorinated 2,3-diphenylquinoxaline, nonfluorinated 2,3-diphenylquinoxaline and phenanthrene based quinoxaline were coupled with selenophene substituted BDT in order to get better understanding for the structure-performance relationship also to achieve high PCE of OSCs. The effects of introducing fused structure and incorporation of an electron withdrawing F atom onto the quinoxaline units with respect to electrochemical, spectroelectrochemical studies were examined and compared.

The synthesized polymers were characterized by several techniques and also the photovoltaic and morphological properties of these polymers were carefully investigated. The molecular structures of polymers P1, P2 and P3 were shown in Figure 1.14.

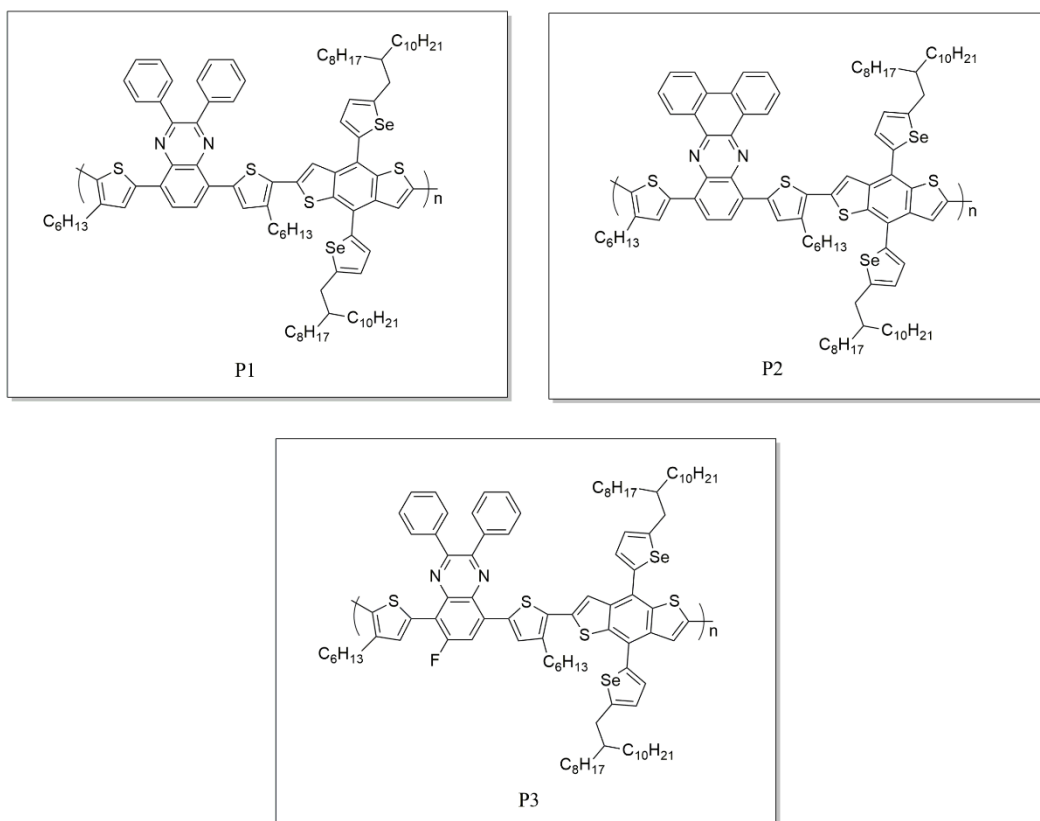


**Figure 1.14.** Chemical structures of synthesized polymers P1, P2 and P3

## CHAPTER 2

### EXPERIMENTAL

#### 2.1. Materials

All starting materials and reagents used in the synthesis of monomers and CPs were supplied from Sigma-Aldrich except selenophene which was purchased from TCI Korea. Tetrahydrofuran and toluene were dried over Na/benzophenone ketyl prior to use in reactions and other solvents were utilized without any drying process. Moisture and air sensitive reactions were carried out in the presence of nitrogen atmosphere in order to get inert medium. The synthesized products were chromatographically purified on column with Merck Silica Gel 60.

#### 2.2. Synthesis of Monomers

##### 2.2.1. Synthesis of tributyl(4-hexylthiophen-2-yl)stannane

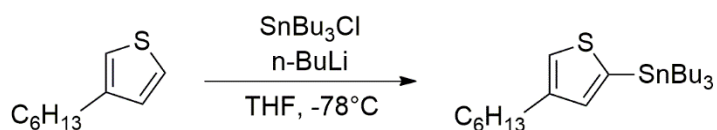


**Figure 2.1.** Synthetic route of tributyl(4-hexylthiophen-2-yl)stannane

In a 100-mL two neck round bottom flask 3-hexylthiophene (2.5 g, 14.85 mmol) was dissolved in dry THF (15 mL). Then, under argon atmosphere the reaction was cooled to -78 °C and 2.5 M n-BuLi in hexane (6.54 mL, 16.34 mmol) was added slowly to the reaction medium. The reaction was stirred for 1.5 hours and 1 M trimethyl tin chloride (SnMe<sub>3</sub>Cl) (16.34 mL, 16.34 mmol) was added drop wise to the mixture and stirred for another 1.5 hours under same conditions. Later, reaction medium was warmed to room temperature and subsequently stirred for 20 hours. The removal of solvent by rotary evaporation was performed and the mixture was extracted with water and diethyl ether three times. Then, combined organic layer was separated and dried with anhydrous Na<sub>2</sub>SO<sub>4</sub> for half an hour, filtered, and evaporated under vacuum yielded a yellowish liquid (6.54 g, 96%).

### 2.2.2. Synthesis of 4,7-dibromobenzo[c][1,2,5]thiadiazole

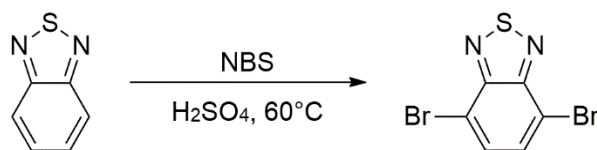


**Figure 2.2.** Synthetic route of 4,7-dibromobenzo[c][1,2,5]thiadiazole

Benzo-1,2,5-thiadiazole (2.00 g, 14.69 mmol) was dissolved in 20 mL of sulfuric acid (H<sub>2</sub>SO<sub>4</sub>) in a single neck round bottom reaction flask. Then, the bromination agent N-bromosuccinimide (NBS) (5.23 g, 29.37 mmol) was added portion by portion to the reaction medium. After, temperature was raised up to 60 °C and reaction was stirred in an oil bath for overnight. The cooled reaction mixture was filtered, and solid residue was washed with cold distilled water (100 mL). The solid product was filtered and recrystallized with ethanol several times. Isolated product was collected as a white solid (3.60 g, 83%).

### 2.2.3. Synthesis of 3,6-dibromo-1,2-benzenediamine

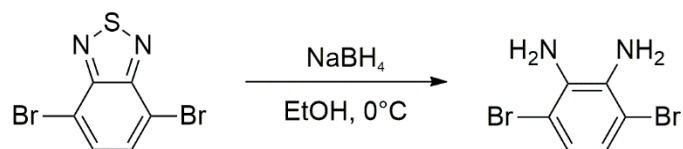


**Figure 2.3.** Synthetic route of 3,6-dibromo-1,2-benzenediamine

4,7-Dibromo-benzo[*c*][1,2,5]thiadiazole (3.00 g, 10.21 mmol) was put in a two neck round bottom flask and then 400 ml ethanol was added. Then NaBH<sub>4</sub> (5.79 g, 153.08 mmol) was added portion by portion to the reaction intermediate at 0 °C in an ice bath. After completion of addition of sodium borohydride, the reaction was stirred at room temperature for 20 hours. Solvent removal was performed under reduced pressure then, product was extracted with diethyl ether and brine four times. The organic layer was dried over Na<sub>2</sub>SO<sub>4</sub> and the solvent was removed under reduced pressure. The procedure gave product as a yellow solid (2.50 g, 92%).

### 2.2.4. Synthesis of 5,8-dibromo-2,3-diphenylquinoxaline

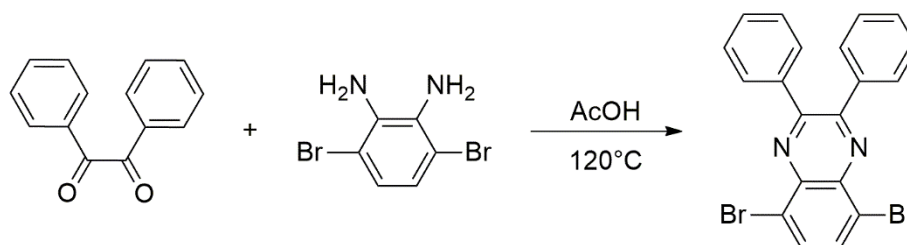


**Figure 2.4.** Synthetic route of 5,8-dibromo-2,3-diphenylquinoxaline

3,6-Dibromo-1,2-benzenediamine (0.50 g, 1.88 mmol) and benzil (0.43 g, 2.07 mmol) were putted in a 100-mL single neck flask and 25 mL glacial acetic acid was added carefully. The solution mixture was refluxed for 15 hours. The reaction was controlled by using thin layer chromatography (TLC). After cooling to room temperature, the solution was transferred into cold distilled water and washed with water several times to get rid of excess AcOH. The participation was filtered and recrystallized with ethanol to obtain pure product as pale yellow solid (0.73 g, 87%).

$^1\text{H}$  NMR (400 MHz,  $\text{CDCl}_3$ )  $\delta$  (ppm): 7.92 (s, 2H), 7.70 – 7.62 (m, 4H), 7.44 – 7.33 (m, 6H).  $^{13}\text{C}$  NMR (101 MHz,  $\text{CDCl}_3$ )  $\delta$  (ppm): 154.25, 139.42, 138.03, 133.10, 130.25, 129.58, 128.38, 123.73.

### 2.2.5. Synthesis of 5,8-bis(4-hexylthiophen-2-yl)-2,3-diphenylquinoxaline

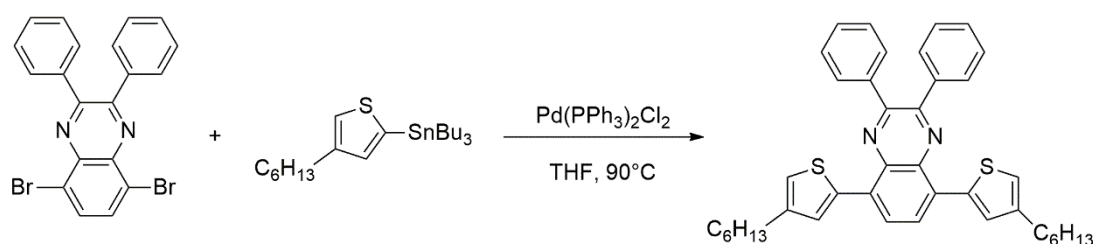


**Figure 2.5.** Synthetic route of 5,8-bis(4-hexylthiophen-2-yl)-2,3-diphenylquinoxaline

5,8-Dibromo-2,3-diphenylquinoxaline (0.50 g, 1.14 mmol), tributyl(4-hexylthiophen-2-yl)stannane (1.30 g, 2.84 mmol) and 35 mL freshly distilled THF were added in a 100 mL two neck flask under inert atmosphere. After, bubbling process were performed for 1 hour to the system the  $\text{Pd}(\text{PPh}_3)_2\text{Cl}_2$  (0.02 mg, 0.02 mmol) was added to the reaction mixture quickly. The reaction allowed to stir at  $90^\circ\text{C}$  for 2 days under argon atmosphere. After evaporation of solvent under vacuum, the product was

extracted with chloroform and water. The organic layer was dried by anhydrous  $\text{Na}_2\text{SO}_4$ . Removal of organic solvent by rotary evaporation was performed and crude product was purified by column chromatography with chloroform /hexane (3:7) to obtain faint orange solid (0.43 g, 61%).

$^1\text{H}$  NMR (400 MHz,  $\text{CDCl}_3$ )  $\delta$  (ppm): 8.10 (s, 2H), 7.75 (d,  $J = 10.0$  Hz, 6H), 7.38 (d,  $J = 6.2$  Hz, 6H), 7.11 (s, 2H), 2.69 (t,  $J = 7.7$  Hz, 4H), 1.75 – 1.67 (m, 4H), 1.44 – 1.30 (m, 12H), 0.91 (t,  $J = 6.4$  Hz, 6H).  $^{13}\text{C}$  NMR (101 MHz,  $\text{CDCl}_3$ )  $\delta$  (ppm): 151.47, 142.85, 138.75, 138.43, 137.33, 131.23, 130.49, 128.97, 128.20, 128.07, 126.96, 123.82, 76.71, 31.79, 30.61, 29.06, 22.67, 14.13.

#### 2.2.6. Synthesis of 5,8-bis(5-bromo-4hexylthiophen-2-yl)-2,3-diphenylquinoxaline

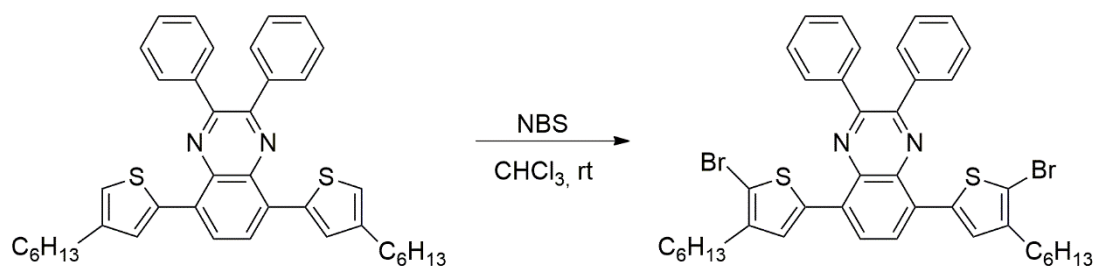


**Figure 2.6.** Synthetic route of 5,8-bis(5-bromo-4hexylthiophen-2-yl)-2,3 diphenyl quinoxaline

In a single neck round bottom flask 5,8-bis(4-hexylthiophen-2-yl)-2,3-diphenyl quinoxaline (0.35 g, 0.56 mmol) was dissolved in 25 mL chloroform, to which NBS (0.21 g, 1.20 mmol) was added portion by portion in dark at 0 °C. Then the solution was allowed to reach room temperature and stirred for 20 hours. After the completion of stirring process, the product was poured into  $\text{NaHCO}_3$  -water and extracted with

chloroform to get rid of excess NBS. Organic layer was filtered, dried over Na<sub>2</sub>SO<sub>4</sub> and lastly concentrated on rotary evaporator. Recrystallization with cold methanol yielded the crude product as a red-orange solid. (0.39 g, 88%).

<sup>1</sup>H NMR (400 MHz, CDCl<sub>3</sub>) δ (ppm): 8.03 (s, 2H), 7.70 (dd, *J* = 7.6, 1.8 Hz, 4H), 7.53 (s, 2H), 7.45 – 7.36 (m, 6H), 2.63 (t, 4H), 1.72 – 1.61 (m, 4H), 1.43 – 1.30 (m, 12H), 0.91 (t, *J* = 7.0 Hz, 6H). <sup>13</sup>C NMR (101 MHz, CDCl<sub>3</sub>) δ (ppm): 151.98, 141.30, 138.30, 137.63, 136.83, 130.55, 130.49, 129.15, 128.27, 126.56, 125.68, 114.17, 77.33, 77.01, 76.69, 31.69, 29.81, 29.59, 29.00, 22.63, 14.12.

### 2.2.7. Synthesis of 10,13-dibromodibenzo[*a,c*]phenazine

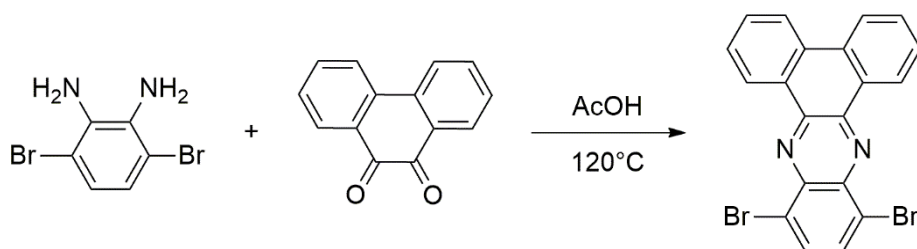


**Figure 2.7.** Synthetic route of 10,13-dibromodibenzo[*a,c*]phenazine

Phenanthrene-9,10-dione (0.30 g, 1.13 mmol) and 3,6-dibromo-1,2-benzenediamine (0.26 g, 1.24 mmol) were placed in a single neck round bottom flask and dissolved in 25 mL acetic acid then, the mixture was stirred for 16 h under reflux. After the reaction was completed, the solution was poured into cold distilled water (200 mL). The precipitate was filtered and recrystallized with ethanol to afford dark yellow solid (0.37 g, 76%).

<sup>1</sup>H NMR (400 MHz, CDCl<sub>3</sub>) δ (ppm): 9.46 (dd, *J* = 5.9, 2.0 Hz, 2H), 8.56 (d, *J* = 7.9 Hz, 2H), 8.03 (s, 2H), 7.87 – 7.75 (m, 4H).

### 2.2.8. Synthesis of 10,13-bis(4-hexylthiophen-2-yl)dibenzo[*a,c*]phenazine

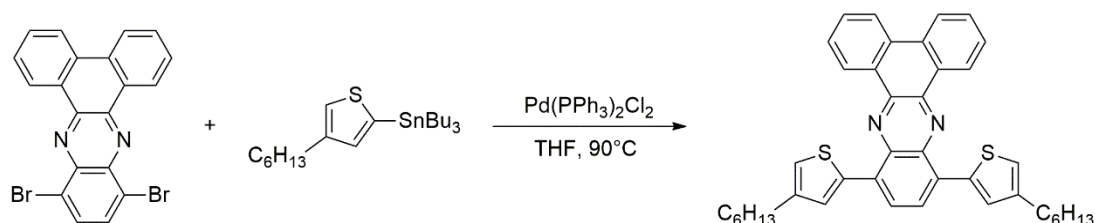


**Figure 2.8.** Synthetic route of 10,13-bis(4-hexylthiophen-2-yl)dibenzo[*a,c*]phenazine

10, 13-Dibromodibenzo[*a,c*]phenazine (0.50 g, 1.14 mmol) and tributyl(4-hexylthiophen-2-yl)stannane (1.30 g, 2.85 mmol) were dissolved in 40 mL freshly distilled THF in a 100 mL two necked flask. Before the addition of Pd(PPh<sub>3</sub>)<sub>2</sub>Cl<sub>2</sub> catalyst (16.02 mg, 0.03 mmol), the solution was purged several times with argon to get inert atmosphere for 1 hour. The reaction was stirred at 90 °C for 48 hours. After evaporation of solvent under vacuum, the product was partitioned between chloroform and water. The organic layer was dried by anhydrous Na<sub>2</sub>SO<sub>4</sub>. Removal of organic solvent by rotary evaporation was performed and crude product was purified by column chromatography on silica gel with chloroform /hexane (1:5) to obtain light red solid (0.43 g, 62%).

<sup>1</sup>H NMR (400 MHz, CDCl<sub>3</sub>) δ (ppm): 9.54 – 9.49 (m, 2H), 8.53 (d, *J* = 7.2 Hz, 2H), 8.16 (s, 2H), 7.78 – 7.73 (m, 6H), 7.23 (s, 2H), 2.75 (t, 4H), 1.82 – 1.73 (m, *J* = 15.0, 7.6 Hz, 6H), 1.43 – 1.34 (m, *J* = 7.3 Hz, 12H), 0.94 (t, *J* = 6.8 Hz, 6H). <sup>13</sup>C NMR (101 MHz, CDCl<sub>3</sub>) δ (ppm): 142.85, 141.68, 138.69, 138.55, 132.39, 131.58, 130.58, 130.34, 128.05, 128.00, 127.76, 126.91, 123.94, 122.89, 31.81, 30.69, 30.66, 29.17, 22.69, 14.16.

### 2.2.9. Synthesis of 10,13-bis(5-bromo-4-hexylthiophen-2-yl)dibenzo[*a,c*]phenazine

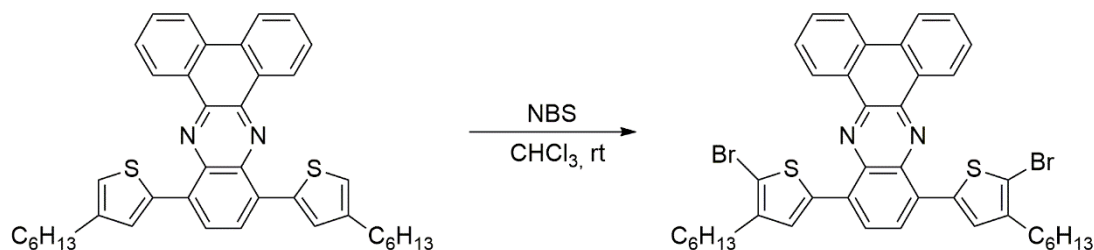


**Figure 2.9.** Synthetic route of 10,13-bis(5-bromo-4-hexylthiophen-2-yl)dibenzo[*a,c*]phenazine

In a single neck round bottom flask 10,13-bis(4-hexylthiophen-2-yl)dibenzo[*a,c*]phenazine (0.30 g, 0.50 mmol) was dissolved with 25 mL chloroform, to which NBS (0.17 g, 0.09 mmol) was added portion by portion in dark at 0 °C. Then the temperature of mixture was maintained at room temperature and reaction was stirred for overnight. After, the product was poured into NaHCO<sub>3</sub>-water and extracted with chloroform to get rid of excess NBS. Organic layer was filtered, dried over Na<sub>2</sub>SO<sub>4</sub> and lastly condensed on rotary evaporator. Through recrystallization of crude product with methanol a shiny brown-red solid was afforded (0.27 g, 72%).

<sup>1</sup>H NMR and <sup>13</sup>C NMR results could not be achieved for this molecule since the fused structure hampers the solubility of monomer in the common solvents.

### 2.2.10. Synthesis of 3,6-dibromo-4-fluorobenzene-1,2-diamine

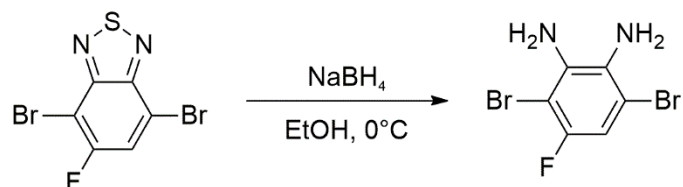


**Figure 2.10.** Synthetic route of 3,6-dibromo-4-fluorobenzene-1,2-diamine

4,7-Dibromo-5-fluorobenzo[*c*][1,2,5]thiadiazole (0.6 g, 1.92 mmol) was weighed in a two neck round bottom flask then 100 mL ethanol was added. Then, sodium borohydride (0.73 g, 19.23 mmol) was added portion wise to the reaction medium which was placed in ice bath at 0 °C. The reaction was stirred at room temperature for 16 hours. The crude product was quenched with water (200 mL) and extracted with diethyl ether. Firstly, organic layer filtered, dried over sodium sulfate and then solvent was vaporized by rotary evaporation to afford brownish yellow solid (0.40 g, 73%).

### 2.2.11. Synthesis of 5,8-dibromo-6-fluoro-2,3-diphenylquinoxaline

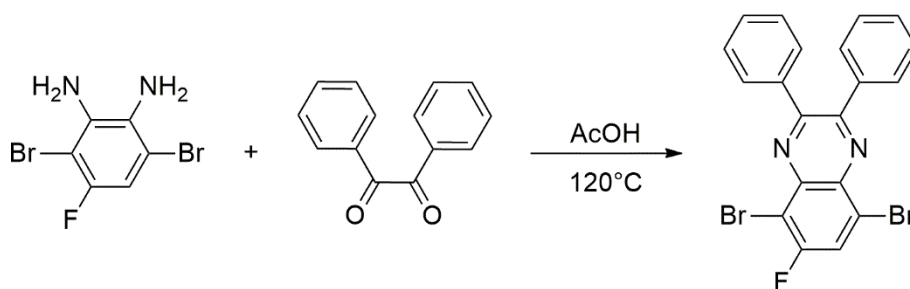


**Figure 2.11.** Synthetic route of 5,8-dibromo-6-fluoro-2,3-diphenylquinoxaline

A mixture of 3,6-dibromo-4-fluorobenzene-1,2-diamine (0.30 g, 1.06 mmol), benzil (0.24 g, 1.16 mmol) and 20 mL acetic acid was refluxed for 20 hours. After cooling, the solution was poured into ice-water and the product was extracted with chloroform three times. The organic layer was dried over Na<sub>2</sub>SO<sub>4</sub> and the solvent was removed under vacuum by using rotary evaporator. The compound was purified by column chromatography eluting with CHCl<sub>3</sub>/hexane (1:1) and pale-yellow solid were obtained (0.27 g, 56%).

<sup>1</sup>H NMR (400 MHz, CDCl<sub>3</sub>) δ (ppm): 7.94 (d, *J* = 8.0 Hz, 1H), 7.68 – 7.62 (m, 4H), 7.43 – 7.34 (m, 6H). <sup>13</sup>C NMR (101 MHz, CDCl<sub>3</sub>) δ (ppm): 154.62, 137.82, 137.74, 130.26, 130.16, 129.75, 129.56, 128.38, 123.35, 123.06.

### 2.2.12. Synthesis of 5,8-bis(4-hexylthiophen-2-yl)-6-fluoro-2,3-diphenylquinoxaline

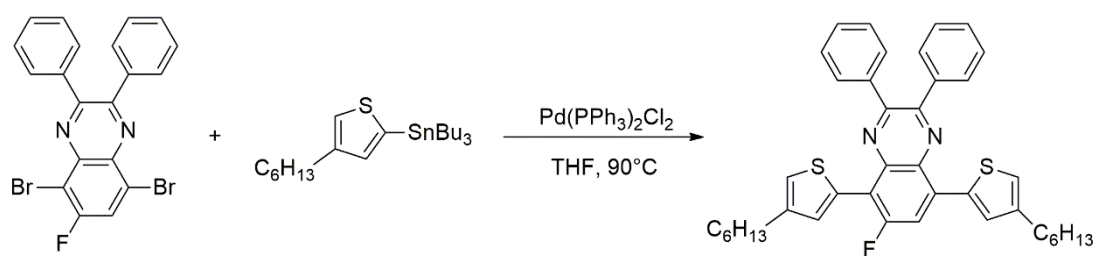


**Figure 2.12.** Synthetic route of 5,8-bis(4-hexylthiophen-2-yl)-6-fluoro-2,3-diphenyl quinoxaline

5,8-Dibromo-6fluoro-2,3-diphenylquinoxaline (0.26 g, 0.57 mmol), tributyl(4-hexylthiophen-2-yl)stannane (0.65 g, 1.42 mmol) were putted into a 100 mL two neck round bottom flask and then they were dissolved in degassed THF. After the addition of catalyst Pd(PPh<sub>3</sub>)<sub>2</sub>Cl<sub>2</sub> (8.00 mg, 0.01mmol), the solution was bubbled with nitrogen gas and heated to 90 °C under inert atmosphere for 46 hours. The resulting reaction was extracted with DCM and water and the combined organic phases were filtered and dried over Na<sub>2</sub>SO<sub>4</sub>. Later, solvent removal process was performed under reduced

pressure, the product was purified by silica based column chromatography eluting with hexane/CH<sub>2</sub>Cl<sub>2</sub> (5:1) to afford orange crystals (0.28 g, 78%).

<sup>1</sup>H NMR (400 MHz, CDCl<sub>3</sub>) δ (ppm): 7.95 (d, *J* = 13.4 Hz, 1H), 7.86 (s, 1H), 7.81 – 7.71 (m, 5H), 7.53 – 7.31 (m, 7H), 7.17 (d, 1H), 2.69 (dd, *J* = 15.9, 8.3 Hz, 4H), 1.76 – 1.68 (m, 4H), 1.45 – 1.31 (m, 12H), 0.91 (t, *J* = 6.9 Hz, 6H). <sup>13</sup>C NMR (101 MHz, CDCl<sub>3</sub>) δ (ppm): 140.69, 140.31, 136.26, 136.17, 128.30, 128.19, 126.87, 126.72, 126.39, 125.97, 122.67, 121.96, 29.50, 28.33, 28.27, 26.85, 26.81, 25.92, 24.54, 20.39, 15.11, 11.87, 11.33

### 2.2.13. Synthesis of 5,8-bis(5-bromo-4-hexylthiophen-2-yl)-6-fluoro-2,3-diphenylquinoxaline

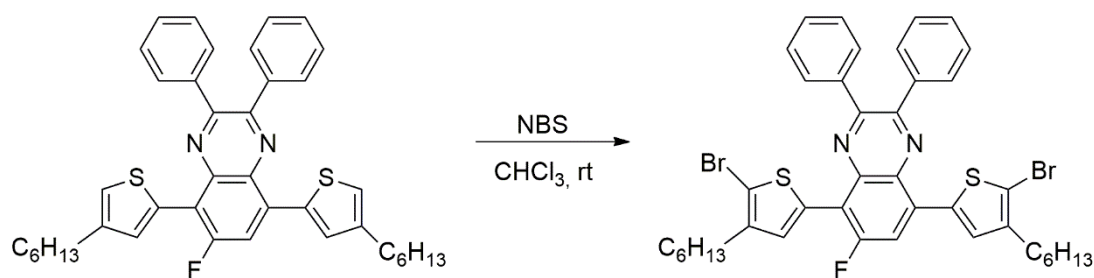


**Figure 2.13.** Synthetic route of 5,8-bis(5-bromo-4-hexylthiophen-2-yl)-6-fluoro-2,3-diphenylquinoxaline

6-Fluoro-5,8-bis(4-hexylthiophen-2-yl)-2,3-diphenylquinoxaline (0.25 g, 0.4 mmol) was dissolved in 15 mL of CHCl<sub>3</sub>. N-bromosuccinimide (NBS) (0.15 g, 0.8 mmol) was added slowly to the reaction intermediate in the dark at 0 °C. After that, the mixture was stirred at room temperature for 24 hours. The product was extracted four times with chloroform:water. The organic phases were filtered and dried over Na<sub>2</sub>SO<sub>4</sub> and condensed by using rotary evaporator under reduced pressure. The product was

chromatographically purified on column eluting with ethyl acetate/hexane (1:30). This procedure gave product as a shiny orange solid. (0.24 g, 76%)

$^1\text{H}$  NMR (400 MHz,  $\text{CDCl}_3$ )  $\delta$  (ppm): 7.74 (d,  $J = 13.8$  Hz, 1H), 7.67 – 7.53 (m, 5H), 7.45 – 7.24 (m, 7H), 2.63 – 2.48 (m, 4H), 1.63 – 1.54 (m, 4H), 1.39 – 1.21 (m, 12H), 0.83 (t,  $J = 6.6$  Hz, 6H).  $^{13}\text{C}$  NMR (101 MHz,  $\text{CDCl}_3$ )  $\delta$  (ppm): 152.41, 151.14, 141.38, 137.99, 136.31, 136.07, 130.59, 130.48, 129.31, 128.29, 116.26, 115.76, 115.63, 115.19, 77.34, 77.02, 76.70, 31.69, 29.80, 29.61, 29.02, 22.65, 14.13.

#### 2.2.14. Synthesis of 9-(bromomethyl)nonadecane

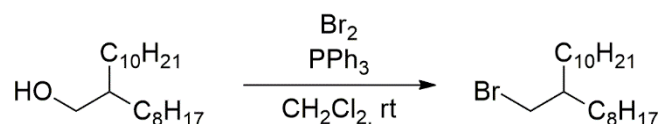


**Figure 2.14.** Synthetic route of 9-(bromomethyl)nonadecane

2-Octyl-1-dodecanol (6.00 g, 20.10 mmol) was dissolved in 60 mL dichloromethane at 0 °C. After dissolving process was completed, triphenylphosphine (PPh<sub>3</sub>) (5.80 g, 22.11 mmol) was added. Then, slow addition of bromine (6.74 g, 42.20 mmol) was done carefully and mixture was stirred for 1 hour at 0 °C. Subsequently, the temperature was maintained to room temperature and reaction was stirred for 28 hours. To get rid of the excess bromine, concentrated NaHSO<sub>3</sub> solution was poured into the reaction mixture. The solution was partitioned between DCM and brine. The CH<sub>2</sub>Cl<sub>2</sub> layer was separated and dried over Na<sub>2</sub>SO<sub>4</sub>. The evaporation of solvent under reduced pressure afforded a white solid product which was purified chromatographically on silica gel using hexane as the eluent. The obtained crude product was a colorless oil like liquid (6.50 g, 89%).

### 2.2.15. Synthesis of 2-(2-octyldodecyl)selenophene

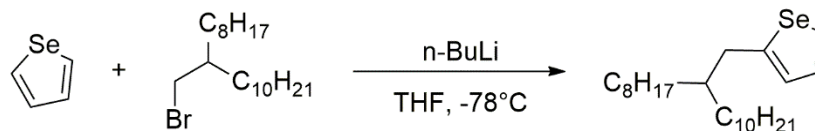


**Figure 2.15.** Synthetic route of 2-(2-octyldodecyl)selenophene

Selenophene (2.50 g, 15.26 mmol) was dissolved in dry THF (60 mL) under inert atmosphere. The solution was cooled down to -78 °C before the addition of 2.5 M (in hexane) *n*-butyllithium (6.11 mL, 15.26 mmol). After the drop wise addition of *n*-BuLi was completed, the solution was stirred for 1.5 hours. The alkyl chain 9-(bromomethyl) nonadecane (5.52 g, 15.26 mmol) was added drop wise slowly under same conditions. Then, temperature was raised to 80 °C and stirred for 15 hours. The solution was hydrolyzed with saturated NH<sub>4</sub>Cl and extraction was performed with diethyl ether. The organic phase was combined, filtered and dried over anhydrous sodium sulfate. The solvent removal was done by using rotary evaporator and the residue was purified by column chromatography technique eluting with hexane. Isolated product was obtained as a clear yellow oil (1.82 g, 57%).

<sup>1</sup>H NMR (400 MHz, CDCl<sub>3</sub>) δ (ppm): 7.81 (d, J = 4.6 Hz, 1H), 7.13 (dd, J = 5.6, 3.6 Hz, 1H), 6.92 (d, J = 2.7 Hz, 1H), 2.83 (d, J = 6.5 Hz, 2H), 1.64 – 1.51 (m, 1H), 1.44 – 1.16 (m, 32H), 0.90 (t, J = 6.7 Hz, 6H). <sup>13</sup>C NMR (101 MHz, CDCl<sub>3</sub>) δ (ppm): 151.98, 128.97, 128.19, 127.29, 40.83, 36.92, 33.95, 33.16, 31.96, 31.61, 30.81, 29.99, 29.88, 29.69, 29.59, 29.39, 29.37, 26.77, 26.62, 22.73, 14.15.

### 2.2.16. Synthesis of 4,8-bis(5(2-octyldodecyl)selenophen-2-yl)benzo[1,2-b:4,5-b'] dithiophene

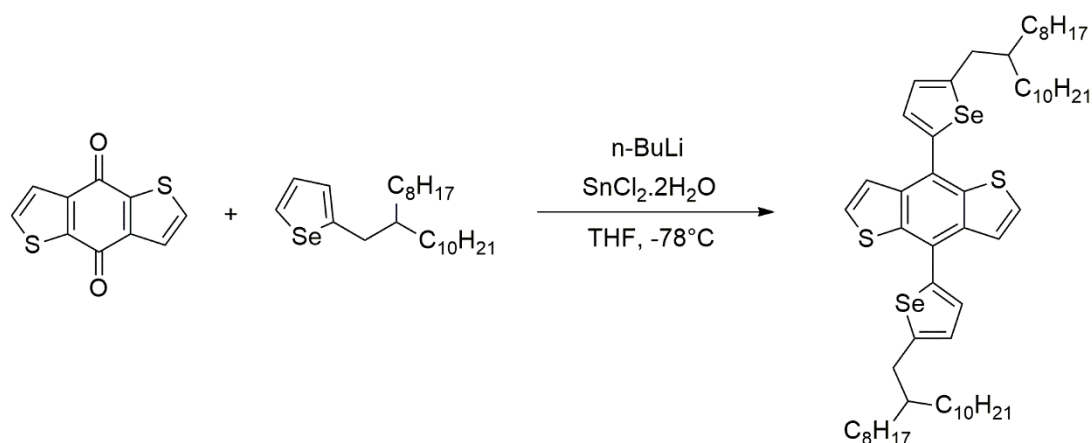


**Figure 2.16.** Synthetic route of 4,8-bis(5(2-octyldodecyl)selenophen-2-yl)benzo[1,2-b:4,5-b']dithiophene

In a 100 mL two neck round bottom flask, 2-(2-octyldodecyl) selenophene (1.68 g, 4.09 mmol) was dissolved with 50 mL degassed THF. Slow addition of 2.5 M  $n\text{-BuLi}$  (2.18 mL, 5.45 mmol) was done at  $-78^\circ\text{C}$  under inert atmosphere. After that, temperature was increased to  $50^\circ\text{C}$  and the mixture was stirred for 1.5 hours. In the next step, the benzo[1,2-b:4,5-b'] dithiophene-4,8-dione (0.30 g, 1.36 mmol) was added to the solution in one portion and the solution was stirred for another 1.5 hours before being cooled to  $25^\circ\text{C}$ . After the completion of cooling process,  $\text{SnCl}_2 \cdot 2\text{H}_2\text{O}$  (2.35 g, 11.30 mmol) was dissolved in 10 mL HCl (10%) and the mixture was added directly into the reaction medium and mixture was further stirred for overnight. The mixture was quenched with ice water and extraction was performed by using diethyl ether as an organic solvent. The extracted organic phase was washed with brine, dried with sodium sulfate and the evaporation of solvent under reduced pressure was done. Purification step was achieved by silica gel column chromatography eluting with

hexane. Purified crude product was obtained as a sticky brownish yellow oil (0.85 g, 61%).

$^1\text{H}$  NMR (400 MHz,  $\text{CDCl}_3$ )  $\delta$  7.66 (d,  $J = 5.7$  Hz, 2H), 7.44 (d,  $J = 5.6$  Hz, 2H), 7.40 (d,  $J = 3.6$  Hz, 2H), 7.03 (d,  $J = 3.6$  Hz, 2H), 2.91 (d,  $J = 6.5$  Hz, 4H), 1.73 – 1.66 (m, 2H), 1.41 – 1.24 (m, 64H), 0.91 – 0.86 (m, 12H).  $^{13}\text{C}$  NMR (101 MHz,  $\text{CDCl}_3$ )  $\delta$  153.89, 142.77, 138.81, 136.24, 130.02, 127.54, 127.39, 126.28, 123.53, 40.81, 37.44, 33.36, 31.97, 30.02, 29.71, 29.68, 29.41, 26.69, 22.73, 14.16.

### 2.2.17. Synthesis of 4,8-bis(5(2-octyldodecyl)selenophen-2-yl)benzo[1,2-*b*:4,5-*b'*] dithiophene-2,6-diyl)bis(trimethylstannane)

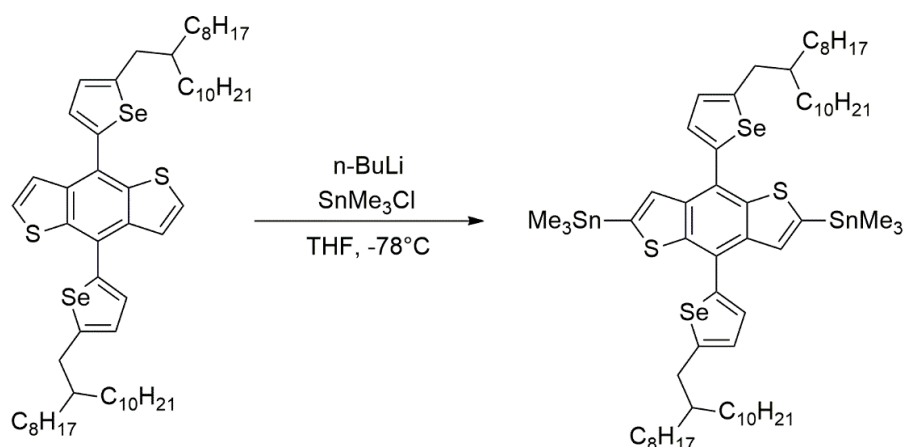


**Figure 2.17.** Synthetic route of 4,8-bis(5(2-octyldodecyl)selenophen-2-yl)benzo[1,2-*b*:4,5-*b'*] dithiophene-2,6-diyl)bis(trimethylstannane)

In a dry 100 ml round bottom flask, compound 4,8-bis(5(2-octyldodecyl)selenophen-2-yl)benzo[1,2-*b*:4,5-*b'*]dithiophene (0.80 g, 0.79 mmol) was dissolved in degassed THF (30 mL) under inert atmosphere. The temperature of medium was maintained at  $-78^\circ\text{C}$  using a dry ice-acetone, and 2.5 M *n*-butyllithium (0.9 mL, 2.38 mmol) was added drop wise to the reaction intermediate under same conditions. The solution was

heated up to room temperature while stirring for 20 minutes. Before the green color disappears, trimethyltin chloride (2.54 mL, 2.54 mmol) was added in one portion and the mixture was turned into pale yellow color. After that, the solution was quenched with ice water and it was partitioned between diethyl ether and brine. The combined organic phase was separated, dried ( $\text{Na}_2\text{SO}_4$ ) and the solvent was removed under reduced pressure. Isolated donor compound was obtained as viscous yellowish-brown liquid (0.96 g, 90%).

$^1\text{H}$  NMR (400 MHz,  $\text{CDCl}_3$ )  $\delta$  7.74 (s,  $J = 14.8$  Hz, 2H), 7.46 (d,  $J = 3.6$  Hz, 2H), 7.07 (d,  $J = 3.6$  Hz, 2H), 2.95 (d,  $J = 6.5$  Hz, 4H), 1.82 – 1.69 (m, 2H), 1.35 – 1.28 (m, 64H), 0.85 – 0.80 (m, 12H), 0.50 – 0.37 (m, 18H).  $^{13}\text{C}$  NMR (101 MHz,  $\text{CDCl}_3$ )  $\delta$  153.51, 143.66, 142.19, 138.94, 137.06, 131.35, 129.82, 127.50, 124.63, 40.77, 37.49, 33.45, 31.97, 30.07, 29.74, 29.41, 29.31, 29.19, 27.45, 27.29, 26.76, 22.74, 14.15, 13.75, 9.49, 8.77.

## 2.3. Synthesis Polymers

### 2.3.1. Synthesis of P1

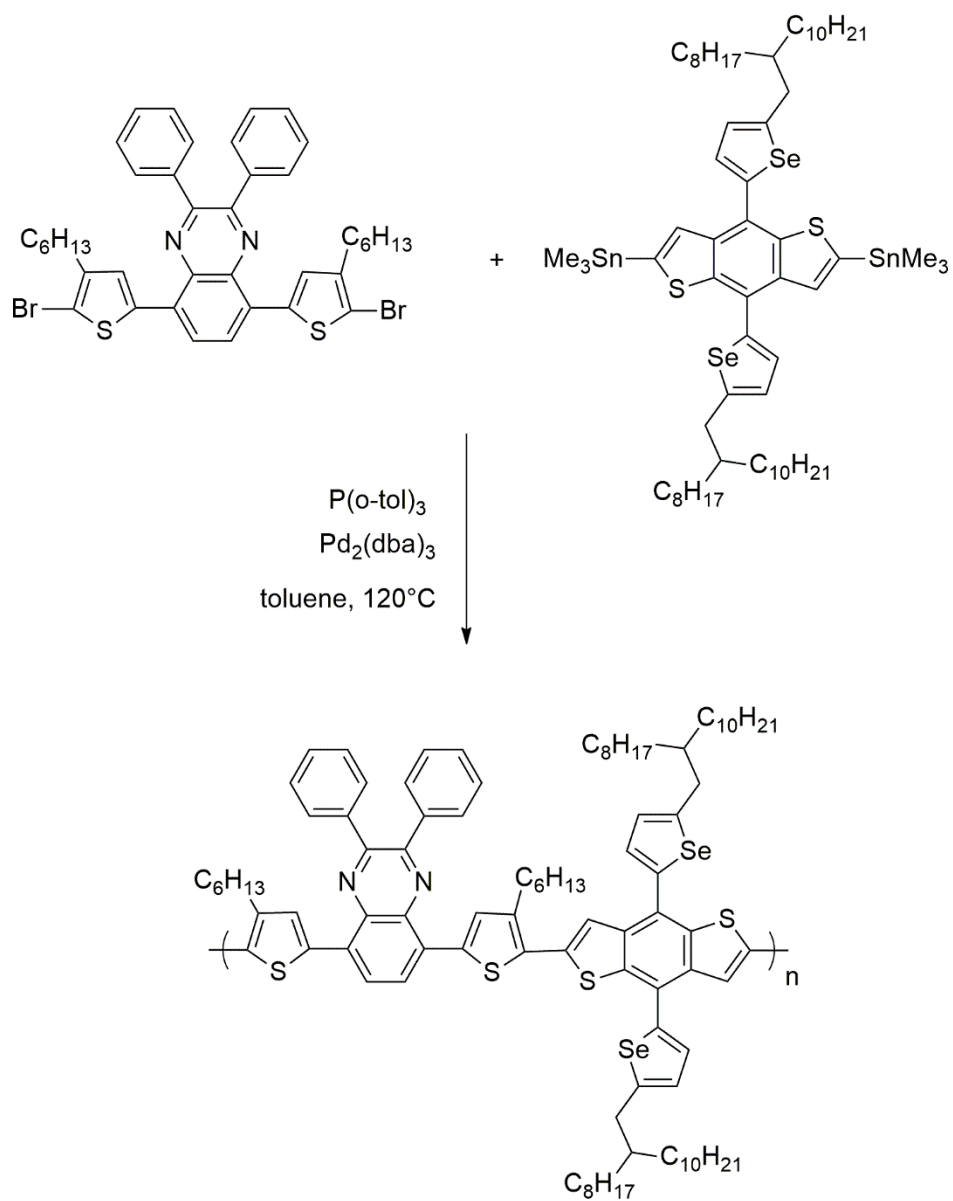


**Figure 2.18.** Synthetic route of P1

In a two neck 25 mL flask, 4,8-bis(5(2-octyldodecyl)selenophen-2-yl)benzo[1,2-*b*:4,5-*b'*]dithiophene-2,6-diyl)bistrimethylstannane) (0.17 g, 0.13 mmol) and 5,8-bis(5-bromo-4-hexylthiophen-2-yl)-2,3-diphenylquinoxaline (0.10 g, 0.13 mmol) were charged and compounds were dissolved in freshly distilled toluene 10 mL. The reaction mixture was deaerated under vacuum, purged with nitrogen gas. The bubbling process was performed for 1 hour to the reaction medium prior to addition of two different catalysts; tris(dibenzylideneacetone)dipalladium (0) ( $\text{Pd}_2(\text{dba})_3$ ) (0.006 g, 0.007 mmol) and tris(*o*-tolyl)phosphine ( $\text{P}(\text{o-tol})_3$ ) (0.01 g, 0.045 mmol). After the addition of catalysts were completed, the reaction mixture was heated up to 120 °C and stirred for 46 hours under inert atmosphere. Then, 2-bromothiophene (0.04 mg, 0.26 mmol) and 2-tributylstanylthiophene (0.10 g, 0.26 mmol) were added to the reaction intermediate to end-cap the polymer chain. After cooling to room temperature (25 °C), the resulting solution was poured into cold methanol. The precipitate was subjected to Soxhlet extraction with methanol, acetone, hexane, and chloroform respectively. The small amount of quadrasil (10 mg) was added to the chloroform extract as a scavenger and the extract was purified by the silica gel column. Lastly,  $\text{CHCl}_3$  fraction was condensed by evaporation, precipitated into 250 mL methanol and filtered by vacuum to afford the desired polymer as purple solid (0.12 g, 56%).

GPC analysis: The number-average molecular weight ( $M_n$ ) P1 is found as 12 kDa and the weight average molecular weight ( $M_w$ ) is detected as 16 kDa with 1.3 polydispersity index (PDI).

### 2.3.2. Synthesis of P2

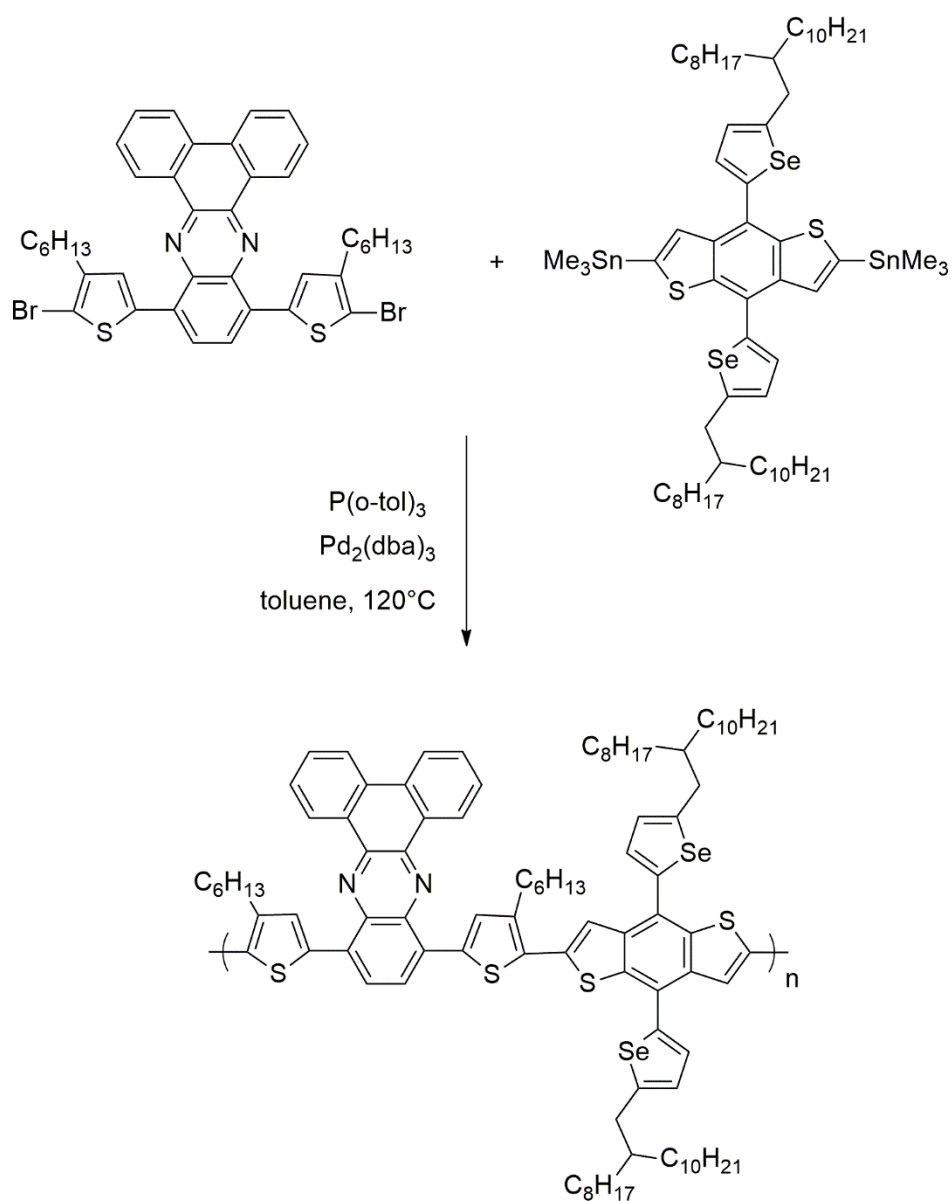


**Figure 2.19.** Synthetic route of P2

4,8-Bis(5(2-octyldodecyl)selenophen-2-yl)benzo[1,2-*b*:4,5-*b'*]dithiophene-2,6-diyl bistrimethylstannane) (0.16 g, 0.12 mmol) and 10,13-bis(5-bromo-4-hexylthiophen-2-yl)dibenzo[*a,c*]phenazine (0.09 g, 0.12 mmol) were putted in a two neck 25 mL flask and compounds were dissolved in dry toluene (10 mL). The reaction mixture

was deaerated under vacuum, backfilled with nitrogen gas and bubbled for 1 hour before the addition of tris(dibenzylideneacetone)dipalladium (0) ( $\text{Pd}_2(\text{dba})_3$ ) (0.005 g, 0.006 mmol) and tris(o-tolyl)phosphine ( $\text{P}(\text{o-tol})_3$ ) (0.01g, 0.045mmol). After the addition of two catalysts, the reaction temperature was set to 120 °C and the mixture was stirred for 50 hours under inert atmosphere. Subsequently, two separate end-cappers 2-bromothiophene (0.04 mg, 0.26 mmol) and 2-tributylstanylthiophene (0.10 g, 0.26 mmol) were added to the reaction medium respectively. After cooling to room temperature (25 °C), the resulting polymer was poured into cold methanol and precipitated. Soxhlet extraction was done for purification of precipitate eluting with methanol, acetone, hexane, and chloroform. Then, the quadrasil (10 mg) was added to the chloroform solution and the mixture was stirred about 2 hours. After stirring process, the product was passed through silica gel. The chloroform fraction was condensed by evaporation, precipitated into 250 mL methanol and filtered by vacuum in order to obtain the corresponding polymer as dark green solid (0.10 g, 51%).

GPC analysis: The number-average molecular weight ( $M_n$ ) P2 is found as 7 kDa and the weight average molecular weight ( $M_w$ ) is detected as 9 kDa with 1.3 poly dispersity index (PDI).

### 2.3.3. Synthesis of P3

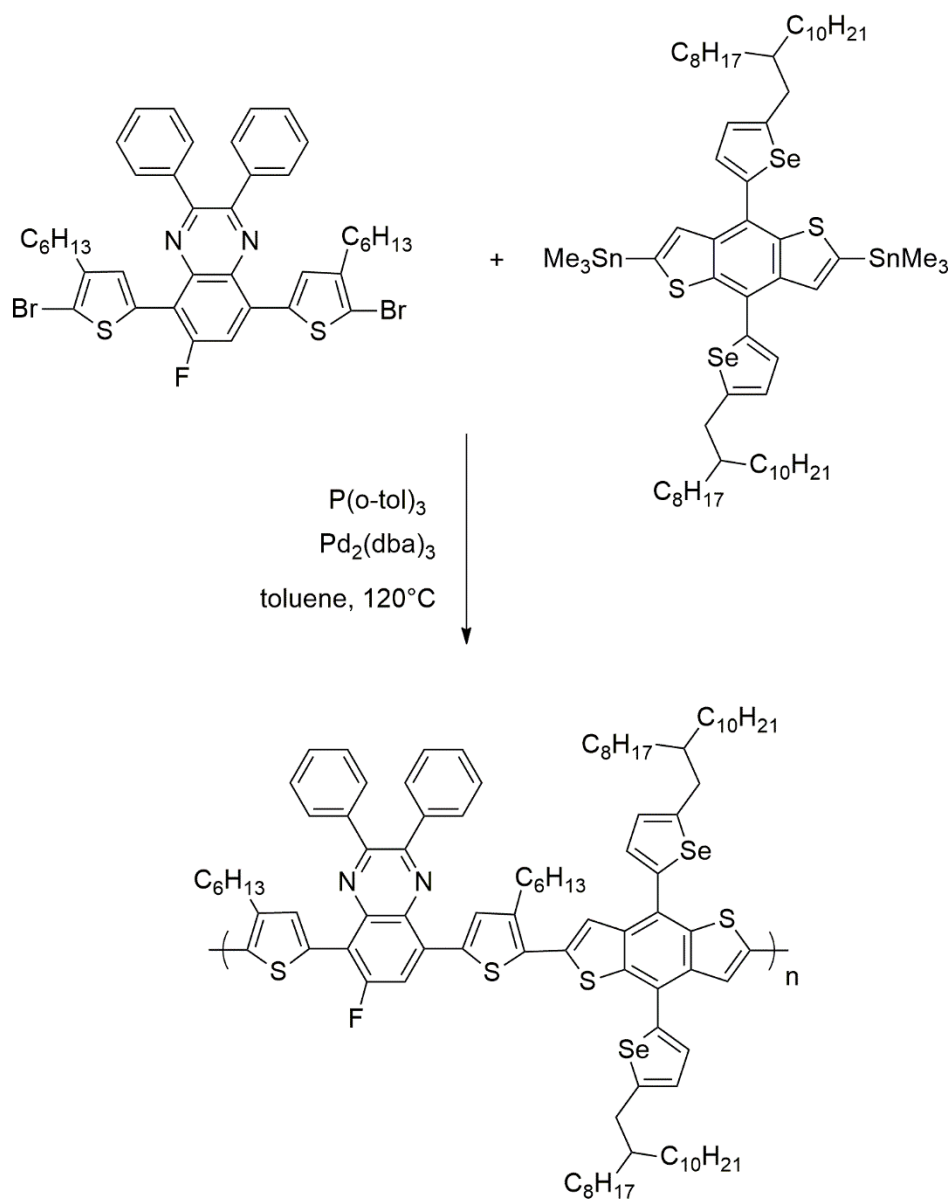


Figure 2.20. Synthetic route of P3

4,8-Bis(5(2-octyldodecyl)selenophen-2-yl)benzo[1,2-*b*:4,5-*b'*]dithiophene-2,6-diyl bistrimethylstannane) (0.18 g, 0.14 mmol) and 5,8-bis(5-bromo-4-hexylthiophen-2-yl)-6-fluoro-2,3-diphenylquinoxaline (0.11 g, 0.14 mmol) were charged in a two neck

25 mL flask and compounds were dissolved in degassed toluene (10 mL). The reaction mixture was deaerated under vacuum, backfilled with nitrogen gas and bubbled for 1 hour prior to addition of two different catalysts tris(dibenzylideneacetone)dipalladium(0) ( $\text{Pd}_2(\text{dba})_3$ ) (0.006 g, 0.007 mmol) and tris(o-tolyl)phosphine ( $\text{P}(\text{o-tol})_3$ ) (0.02g, 0.05 mmol). After the addition of catalyst was completed, the reaction mixture warmed to 120 °C in an oil bath and stirred for 2 days under inert atmosphere. After that, two different end cappers namely 2-bromothiophene (0.04 mg, 0.26 mmol) and 2-tributylstanylthiophene (0.10 g, 0.26 mmol) were added to the reaction intermediate. The resulting mixture was precipitated into cold methanol. The precipitate was subjected to Soxhlet extraction with methanol, acetone, hexane, and chloroform respectively. After the addition of little amount of quadrasil, the chloroform fraction was purified by passing through silica gel and then it was condensed by evaporation, precipitated into 300 mL methanol and filtered by vacuum to afford the corresponding polymer as purple solid (0.14 g, 63%).

GPC analysis: The number-average molecular weight ( $M_n$ ) P3 is found as 10kDa and the weight average molecular weight ( $M_w$ ) is detected as 15 kDa with 1.5 polydispersity index (PDI).

## **2.4. Characterization of Conducting Polymers**

### **2.4.1. Nuclear Magnetic Resonance Spectroscopy**

Structures of synthesized molecules were characterized via Nuclear Magnetic Resonance Spectroscopy technique (NMR) and both hydrogen NMR and carbon NMR shifts were detected using Bruker Spectrospin Avance DPX-400 Spectrometer in chloroform-d ( $\text{CDCl}_3$ ) solutions. The chemical shifts of  $^1\text{H}$  NMR and  $^{13}\text{C}$  NMR are presented in the unit of ppm with respect to internal reference namely tetramethyl silane (TMS). According to TMS reference in which peak signal was stated at 0 ppm, the chemical peaks signals of  $^1\text{H}$  NMR and  $^{13}\text{C}$  NMR in the deuterated chloroform were observed at 7.26 ppm and 77 ppm respectively.

### **2.4.2. Gel Permeation Chromatography**

Gel permeation chromatography (GPC) is a type separation technique yielding molecular weight of polymers. GPC is the only mechanism available to calculate molecular weight distribution and polydispersity index (PDI) of the synthesized polymer molecules in a chloroform solution (2.0 mg /mL). This instrument contains mobile phase and stationary phase that are liquid and solid respectively. The data which obtained from the chromatogram were compared to calibrated polystyrene (PS) standards by this way elution behaviors of polymers were achieved. GPC provides short time analysis with good sensitivity and narrow bands in order to derive weight average molecular weight ( $M_w$ ) of the polymers.

### **2.4.3. Electrochemical Studies**

Electrochemical studies of conjugated polymers were performed via Cyclic voltammetry (CV) in order to determine redox behaviors of polymers. Also, HOMO-LUMO level of polymers were estimated utilizing cyclic voltammograms. Electrochemical experiment set up was consisted of three electrode system in which Ag wire is the reference electrode (RE), platinum wire is the counter electrode (CE) and lastly Indium Tin Oxide (ITO) coated glass is the working electrode (WE). The synthesized polymers were spray coated onto working electrode by Omni coating gun and then coated ITO was immersed in acetonitrile (ACN) solution with 0.1 M tetrabutylammonium hexafluorophosphate (TBAPF<sub>6</sub>). In this technique, suitable cyclic potential was carried out at a constant scan rate (100 mV/s) using Gamry Instrument Reference 600 Potentiostat to investigate n and p doping potentials and color changes of polymers. Cyclic voltammograms of polymers gave the graph of current density ( $\text{mA}/\text{cm}^2$ ) versus voltage (V). Onset oxidation potential and onset reduction potential that were recorded from the graph showed LUMO and HOMO levels of the polymer respectively. As it was mentioned previously, the energy difference between HOMO and LUMO gave electronic band gap ( $E_g^{\text{el}}$ ) of conjugated polymers and these values were calculated by CV measurements.

#### 2.4.4. Spectroelectrochemical Studies

Doping process generates positive charges namely polarons and bipolarons to ensure conduction in conjugated polymers and these positive charges and neutral state of polymers are investigated with the help of spectroelectrochemical studies. For this thesis, spectroelectrochemical results of polymers were accomplished using Varian Cary 5000 UV-Vis Spectrometer. As name recalls spectroelectrochemical analysis contains both electrochemical and spectroscopic measurements. Experimental set up of these instruments consisted of three electrode system and spectroscopic measurements were demonstrated the UV Vis NIR spectra of polymers as a function of applied voltage. From these spectra, radical carriers via p-doping, maximum absorption wavelength ( $\lambda_{\text{max}}$ ) and optical band gap ( $E_{\text{g}}^{\text{op}}$ ) of polymers were detected.  $E_{\text{g}}^{\text{op}}$  was determined from onset point ( $\lambda_{\text{onset}}$ ) by taking tangent line of the  $\pi$ - $\pi^*$  interband transition where the absorption process was started for the polymers. Additionally, electrochromic properties of conducting polymers were investigated. Following equation represents calculation of  $E_{\text{g}}^{\text{op}}$ ;

$$E_{\text{g}}^{\text{op}} = \frac{1241}{\lambda_{\text{onset}}}$$

#### 2.4.5. Kinetic Studies

Kinetic studies were performed to gain insightful information about the transmittance change especially switching time and optical contrast of the synthesized polymers as a function of time under applied potential. Switching time refers to time needed for polymeric materials to switch from one redox state to another, whereas optical contrast shows the difference between percent transmittance (T%) of two extreme states of polymers which are reduced and oxidized states. Experimental set up comprised of square wave potential with optical spectroscopy and chronoamperometry. Polymer coated ITO films were subjected to square wave potential with 5 seconds time intervals in 0.1 molar TBAPF<sub>6</sub>/ACN and by utilizing UV Vis-NIR spectrophotometer

and optical contrast of polymers were determined. Additionally, switching times of conjugated polymers were calculated by utilizing chronoamperometry.

#### **2.4.6. Thermal Studies**

Two different techniques were utilized to analyze thermal properties of conjugated polymers namely thermal gravimetric analysis (TGA) and differential scanning calorimetry (DSC). TGA measures changes in weight in relation to changes in temperature to detect decomposition temperatures of the conjugated polymers, whereas DSC measures the difference heat flow rate between conjugated sample and a reference as a function of time and temperature to obtain melting point ( $T_m$ ) and glass transition temperature ( $T_g$ ) of the polymers. In this thesis, Perkin Elmer Pyris 1 Thermal Gravimetry Analysis and Perkin Elmer Differential Scanning Calorimetry were utilized for the thermal analysis of synthesized three polymers.

#### **2.4.7. Fabrication and Photovoltaic Studies of Organic Photovoltaics**

In order to evaluate photovoltaic performances of synthesized polymers, traditional ITO/PEDOT:PSS/Polymer:PC<sub>71</sub>BM/LiF/Al device architecture was constructed. Typical BHJ devices were fabricated as follows; ITO etching-cleaning, PEDOT:PSS coating, processing active layer and metal evaporation respectively. ITO glass substrates were etched by zinc powder and hydrochloric acid and then ultrasonically cleaned sequentially with toluene, detergent (Hellmanex), distilled water and isopropyl alcohol. Each solvent was sonicated for 15 minutes in ultrasonic bath. Prior to oxygen plasma treatment all substrates were dried with N<sub>2</sub> gun. Plasma treatment was carried out by utilizing Harrick Plasma Cleaner for 5 minutes to the substrates. Indeed, this step was necessary for the enhancement of WF of ITO via removing organic impurities and for reduction the surface tension of ITO. Then, the glass substrates were covered by PEDOT:PSS via spin coating technique at different rpm values. Thereafter, to remove water residues on the coated substrates, annealing was done at 140 °C for 15 min on the hot plate. Active layer processing was performed by

blending Polymer:PC<sub>71</sub>BM (purchased from Solenne) with different weight ratios and different blend concentrations. Also, active layer was treated with different solvent additive concentrations. Then, after preparation of photoactive layer, they were spin coated onto hole transport layer inside the N<sub>2</sub> filled glove box. Lastly, the device was completed by thermal evaporation of LiF and Al metal in a vacuum evaporation chamber. Current density (J)-voltage (V) characteristics of polymers under dark and illumination (AM 1.5G, 100 mW/cm<sup>2</sup>) were investigated by using Keithley 2400 sourcemeter inside the nitrogen filled glove box.

## CHAPTER 3

### RESULTS AND DISCUSSIONS

#### 3.1. Optical Studies

Normalized UV-Vis absorption spectra of synthesized polymers in dilute  $\text{CHCl}_3$  solutions and thin-films spin-coated from  $\text{CHCl}_3$  are shown in Figure 3.1. These polymers which were designed based on the intrachain D-A polymer theme, were expected to demonstrate the strong and broad absorption in the visible and near IR region. Hence, all compounds exhibited two distinct absorption bands in both the long wavelength zone and short wavelength zone. The absorption in the shorter wavelength or high energy band is attributed as the localized  $\pi$ - $\pi^*$  transition, whereas absorption at longer wavelength in other words lower energy band is assigned as the ICT among donor and acceptor moieties. Absorption at shorter wavelengths can be assigned as shoulders and the thin film peaks at 450 nm and 445 nm are the shoulders of P1 and P3 respectively. On the other hand, the green polymer namely P2 demonstrated two peaks both in the red region at 460 nm and blue region at 660 nm in the thin film absorption spectrum of P2. Maximum wavelength ( $\lambda_{\text{max}}$ ) values of all polymers both in solution and thin film are summarized in Table 3.1. In the thin film of corresponding polymers, absorption becomes broader and both of them are red shifted with following three peaks 600, 715 and 610 nm respectively. Particularly, red shifts and obvious broadening peaks in the thin film absorption spectra of the polymers signaling that polymer chains are highly aggregated in their solid state. The P2 possesses larger red shift compared to P1 and P3, the reason of this situation can be explained from the phenanthrene unit in the P2, which induces fused planarity by cyclization of two phenyl rings on the quinoxaline structure with an enhancement of intermolecular electronic interactions in the solid state. Moreover, it is expected that P2 should

demonstrate effective conjugation length with a narrower band gap owing to highest planarity.

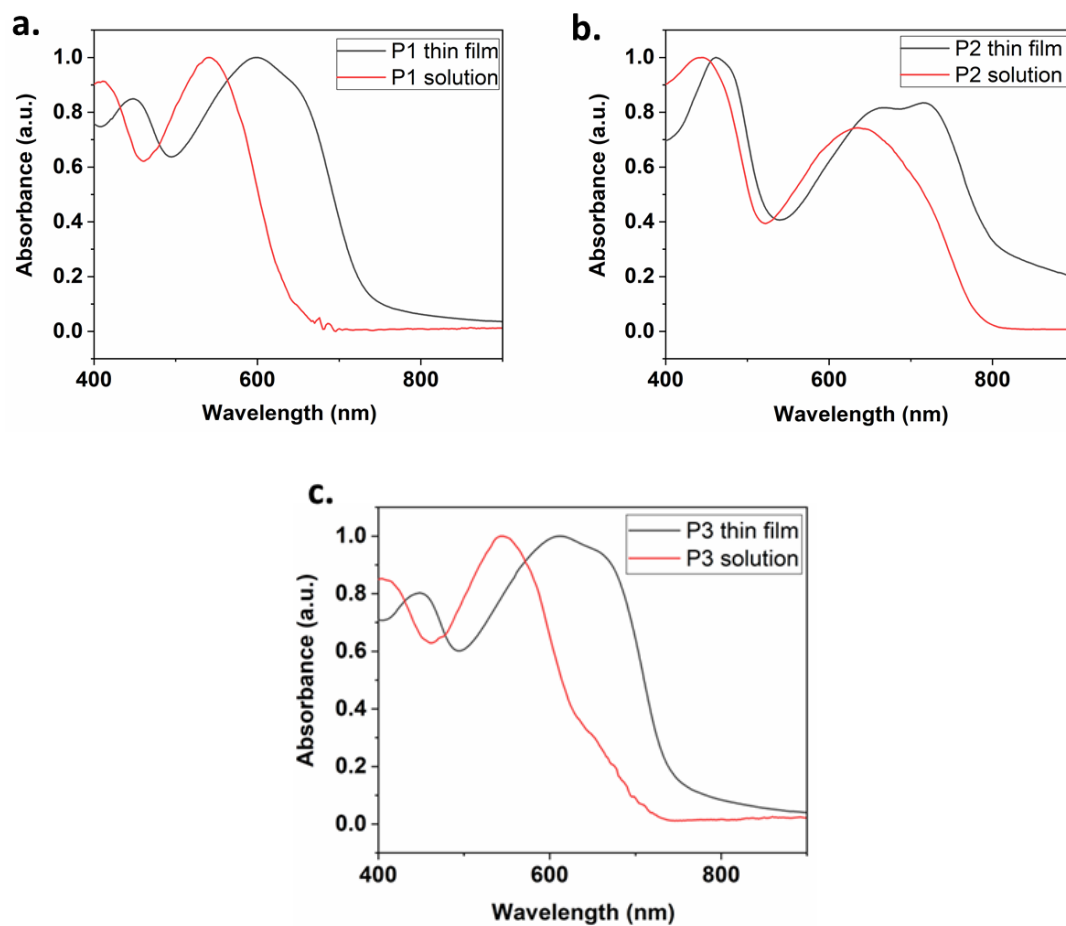


**Figure 3.1.** Normalized UV-Vis absorption spectra of synthesized polymers a) P1, b) P2, c) P3 in  $\text{CHCl}_3$  solutions (in red) and thin-films spin-coated from  $\text{CHCl}_3$  (in black)

**Table 3.1.** Maximum wavelength ( $\lambda_{\max}$ ) values of all polymers both in solution and thin film

Polymer	Solution $\lambda_{\max}$ (nm)	Thin film $\lambda_{\max}$ (nm)
<b>P1</b>	542	600
<b>P2</b>	637	715
<b>P3</b>	542	610

### 3.2. Electrochemical Studies

As mentioned previously in the section 2.4.1., cyclic voltammetry system that consisted of three electrode system as following; Ag wire is the reference electrode (RE), platinum wire is the counter electrode (CE) and Indium Tin Oxide (ITO) coated glass is the working electrode (WE) conducted for the electrochemical characterization of the synthesized three polymers. These polymers namely P1, P2 and P3 were dissolved in chloroform prior to spray coating onto ITO glasses. Then, polymer coated working electrodes were immersed in ACN solvent with 0.1 M electrolyte TBAPF<sub>6</sub>. CV measurements were carried out in order to get information about redox behaviors of the P1, P2 and P3 at a constant 100 mV/s scan rate. Onset oxidation, onset reduction and doping-dedoping potentials of studied polymers were investigated from the cyclic voltammograms which were depicted in below Figure 3.2.

Onset oxidation and onset reduction potentials were investigated from the cyclic voltammograms. Briefly, the  $E_{\text{ox}}^{\text{onset}}$  of P1, P2 and P3 were detected as 0.60, 0.57, 0.63 while the  $E_{\text{red}}^{\text{onset}}$  of polymers were found as -1.20, -1.13 and -1.10 respectively.

According to voltammograms, all three polymers have p-doping and n-doping properties in other words both polymers possess ambipolar character.

Later, HOMO and LUMO energy levels as well as the electronic band gap of the polymers in the thin films were calculated from the corresponding onset oxidation and onset reduction potentials recorded from the CV.

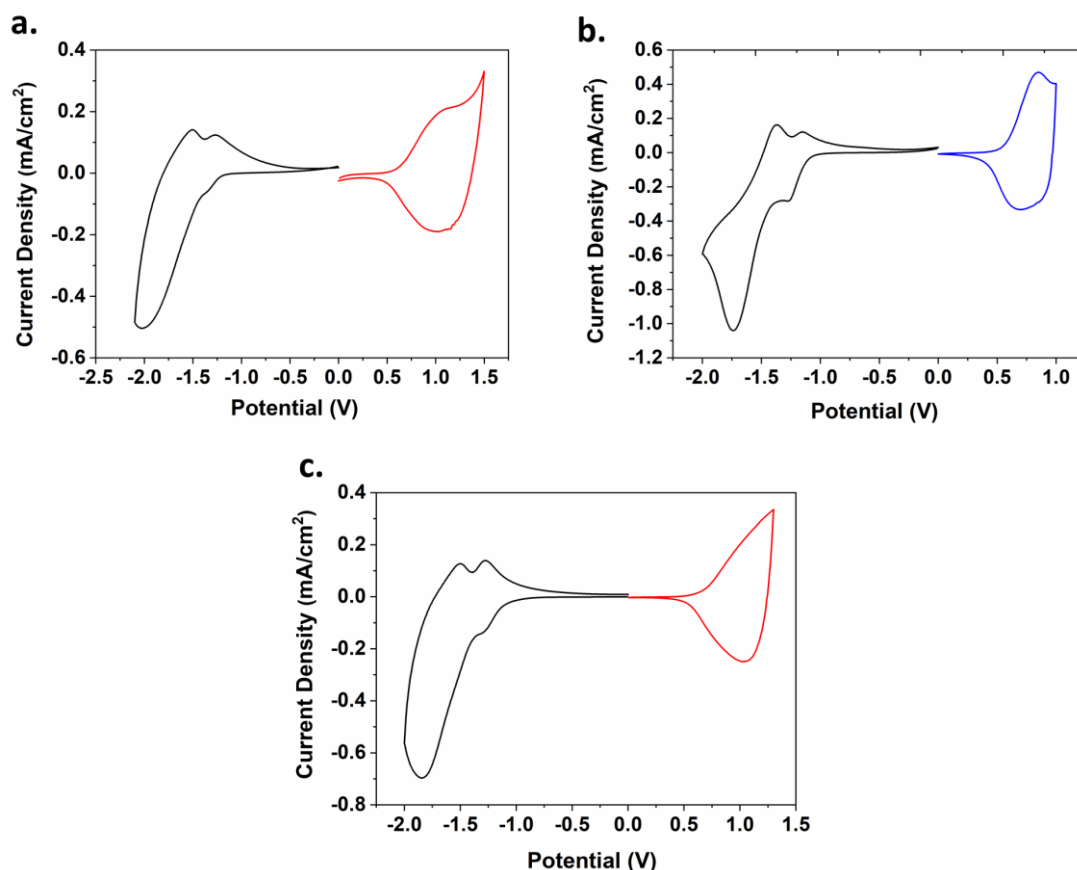


**Figure 3.2.** Cyclic voltammograms of polymers a) P1 b) P2 c) P3 in the thin films at a scan rate 100 mV/s and in 0.1 M supporting electrolyte/ solvent couple (TBAPF<sub>6</sub>/ACN)

The curves obtained from CV were internally calibrated by utilizing standard reference of ferrocene/ferrocenium redox couple (Fc/Fc<sup>+</sup>) with 0.05 eV half wave reduction potential relative to the reference electrode (Ag wire) potential. The absolute energy level of ferrocene was assumed as 4.80 eV below the vacuum level and after calibration of reference electrode, it was assigned as 4.75 eV. Furthermore, following

equations were used to calculate HOMO-LUMO energy values of polymers where the  $E_{1/2, \text{Fc,Fc}^+}$  was the half wave reduction potential of ferrocene/ferrocenium redox couple, the  $E_{\text{ox}}^{\text{onset}}$  was the onset oxidation potential and  $E_{\text{red}}^{\text{onset}}$  was the onset reduction potential and also the energy difference between calculated HOMO and LUMO gave electronic band gap ( $E_{\text{g}}^{\text{el}}$ ) of all polymers recorded from the cyclic voltammograms relative to the silver reference electrode.

$$\text{HOMO} = - (4.80 - E_{1/2, \text{Fc,Fc}^+} + E_{\text{ox}}^{\text{onset}}) = - (4.75 + E_{\text{ox}}^{\text{onset}}) \text{ eV}$$

$$\text{LUMO} = - (4.75 + E_{\text{red}}^{\text{onset}}) \text{ eV}$$

$$E_{\text{g}}^{\text{el}} = \text{HOMO-LUMO eV}$$

By using above formulas, HOMO of P1, P2 and P3 were evaluated as -5.35 eV, -5.32 eV, -5.38 eV whereas LUMO energy levels were found as -3.55 eV, -3.62 eV, -3.65 eV, correspondingly. The electronic band gaps of P1 and P3 were estimated to be 1.80 eV and 1.73 eV respectively, while the lowest electronic band gap was found as 1.70 eV which belongs to the P2.

P3 had low lying HOMO and LUMO energy level than those of P1 and P2 owing to introduction of strong electron withdrawing fluorine atom on the polymer backbone. Substitution of F atom attained deeper levels for HOMO/LUMO, at the same time lower the electronic band gap by diminishing electron density of the polymer backbone and by minimizing unexpected steric interactions. However, the narrower electronic band gap was observed for the P2 which can be explained by the planar and rigid structure of phenanthrene unit with fused BDT unit and easy generation of quinoid structure. Moreover, low resonance stabilization and enhanced planarity eases electron delocalization on conjugation main chain via lowering band gap. In comparison to nonfluorinated P1, fluorinated P3 exhibited lower band gap which could be the results from the F atom since it causes planarization of the conjugated chain through intramolecular and intermolecular interactions.

Representative electrochemical results of polymers as well as the energy level parameters of them which derived from the cyclic voltammograms were given in Table 3.2.

**Table 3.2.** Representative electrochemical results of polymers derived from the cyclic voltammograms

	$E_{p,doping}$ (V)	$E_{p,dedoping}$ (V)	$E_{n,doping}$ (V)	$E_{n,dedoping}$ (V)	$E_{ox}^{onset}$ (V)	$E_{red}^{onset}$ (V)	HOMO (eV)	LUMO (eV)	$E_g^{el}$ (eV)
<b>P1</b>	1.10	0.99	-1.34/-2.00	-1.25/-1.50	0.60	-1.20	-5.35	-3.55	1.80
<b>P2</b>	0.85	0.69	-1.26/-1.74	-1.15/-1.37	0.57	-1.13	-5.32	-3.62	1.70
<b>P3</b>	1.18	1.03	-1.29/-1.85	-1.28/-1.50	0.63	-1.10	-5.38	-3.65	1.73

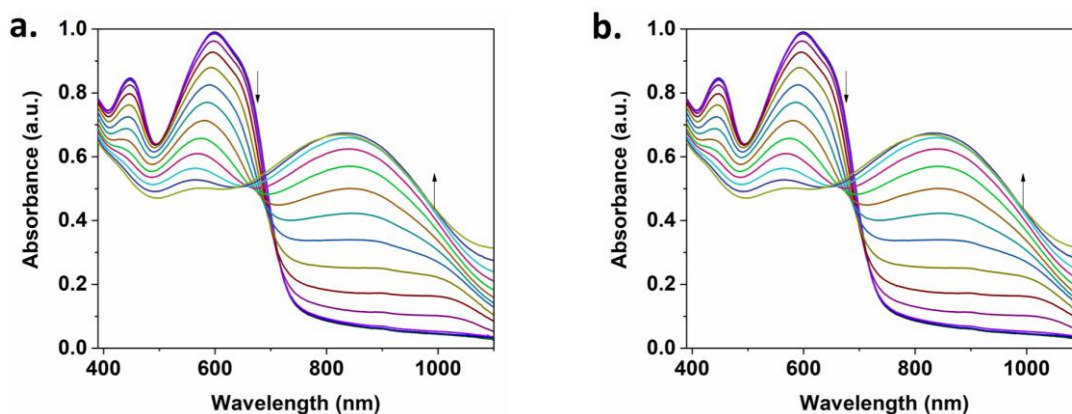
### 3.3. Spectroelectrochemical Studies

The synthesized polymers were spectrochemically characterized using three electrode system in supporting electrolyte/solvent couple while changing the applied potential in the UV-Vis-NIR regions as mentioned before in the section 2.4. Experimental procedure initiated with the solvation process of polymers in  $CHCl_3$ , after that they were deposited onto the ITO coated glass slides at room T via spin coating. Then, spectroelectrochemical results gave the optical absorption (a.u.) as a function of wavelength (nm). As shown in Figure 3.3., responses were recorded in the absorption spectra upon oxidative doping potentials, all polymers demonstrated two distinct absorption peaks around 400-700 nm and they possess absorption in the NIR region. With the applied stepwise oxidation, as it was expected, the intensity of detected absorption bands of polymers began to reduce and the absorption in the NIR regions initiated to raise owing to formation of polarons. This depletion and increment of the intensity of peaks can be explained with the concentration changes. As the oxidation

process continuously applied to polymer, neutral polymer concentration starts to diminish, whereas polaron concentration increases due to formation of charge carriers.

Since the absorption of light by the donor material causes excitation of electrons to the higher energy level while leaving holes in the HOMO level, the energy is created owing to excitation process and the wavelength of this energy is called optical band gap. By taking tangent line of the  $\pi$ - $\pi^*$  interband transition where the maximum absorption process was started for the polymers in other words from the onset point, optical band gaps ( $E_g^{op}$ ) were found as 1.67 eV, 1.45 eV and 1.64 eV for P1, P2 and lastly P3 respectively. The Table 3.3 represents the values of  $E_g^{op}$  (eV) and  $\lambda_{max}^{onset}$  (nm) for each polymer.

It is worth noting that the electronic gap mostly is larger than the optical gap. The reason behind this difference can be explained by the free electrons in cyclic voltammetry measurements. As compared to CV, in the optical measurements, excitation process does not alter the number of electrons and thus it remains constant at the end of the excitation. Therefore, both synthesized polymers namely P1, P2 and P3 exhibited larger  $E_g^{el}$  than  $E_g^{op}$  in this study. When compared to  $E_g^{op}$  values of polymers with each other P2 had the lowest optical band gap. This phenomenon like in the case of electronic band gap, can be clarified by the degree of interchain  $\pi$ - $\pi$  stacking or/and planar rigid polymer chain of P2.



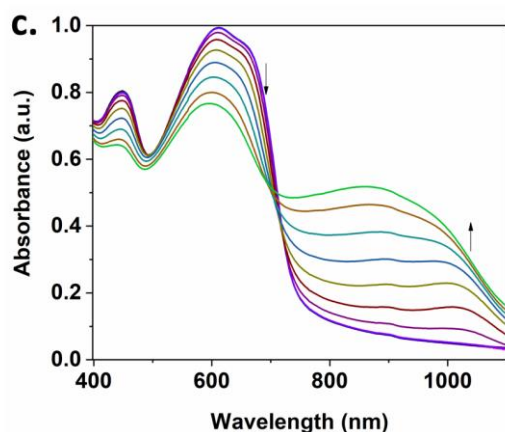


**Figure 3.3.** The change in the electronic absorption spectra of corresponding polymers a) P1, b) P2 and c) P3 upon oxidative doping potentials in supporting electrolyte/solvent couple (0.1 M TBAPF<sub>6</sub>/ACN)

**Table 3.3.** The recorded values of  $E_{g}^{op}$  and  $\lambda_{max}^{onset}$  for each polymer.

Polymer	$\lambda_{max}^{onset}(nm)$	$E_{g}^{op}$ (eV)
<b>P1</b>	745	1.67
<b>P2</b>	858	1.45
<b>P3</b>	760	1.64

Colorimetric measurements were carried out in order to determine brightness (L), saturation (b) and hue (a) of the synthesized polymers films by International Commission on Illumination (CIE) system. Both polymers exhibited different colors between their neutral, oxidized and reduced states. P1 and P3 showed dark purple colors in their neutral states and P2 demonstrated green color in its neutral state. All polymers showed light grey in oxidized state and dark grey in reduced state. In Figure 3.4. colors and the L, a and b values of corresponding polymers were represented.

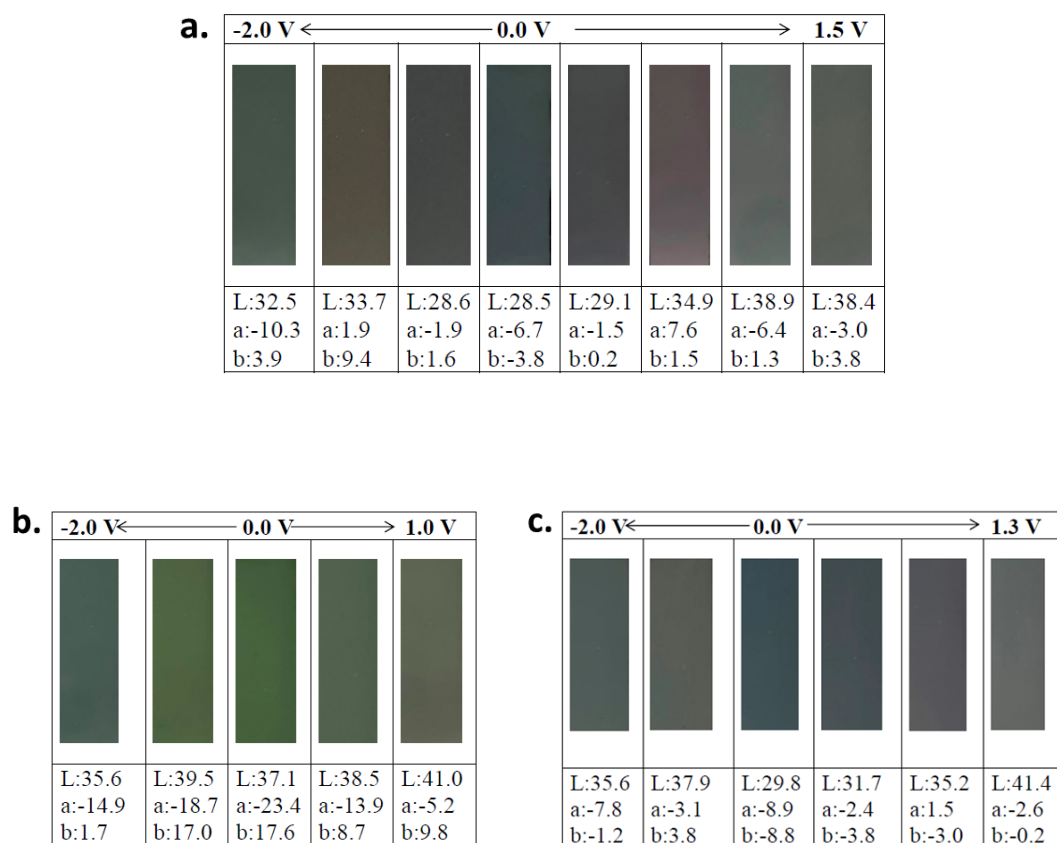


**Figure 3.4.** The colors and L, a, b values of corresponding polymers a) P1, b) P2 and c) P3

### 3.4. Kinetic Studies

As mentioned previously by utilizing UV Vis-NIR spectrophotometer, P1, P2 and P3 coated ITO thin films were subjected to square wave potential with 5 seconds time intervals in 0.1 molar TBAPF<sub>6</sub>/ACN and both optical contrasts and switching times of polymers were determined. Notably, optical contrast shows the difference between percent transmittance (T%) of two extreme states of polymers which are reduced and oxidized states at a 95% contrast since 95% of full contrast represents the sensitivity of human eye. Transmittance changes at dominant wavelengths were depicted in Figure 3.5. and the values of optical contrast ( $\Delta T\%$ ) and switching times (s) at these

wavelengths for P1, P2 and P3 were shown in the Table 3.4. From the absorption versus time spectra of kinetic studies, it can be deduced that optical contrasts of three polymers in the visible region were lower than the optical contrasts in the NIR region. For the longer wavelength absorption band of P1, P2 and P3, the higher optical contrasts were recorded as 34%, 28% and 47% with smaller 1.0 s, 1.0 s and 0.9 s switching times respectively. On the other hand, the optical contrast at shorter wavelength were found for P1; 13%, 23% for P1; 22%, 18% and for P3; 18%, 25% with longer switching times.

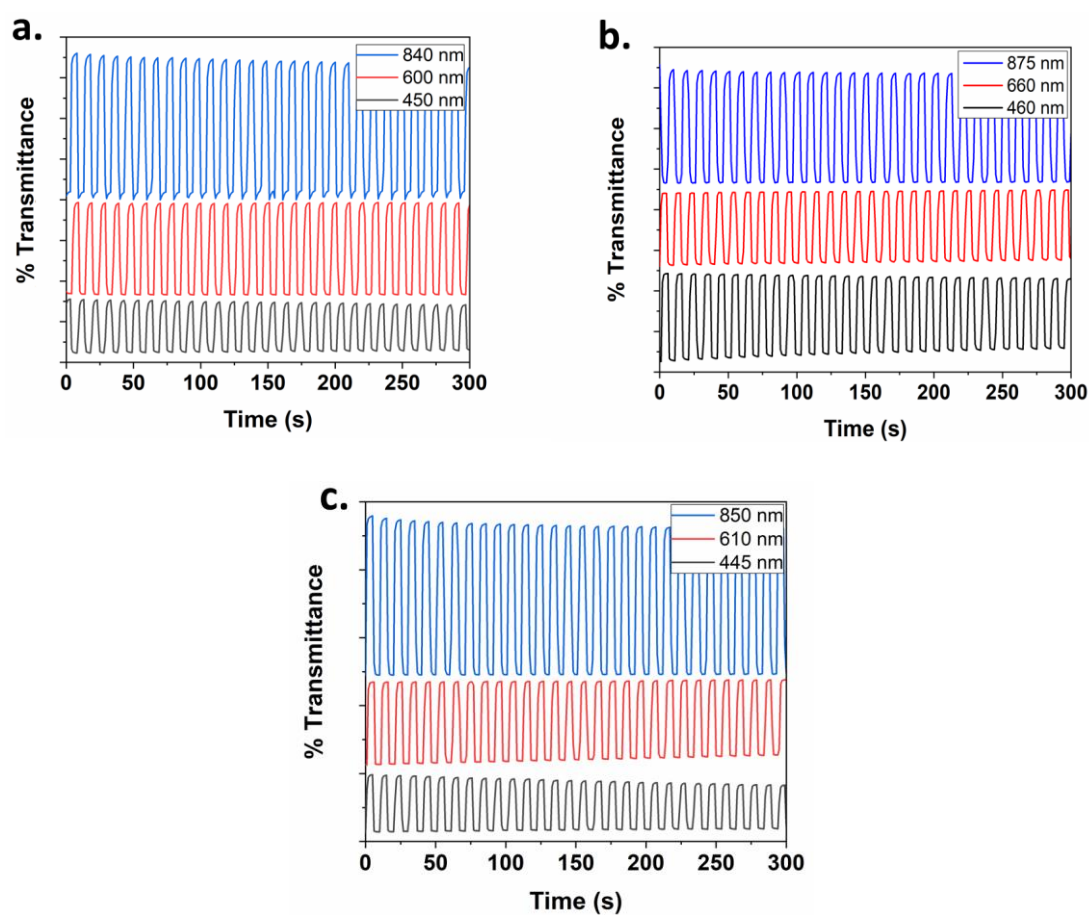


**Figure 3.5.** Transmittance changes at dominant wavelengths for a) P1 b) P2 c) P3

**Table 3.4.** The values of optical contrasts ( $\Delta T\%$ ) and switching times (s) at dominant wavelengths for P1, P2 and P3

Polymer	Wavelength (nm)	Optical contrast $\Delta T\%$	Switching time (s)
<b>P1</b>	450	13	1.8
	600	23	1.6
	840	34	1.0
<b>P2</b>	460	22	1.9
	660	18	1.8
	875	28	1.0
<b>P3</b>	445	18	1.6
	610	25	1.0
	845	47	0.9

### 3.5. Thermal Studies

Thermal properties of synthesized polymers were investigated both by DSC and TGA with heating rate of 10 °C/min under nitrogen atmosphere. For TGA, temperature range was between 25 °C-600 °C, while for DSC it was between 25 °C-300 °C. The report obtained from the TGA studies proved that all polymers possess good thermal stability up to 400°C. After this temperature, weight losses were observed for P1, P2 and P3 as following; 54%, 57% and 53% respectively and the decomposition temperatures were detected as 450 °C for P1 and P3 and 443 °C for P2. The DSC analysis provided that all polymers significantly stable in the range of 25 °C-300 °C and did not demonstrate phase transitions upon applying heating and cooling processes. In the appendices part, thermal studies reports resulted from DSC and TGA were illustrated.

### 3.6. Photovoltaic Studies

BHJ photovoltaic solar devices based on three polymers with an architecture of ITO /PEDOT:PSS /Polymer:PC<sub>71</sub>BM/LiF/Al were fabricated and photovoltaic parameters of these devices were evaluated under illumination (AM 1.5G, 100 mW/cm<sup>2</sup>). Detailed information on the device fabrication and characterization were given in the experimental part. Herein, as mentioned before BHJ active layer consisted of blend of polymer donor and fullerene acceptor. PC<sub>71</sub>BM was chosen as an acceptor owing to broader and stronger absorption in the visible zone as compared to other fullerenes such as PC<sub>61</sub>BM. In order to get most efficient solar cells, various optimizations were done such as blend ratio of polymer and PC<sub>71</sub>BM (w:w) and blend concentration optimization. In addition to BHJ blend ratio and blend concentration optimization, thickness optimizations were also carried out by altering spin coating rate. Notably, processing solvent additives had no positive effect on the device photovoltaic performance in this study. Figure 3.6. illustrates the energy level diagrams of all polymers using data derived from cyclic voltammograms and the energy levels of other materials used in the solar cell fabrication process. According to the HOMO-LUMO energy levels also band gap of the polymers obtained from CV, it is clearly understood that these polymers compatible with PC<sub>71</sub>BM in terms of energy levels and they can be utilized in the solar cell applications.

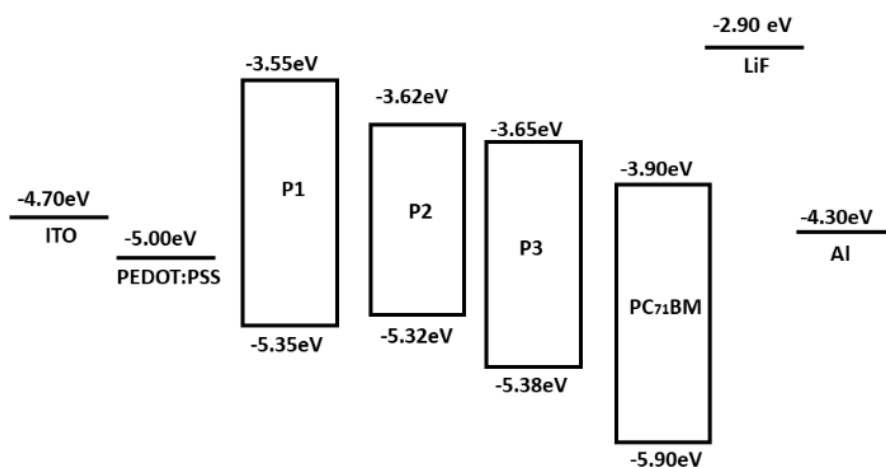


**Figure 3.6.** Energy level diagrams of all polymers using data derived from cyclic voltammograms with device architecture

For clear comparison of device performance of synthesized three polymers namely P1, P2 and P3, their photovoltaic data were shown in the Tables 3.5., 3.6. and 3.7. respectively.

Among all three polymers, fluorinated P3 with following blend ratio P3:PC<sub>71</sub>BM (1:4, w/w) showed the highest performance with a PCE of 2.45%, a J<sub>SC</sub> of 7.59 mA/cm<sup>2</sup>, a V<sub>OC</sub> 0.77 V and a FF of 41%. Whereas, P1:PC<sub>71</sub>BM (1:3, w/w) exhibited the best PCE as 2.36% and the P2 exhibited the best PCE as 2.07%.

**Table 3.5.** Device parameters of P1 containing OPV cells

P1:PC <sub>71</sub> BM (w:w)	J <sub>SC</sub> (mA/cm <sup>2</sup> )	V <sub>OC</sub> (V)	J <sub>MAX</sub> (mA/cm <sup>2</sup> )	V <sub>MAX</sub> (V)	FF%	PCE%	RPM
1:2 (2%)	5.76	0.77	3.89	0.49	43	1.92	500
1:3 (2%)	7.32	0.77	4.96	0.44	39	2.21	500
1:4 (2%)	7.10	0.77	4.19	0.47	39	1.97	500
1:3 (2%)	3.07	0.58	1.57	0.35	30	0.55	500
1:3 (3%)	8.19	0.77	4.96	0.44	35	2.21	500
<b>1:3 (2%)</b>	<b>7.29</b>	<b>0.79</b>	<b>4.52</b>	<b>0.52</b>	<b>41</b>	<b>2.36</b>	<b>350</b>
1:3 (2%)	6.94	0.79	3.94	0.48	35	1.92	750

**Table 3.6.** Device parameters of P2 containing OPV cells

P2:PC <sub>71</sub> BM (w:w)	J <sub>SC</sub> (mA/cm <sup>2</sup> )	V <sub>OC</sub> (V)	J <sub>MAX</sub> (mA/cm <sup>2</sup> )	V <sub>MAX</sub> (V)	FF%	PCE%	RPM
<b>1:2 (2%)</b>	<b>5.27</b>	<b>0.71</b>	<b>3.96</b>	<b>0.52</b>	<b>55</b>	<b>2.07</b>	<b>500</b>
1:3 (2%)	5.30	0.70	3.62	0.38	37	1.38	500

**Table 3.7.** Device parameters of P3 containing OPV cells

P3:PC <sub>71</sub> BM (w:w)	J <sub>SC</sub> (mA/cm <sup>2</sup> )	V <sub>OC</sub> (V)	J <sub>MAX</sub> (mA/cm <sup>2</sup> )	V <sub>MAX</sub> (V)	FF%	PCE%	Rpm
1:1 (2%)	2.50	0.75	1.73	0.53	49	0.92	500
1:2 (2%)	3.95	0.75	2.44	0.57	46	1.38	500
1:3 (2%)	3.85	0.75	2.35	0.61	49	1.43	500
1:4 (2%)	5.14	0.76	3.22	0.51	42	1.65	500
1:4 (2.5%)	7.13	0.74	3.38	0.54	34	1.83	500
1:4 (3%)	7.63	0.75	4.29	0.47	35	2.02	500
<b>1:4 (3%)</b>	<b>7.59</b>	<b>0.77</b>	<b>4.36</b>	<b>0.56</b>	<b>41</b>	<b>2.45</b>	<b>350</b>
1:4 (3%)	5.90	0.74	3.51	0.42	33	1.48	750

For P1 containing devices, different optimization processes were performed as can be deduced in Table 3.7. Moreover, Figure 3.7. represents the J-V curves of P1 based solar cells with different blend ratios and different spin coating rates. When the blend ratio changed from 1:2 to 1:3 short circuit current values were enhanced. The best

performing P3 based device was detected as 1:3 blend ratio with 2% blend concentration (20 mg/mL Polymer: PC<sub>71</sub>BM solution) in o-DCB at 350 rpm. Generally, the increase in the polymer concentration inside the active layer and decrease in the spin coating rate causes enhancement of light absorption ability of and results thicker active layer respectively and these optimizations provides better photovoltaic performances. However, compare to 3% blend concentration of P1:PC<sub>71</sub>BM (1:3) at 500 rpm, 2% blend concentration of P1:PC<sub>71</sub>BM (1:3) at 350 rpm exhibited higher PCE. This unexpected situation could be clarified from a rise in the FF values from 35% to 41 %.

For P2 containing solar devices, blend ratio was changed from 1:2 to 1:3 and this optimization reduced the efficiency of devices from 2.07% to 1.38%. In general, decreasing concentration of polymers via increasing amount of PCBM can cause reduction of J<sub>SC</sub> value but in this case J<sub>SC</sub> value did not change significantly. However, the FF of devices were reduced from 55% to 37% in chlorobenzene solution. This huge decrease of FF can be explained from the active layer morphology and higher PCE device were achieved owing to good morphology in active layer with an enhancement of FF for the P2 based devices with 1:3 blend ratio and 2% blend concentration. Figure 3.8. represents J-V curve of PSCs based on P2:PC<sub>71</sub>BM with different D/A ratios.

P3:PC<sub>71</sub>BM ratio optimizations proved that, ratio of 1:4 was found to be optimum performance for P3:PC<sub>71</sub>BM containing solar cells as seen in Figure 3.9. Although decreased polymer concentration should possess lower J<sub>SC</sub> since the J<sub>SC</sub> is primarily determined by absorption ability of the BHJ blend layer, P3:PC<sub>71</sub>BM with lowest polymer concentration (1:4 ratio) was achieved highest J<sub>SC</sub> values as compared to 1:2 and 1:3 ratios. Blend concentration optimizations proved that 3% weight/volume (w/v) blend concentration in other words 30 mg/mL polymer: PC<sub>71</sub>BM solution in o-DCB yielded more efficient devices than 2% weight/volume (w/v) blend concentration in o-DCB. The reason behind this enhancement of the PCE could be explained by the increase in current density values up to 7.59 mA/cm<sup>2</sup> for the P3

based solar device. As the current density increases harvesting incoming light becomes easier at the same time efficiency increases. Additionally, thickness optimizations were studied with three spin coating rates for the cells with 1:4 blend ratio and 3% blend concentration. In the literature it was proven that the thicker active layer possesses higher performance however, in this study for P3 based cells optimum conditions were selected at 350 rpm. The reason of this situation can be explained from the current densities. Since the current density decreased from 7.59 mA/cm<sup>2</sup> to 5.90 mA/cm<sup>2</sup> from the spin coating rate of 350 rpm to 750 rpm, the device performances were affected from these changes in the J<sub>SC</sub> values. Figure 3.9. represents J-V curve of PSCs based on P3:PC<sub>71</sub>BM with different D/A ratios.

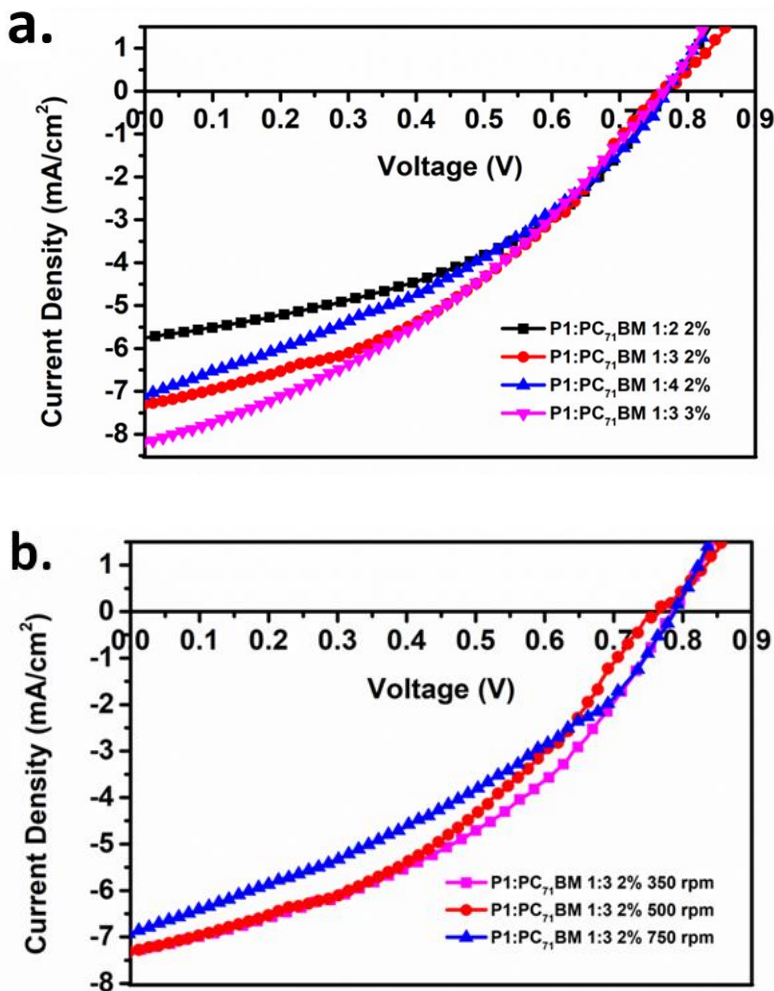


**Figure 3.7.** J-V curve of PSCs based on P1:PC<sub>71</sub>BM a) with different D/A ratios b) with different spin coating rates

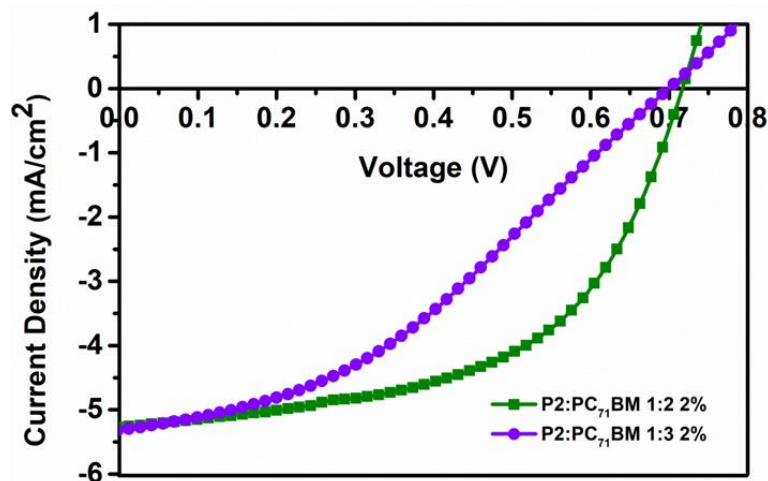


**Figure 3.8.** J-V curve of PSCs based on P2:PC<sub>71</sub>BM with different D/A ratios

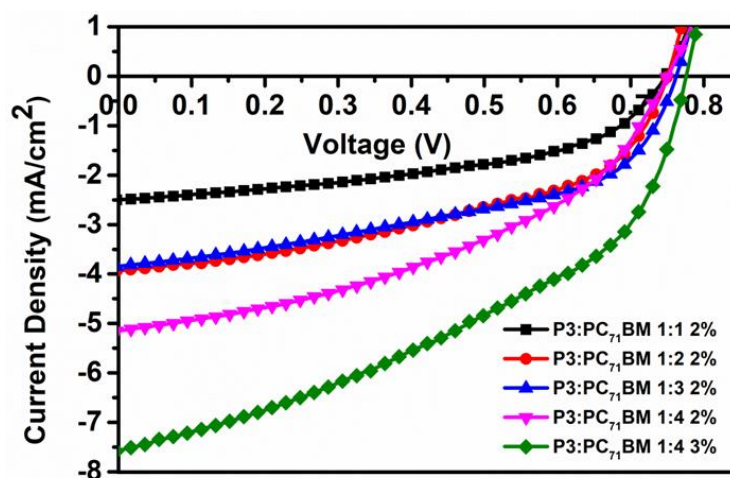


**Figure 3.9.** J-V curve of PSCs based on P3:PC<sub>71</sub>BM with different D/A ratios

Although the narrower band gap and more red shifted absorption were obtained from the P2, P1 and P3 demonstrated better conversion efficiencies than P2. The reason of this phenomenon can be explained based on the molecular weights and morphology of polymers. Thus, lower molecular weight of P2 results in shorter polymer chain

length for the intermolecular charge hopping process and aggregation in the solid state of P2 could be the reason of morphological problems by yielding lower PCEs. Introduction of fluorine onto quinoxaline part has a synergistic effect on enhancing  $J_{SC}$  and  $V_{OC}$  as compared to fused structure polymer (P2). Compared to the nonfluorinated P1 based devices, fluorinated P3 based devices slightly higher  $J_{SC}$  ( $7.59 \text{ mA/cm}^2$ ) and similar FF (41%) values. The higher  $J_{SC}$  value could be the reason of higher efficiency and better morphology for P3. Also, F atom might lead to enhancement of planarization in the thin film by intermolecular interactions and might result in the improvement in the performance of PSCs.

In order to confirm the accuracy of the characterized photovoltaic cells the external quantum efficiencies of the devices were evaluated. For the EQE analysis, devices were constructed under same conditions as those utilized for the photovoltaic measurement to achieve representative J-V curves with AM 1.5 G spectrum. The corresponding EQE curves of resulted polymers were depicted in Figure 3.10. These curves provided EQE wavelength dependencies and also by integrating max EQE values  $J_{SC}$  values of the polymers can be detected easily. Clearly all devices were possessed photo response at the range of 400-700 nm, which was in agreement with red shifted spectrum of polymers that was obtained from the optical studies of the thin films. Also, maximum EQE values were detected as 62%, 35% and 48% for P1, P2 and P3, correspondingly. After the integration of EQE values,  $J_{SC}$  of the devices were deduced as  $6.95 \text{ mA/cm}^2$  for P1,  $6.95 \text{ mA/cm}^2$  for P2 and  $7.01 \text{ mA/cm}^2$  for P3 and these current densities are reasonably close to the  $J_{SC}$  of cells obtained from the J-V curves.

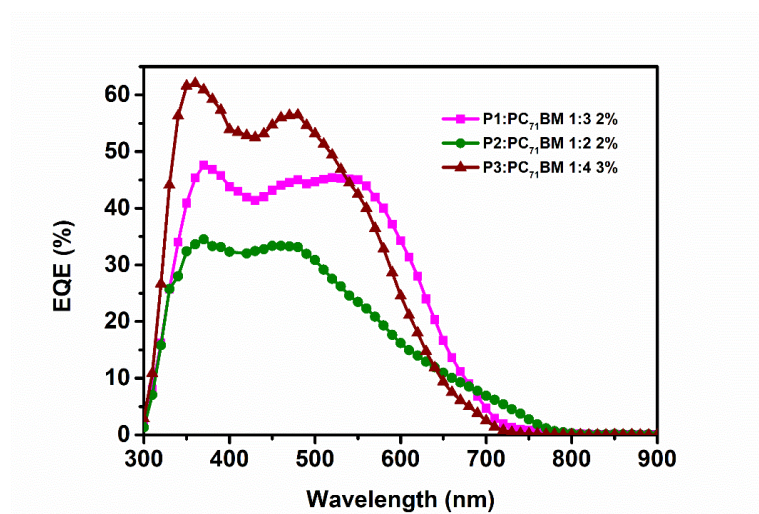


**Figure 3.10.** EQE curves of P1, P2 and P3 based best performing solar cells

### 3.7. Morphology

As mentioned previously FF is the indicator of photovoltaic performance of devices and essentially based on the morphology of photoactive layer. The surface morphologies of photoactive layers which contains polymer and PC<sub>71</sub>BM were investigated with Atomic Force Microscopy (AFM) to gain deeper information about devices. The resulted AFM images of the best performing films of synthesized three polymers are provided in Figure 3.11.

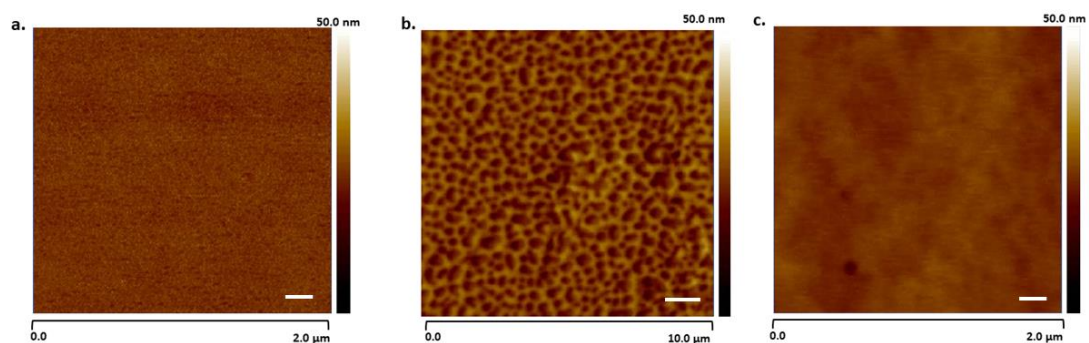


**Figure 3.11.** The surface morphologies of photoactive layers obtained from AFM measurements; a) P1:PC<sub>71</sub>BM (1:3, w:w), b) P2:PC<sub>71</sub>BM (1:2, w:w) c) P3 : PC<sub>71</sub>BM (1:4, w:w). Scale bar represents 200 nm

The AFM images of photoactive films indicated that there was no large aggregation for P1: PC<sub>71</sub>BM and P3:PC<sub>71</sub>BM films and these good film morphologies could be the result of high J<sub>SC</sub> of these polymers. As can be seen from the Figure 3.11., P2:PC<sub>71</sub>BM based device which shown more pronounced red-shifted absorption spectra as compared to P1 and P3 based devices, the lowest short circuit density values and lowest device performances of P2 containing devices were presumably caused by the aggregation in the solid state of photoactive layer. The surface roughnesses measured from these images were 0.28 nm, 3.29 nm and 1.03 nm and active layer thicknesses were detected as 70 nm, 80 nm and 84 nm for P1, P2 and P3 correspondingly. The resulted thicknesses of thin films were both lower than the determined optimum active layer thickness (100 nm) for D-A containing polymer based BHJ solar cells in the literature.

## CHAPTER 4

### CONCLUSIONS

Three new conjugated polymers with electron accepting segments of different quinoxalines and electron donating segments of BDT were successfully designed and synthesized via Pd (0) catalyzed Stille cross coupling reaction. All synthesized polymers had good solubility in widely used solvents since they contain branch octyl dodecyl side chain on the selenophene ring which was attached to BDT backbone. Additionally, 3-hexylthiophene unit acted as a  $\pi$  bridge and seems to promote more enhanced conjugation length for electron delocalization along the polymer axis. As compared to P1 and P3 which showed dark purple color in their neutral states, phenanthrene containing fused structure P2 exhibited green color in its neutral state in the thin film form. In order to investigate optoelectronic properties of synthesized polymers, their spectroelectrochemical, electrochemical and optical analyses were studied and compared. From the cyclic voltammograms, it was observed that all polymers have ambipolar characters and highest oxidation potential was calculated for P3 owing to introduction of fluorine atom onto the quinoxaline part. Corresponding LUMO levels were determined to be -3.55 eV, -3.62 eV, -3.65 eV while the HOMO levels were estimated as -5.35 eV, -5.32 eV, -5.38 eV for P1, P2 and P3, respectively. Benefiting from the strong electronegativity of fluorine atom, the P3 has deeper HOMO-LUMO levels and it possess little enhancement on the  $J_{sc}$  value on the photovoltaic measurements in comparison with P1 and P2. With respect to spectroelectrochemical results in the thin film, both P1, P2 and P3 had broad absorption spectra which were located absorption edges at 745, 858 and 760 nm corresponding to optical band gaps of 1.67, 1.45 and 1.64 eV respectively. For further characterization, kinetic features of resulted D-A polymers were tested and it was found that all polymers demonstrated the highest optical contrast for P1 with 34%, for

P2 with 28% and for P3 with 47% with the smallest switching times 1.0 s, 1.0 s and 0.9 s respectively in the NIR region. The maximum optical contrast and broadened absorption of the polymers at the longer wavelengths eventuate the improvement of the usage efficiency of sunlight. More pronounced red shifted absorption spectra of P2 in these three polymers signaling that P2 has the highest aggregation in the solid state and the highest roughness value and these phenomena can be observed also in the AFM image. Photovoltaic characterization of the blends of three conjugated polymers with a fullerene derivative as an acceptor reveal that the best performing device was achieved 2.45% PCE in the P3 bearing device owing to strong electron withdrawing fluorine atom substitution and enhanced morphology as compared to nonfluorinated counterparts. Furthermore, P1 bearing device exhibited the best PCE as 2.36% and the P2 bearing device exhibited the best PCE as 2.07%. Notably, these results indicate that resulting polymers are promising materials for BHJ photovoltaic applications.

## REFERENCES

- [1] K. E. Trenberth and J. T. Fasullo, "Global warming due to increasing absorbed solar radiation," *Geophys. Res. Lett.*, vol. 36, no. 7, pp. 1–5, 2009.
- [2] M. Höök and X. Tang, "Depletion of fossil fuels and anthropogenic climate change-A review," *Energy Policy*, vol. 52, pp. 797–809, 2013.
- [3] M. Grätzel, "Recent advances in sensitized mesoscopic solar cells," *Acc. Chem. Res.*, vol. 42, no. 11, pp. 1788–1798, 2009.
- [4] S. H. Lee, C. K. Lee, S. R. Shin, S. I. Kim, I. So, and S. J. Kim, "Macromol. Rapid Commun. 6/2009," *Macromol. Rapid Commun.*, vol. 30, no. 6, 2009.
- [5] F. Alharbi, J. D. Bass, A. Salhi, A. Alyamani, H. C. Kim, and R. D. Miller, "Abundant non-toxic materials for thin film solar cells: Alternative to conventional materials," *Renew. Energy*, vol. 36, no. 10, pp. 2753–2758, 2011.
- [6] B. A. Gregg and M. C. Hanna, "Comparing organic to inorganic photovoltaic cells: Theory, experiment, and simulation," *J. Appl. Phys.*, vol. 93, no. 6, pp. 3605–3614, 2003.
- [7] H. Shirakawa, E. J. Louis, A. G. MacDiarmid, C. K. Chiang, and A. J. Heeger, "Synthesis of electrically conducting organic polymers: Halogen derivatives of polyacetylene, (CH)<sub>x</sub>," *J. Chem. Soc. Chem. Commun.*, no. 16, pp. 578–580, 1977.
- [8] M. Audenaert, G. Gusman, and R. Deltour, "Electrical conductivity of I<sub>2</sub>-doped polyacetylene," *Phys. Rev. B*, vol. 24, no. 12, pp. 7380–7382, 1981.
- [9] T. Nezakati, A. Seifalian, A. Tan, and A. M. Seifalian, "Conductive Polymers: Opportunities and Challenges in Biomedical Applications," *Chem. Rev.*, vol. 118, no. 14, pp. 6766–6843, 2018.
- [10] J. W. Y. Lam and B. Z. Tang, "Functional polyacetylenes," *Acc. Chem. Res.*, vol. 38, no. 9, pp. 745–754, 2005.
- [11] Springer, "Conducting Polymers,". 1975.
- [12] H. Peng, X. Sun, W. Weng, and X. Fang, *Polymer Materials for Energy and Electronic Applications*. 2016.
- [13] A. Facchetti, " $\pi$ -Conjugated polymers for organic electronics and photovoltaic cell applications," *Chem. Mater.*, vol. 23, no. 3, pp. 733–758, 2011.
- [14] T. H. Le, Y. Kim, and H. Yoon, "Electrical and electrochemical properties of conducting polymers," *Polymers (Basel)*, vol. 9, no. 4, 2017.

- [15] W. Mönch, *Semiconductor Surfaces and Interfaces*, vol. 26, no. 10–12. 1993.
- [16] J. Roncali, “Molecular engineering of the band gap of  $\pi$ -conjugated systems: Facing technological applications,” *Macromol. Rapid Commun.*, vol. 28, no. 17, pp. 1761–1775, 2007.
- [17] I. Capek, *Advances in Polymer Science vol. 145.: Radical polymerisation polyelectrolytes*. 1999.
- [18] M. M. Collinson, *Handbook of Advanced Electronic and Photonic Materials and Devices*. 2001.
- [19] P. Kar, *Doping in Conjugated Polymers*. 2013.
- [20] Y. J. Cheng, S. H. Yang, and C. S. Hsu, “Synthesis of conjugated polymers for organic solar cell applications,” *Chem. Rev.*, vol. 109, no. 11, pp. 5868–5923, 2009.
- [21] J. L. Brédas, “Relationship between band gap and bond length alternation in organic conjugated polymers,” *J. Chem. Phys.*, vol. 82, no. 8, pp. 3808–3811, 1985.
- [22] H. A. Ho, H. Brisset, P. Frère, and J. Roncali, “Electrogenerated small bandgap  $\pi$ -conjugated polymers derived from substituted dithienylethylenes,” *J. Chem. Soc. Chem. Commun.*, no. 22, pp. 2309–2310, 1995.
- [23] H. Brisset, P. Blanchard, B. Illien, and J. Roncali, “Bandgap control through reduction of bond length alternation in bridged poly ( diethienylethylene ),” pp. 569–570, 1997.
- [24] E. E. Havinga, W. ten Hoeve, and H. Wynberg, “Alternate donor-acceptor small-band-gap semiconducting polymers; Polysquaraines and polycroconaines,” *Synth. Met.*, vol. 55, no. 1, pp. 299–306, 1993.
- [25] C. Kitamura, S. Tanaka, and Y. Yamashita, “Design of narrow-bandgap polymers. Syntheses and properties of monomers and polymers containing aromatic-donor and o-quinoid-acceptor units,” *Chem. Mater.*, vol. 8, no. 2, pp. 570–578, 1996.
- [26] H. Lee, D. Lee, D. H. Sin, S. W. Kim, M. S. Jeong, and K. Cho, “Effect of donor–acceptor molecular orientation on charge photogeneration in organic solar cells,” *NPG Asia Mater.*, vol. 10, no. 6, pp. 469–481, 2018.
- [27] A. Armin, P. Wolfers and P. Shaw, “Simultaneous enhancement of charge generation quantum yield and carrier transport in organic solar cells,” *J. Mater. Chem. C*, vol. 3, no. 41, pp. 10799–10812, 2015.
- [28] Y. Sun, “Side chain engineering and conjugation enhancement of benzodithiophene and phenanthrenequinioxaline based conjugated polymers for photovoltaic devices,” *J. Polym. Sci. Part A Polym. Chem.*, vol. 53, no. 16, pp.

1915–1926, 2015.

- [29] J. Zhang, W. Cai and F. Huang, “Synthesis of quinoxaline-based donor-acceptor narrow-band-gap polymers and their cyclized derivatives for bulk-heterojunction polymer solar cell applications,” *Macromolecules*, vol. 44, no. 4, pp. 894–901, 2011.
- [30] J. Hou, M. Park and S. Zhang, “Bandgap and molecular energy level control of conjugated polymer photovoltaic materials based on benzo[1,2-b:4,5-b']dithiophene,” *Macromolecules*, vol. 41, no. 16, pp. 6012–6018, 2008.
- [31] Q. Peng, X. Liu, D. Su, G. Fu, J. Xu, and L. Dai, “Novel benzo[1,2-b:4,5-b']dithiophene-benzothiadiazole derivatives with variable side chains for high-performance solar cells,” *Adv. Mater.*, vol. 23, no. 39, pp. 4554–4558, 2011.
- [32] E. Zhu, G. Ge and J. Shu, “Direct access to 4,8-functionalized benzo[1,2-b:4,5-b']dithiophenes with deep low-lying HOMO levels and high mobilities,” *J. Mater. Chem. A*, vol. 2, no. 33, pp. 13580–13586, 2014.
- [33] H. Hoppe and N. S. Sariciftci, “Organic solar cells: An overview,” *J. Mater. Res.*, vol. 19, no. 7, pp. 1924–1945, 2004.
- [34] B. R. Weinberger, M. Akhtar, and S. C. Gau, “Polyacetylene photovoltaic devices,” *Synth. Met.*, vol. 4, no. 3, pp. 187–197, 1982.
- [35] C. W. Tang, “Two-layer organic photovoltaic cell,” *Appl. Phys. Lett.*, vol. 48, no. 2, pp. 183–185, 1986.
- [36] G. Yu, J. Gao, J. C. Hummelen, F. Wudl, and A. J. Heeger, “Polymer photovoltaic cells: Enhanced efficiencies via a network of internal donor-acceptor heterojunctions,” *Science (80-. )*, vol. 270, no. 5243, p. 1789, 1995.
- [37] K. He, “Work function changes of plasma treated indium tin oxide,” *Org. Electron. physics, Mater. Appl.*, vol. 15, no. 8, pp. 1731–1737, 2014.
- [38] N. S. Sariciftci, L. Smilowitz, A. J. Heeger, and F. Wudl, “Photoinduced electron transfer from a conducting polymer to buckminsterfullerene,” *Science (80-. )*, vol. 258, no. 5087, pp. 1474–1476, 1992.
- [39] S. Li, B. Zhao and Z. He, “Synthesis, characterization and photovoltaic performances of D-A copolymers based on BDT and DBPz: The largely improved performance caused by additional thiophene blocks,” *J. Mater. Chem. A*, vol. 1, no. 14, pp. 4508–4515, 2013.
- [40] Y. W. Su, S. C. Lan, and K. H. Wei, “Organic photovoltaics,” *Mater. Today*, vol. 15, no. 12, pp. 554–562, 2012.
- [41] S. Günes, H. Neugebauer, and N. S. Sariciftci, “Conjugated polymer-based organic solar cells,” *Chem. Rev.*, vol. 107, no. 4, pp. 1324–1338, 2007.

- [42] F. Matsumoto, K. Moriwaki, Y. Takao, and T. Ohno, "Synthesis of thienyl analogues of PCBM and investigation of morphology of mixtures in P3HT," *Beilstein J. Org. Chem.*, vol. 4, pp. 7–12, 2008.
- [43] C. J. Brabec, S. E. Shaheen, C. Winder, N. S. Sariciftci, and P. Denk, "Effect of LiF/metal electrodes on the performance of plastic solar cells," *Appl. Phys. Lett.*, vol. 80, no. 7, pp. 1288–1290, 2002.
- [44] A. J. Heeger, "25th anniversary article: Bulk heterojunction solar cells: Understanding the mechanism of operation," *Adv. Mater.*, vol. 26, no. 1, pp. 10–28, 2014.
- [45] M. Zhang, H. Wang, and C. W. Tang, "Effect of the highest occupied molecular orbital energy level offset on organic heterojunction photovoltaic cells," *Appl. Phys. Lett.*, vol. 97, no. 14, 2010.
- [46] Y. Min Nam, J. Huh, and W. Ho Jo, "Optimization of thickness and morphology of active layer for high performance of bulk-heterojunction organic solar cells," *Sol. Energy Mater. Sol. Cells*, vol. 94, no. 6, pp. 1118–1124, 2010.
- [47] J.-L. Bredas, J. E. Norton, J. Cornil, and V. Coropceanu, "Molecular Understanding of Organic Solar Cells: Introduction," *Accounts Chem. Res.*, vol. 42, no. 11, pp. 1691–1699, 2009.
- [48] Y. Zhu, R. D. Champion, and S. A. Jenekhe, "Conjugated donor-acceptor copolymer semiconductors with large intramolecular charge transfer: Synthesis, optical properties, electrochemistry, and field effect carrier mobility of thienopyrazine-based copolymers," *Macromolecules*, vol. 39, no. 25, pp. 8712–8719, 2006.
- [49] P. Peumans and S. R. Forrest, "Separation of geminate charge-pairs at donor-acceptor interfaces in disordered solids," *Chem. Phys. Lett.*, vol. 398, no. 1–3, pp. 27–31, 2004.
- [50] M. H. Jao, H. C. Liao, and W. F. Su, "Achieving a high fill factor for organic solar cells," *J. Mater. Chem. A*, vol. 4, no. 16, pp. 5784–5801, 2016.
- [51] H. A. McCartney and M. H. Unsworth, "Spectral distribution of solar radiation. I: Direct radiation," *Q. J. R. Meteorol. Soc.*, vol. 104, no. 441, pp. 699–718, 1978.
- [52] S. R. Cowan, A. Roy, and A. J. Heeger, "Recombination in polymer-fullerene bulk heterojunction solar cells," *Phys. Rev. B - Condens. Matter Mater. Phys.*, vol. 82, no. 24, 2010.
- [53] J. C. Blakesley and D. Neher, "Relationship between energetic disorder and open-circuit voltage in bulk heterojunction organic solar cells," *Phys. Rev. B - Condens. Matter Mater. Phys.*, vol. 84, no. 7, 2011.

- [54] Y. Gao, M. Liu, Y. Zhang, Z. Liu, Y. Yang, and L. Zhao, "Recent development on narrow bandgap conjugated polymers for polymer solar cells," *Polymers (Basel)*, vol. 9, no. 2, 2017.
- [55] B. Qi and J. Wang, "Open-circuit voltage in organic solar cells," *J. Mater. Chem.*, vol. 22, no. 46, pp. 24315–24325, 2012.
- [56] W. Ananda, "External quantum efficiency measurement of solar cell," in *QiR 2017 - 2017 15th International Conference on Quality in Research (QiR): International Symposium on Electrical and Computer Engineering*, 2017, vol. 2017–Decem, pp. 450–456.
- [57] H. C. Chen, Y. H. Chen, C. C. Liu, Y. C. Chien, S. W. Chou, and P. T. Chou, "Prominent short-circuit currents of fluorinated quinoxaline-based copolymer solar cells with a power conversion efficiency of 8.0%," *Chem. Mater.*, vol. 24, no. 24, pp. 4766–4772, 2012.
- [58] X. Xu, Y. Wu and J. Fang, "Side-Chain Engineering of Benzodithiophene-Fluorinated Quinoxaline Low-Band-Gap Co-polymers for High-Performance Polymer Solar Cells," *Chem. - A Eur. J.*, vol. 20, no. 41, pp. 13259–13271, 2014.
- [59] D. Liu, W. Zhao and S. Zhang, "Highly Efficient Photovoltaic Polymers Based on Benzodithiophene and Quinoxaline with Deeper HOMO Levels," *Macromolecules*, vol. 48, no. 15, pp. 5172–5178, 2015.
- [60] Y. Sun, C. Zhang and B. Dai, "Side chain engineering and conjugation enhancement of benzodithiophene and phenanthrenequinoxaline based conjugated polymers for photovoltaic devices," *J. Polym. Sci. Part A Polym. Chem.*, vol. 53, no. 16, pp. 1915–1926, 2015.
- [61] N. Chakravarthi K. Kranthiraja and M. Song, "New alkylselenyl substituted benzodithiophene-based solution-processable 2D  $\pi$ -conjugated polymers for bulk heterojunction polymer solar cell applications," *Sol. Energy Mater. Sol. Cells*, vol. 122, pp. 136–145, 2014.





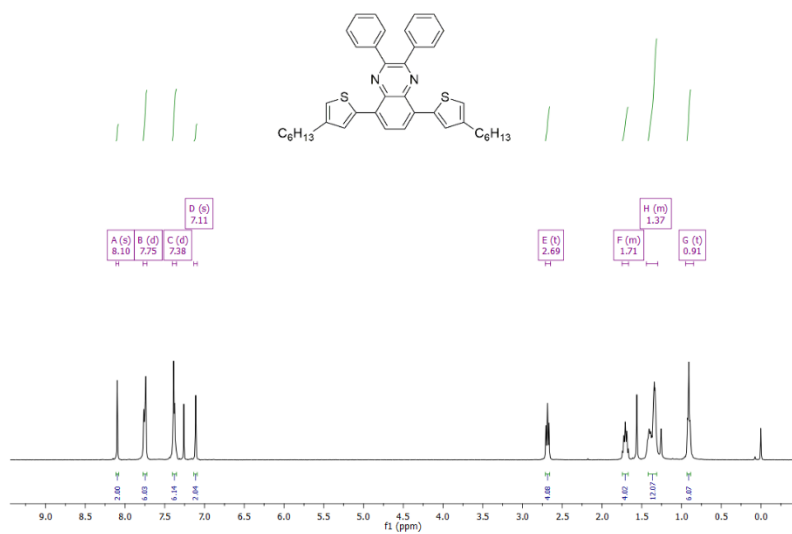


**Figure A.3.** <sup>1</sup>H NMR result of 5,8-bis(4-hexylthiophen-2-yl)-2,3-diphenylquinoxaline

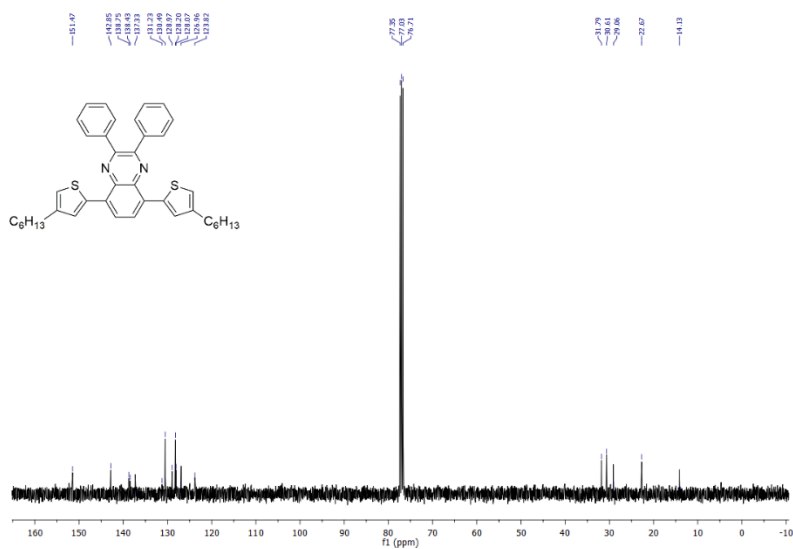


**Figure A.4.** <sup>13</sup>C NMR result of 5,8-bis(4-hexylthiophen-2-yl)-2,3-diphenylquinoxaline

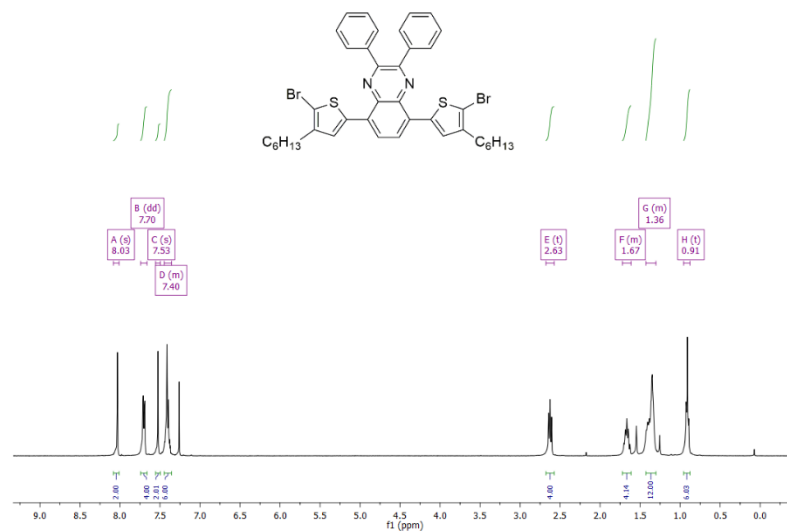


**Figure A.5.**  $^1\text{H}$  NMR result of 5,8-bis(5-bromo-4-hexylthiophen-2-yl)-2,3 diphenylquinoxaline

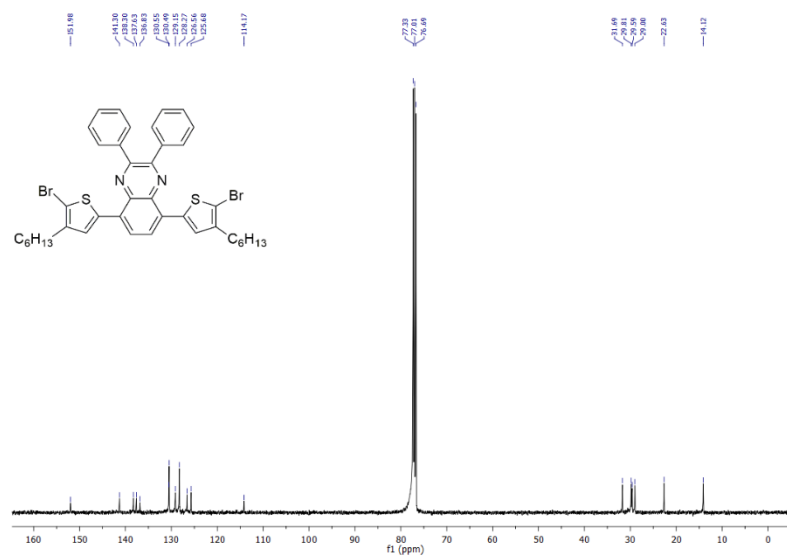


**Figure A.6.**  $^{13}\text{C}$  NMR result of 5,8-bis(5-bromo-4-hexylthiophen-2-yl)-2,3 diphenylquinoxaline

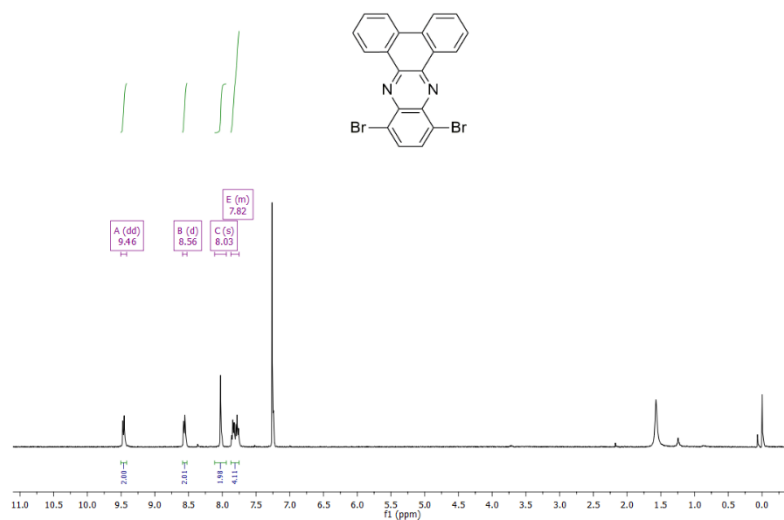


**Figure A.7.**  $^1\text{H}$  NMR result of 10,13-dibromodibenzo[a,c]phenazine

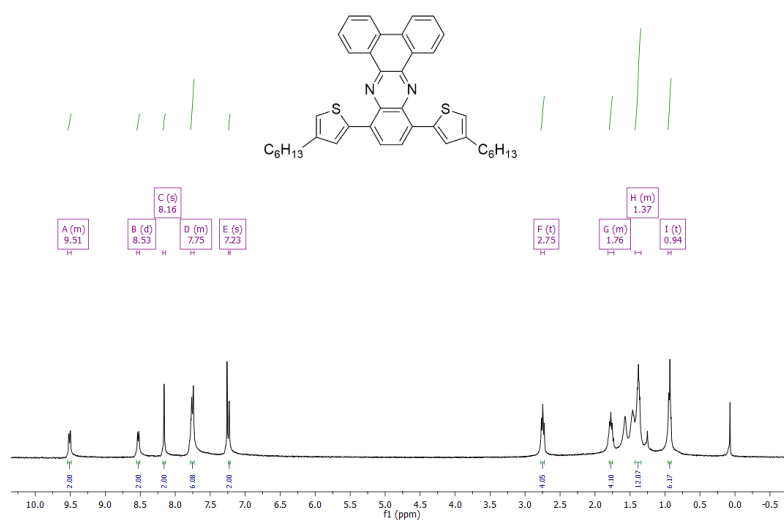


**Figure A.8.**  $^1\text{H}$  NMR result of 10,13-bis(4-hexylthiophen-2-yl)dibenzo[a,c]phenazine

ne

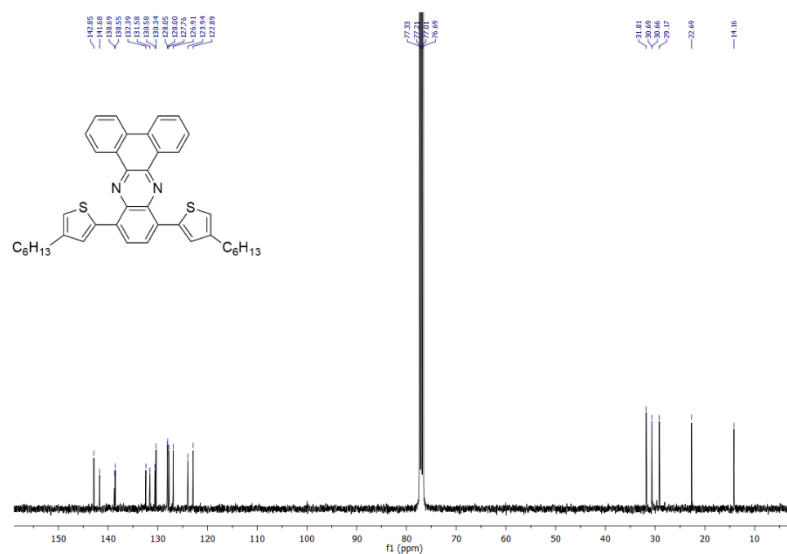


**Figure A.9.** <sup>13</sup>C NMR result of 10,13-bis(4-hexylthiophen-2-yl)dibenzo[a,c]phenazine

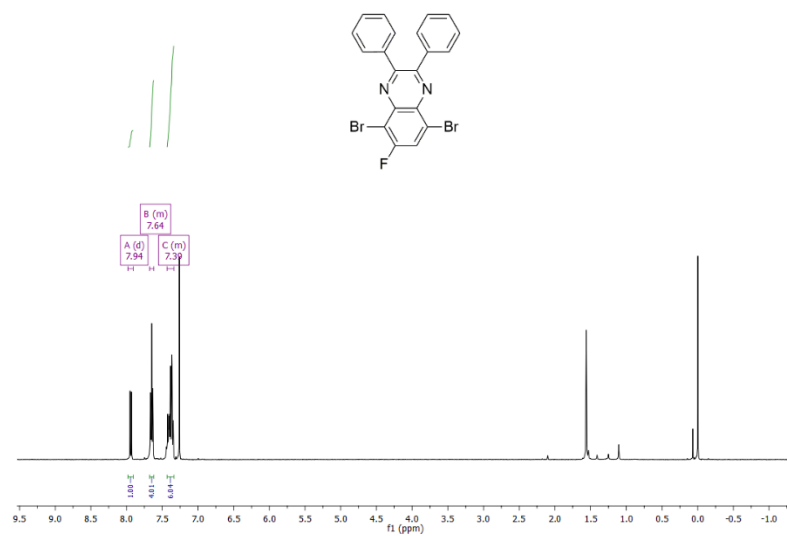


**Figure A.10.** <sup>1</sup>H NMR result of 5,8-dibromo-6-fluoro-2,3-diphenylquinoxaline

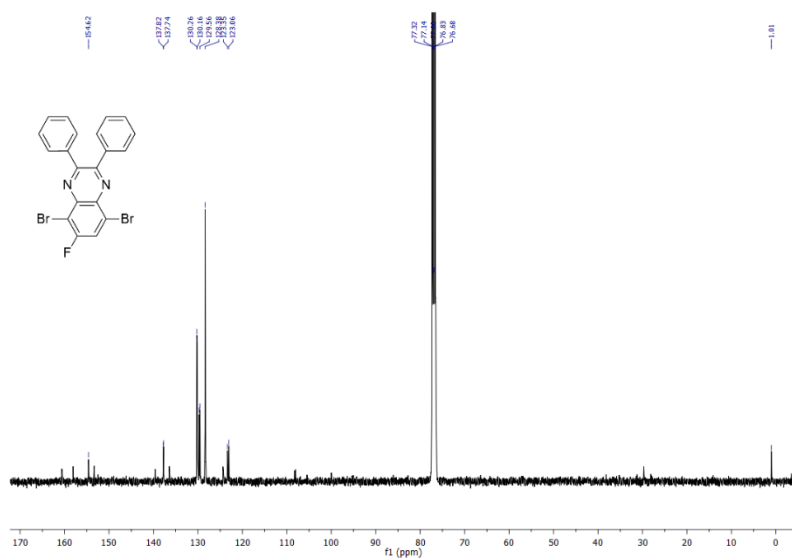


**Figure A.11.**  $^{13}\text{C}$  NMR result of 5,8-dibromo-6-fluoro-2,3-diphenylquinoxaline

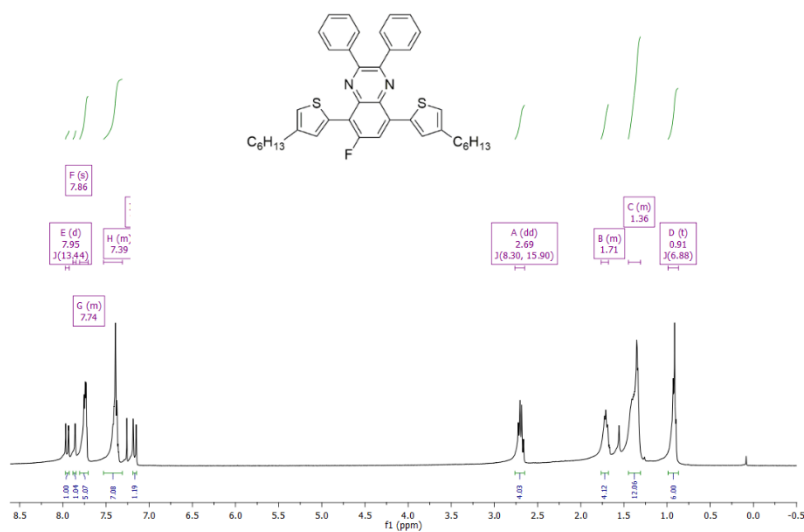


**Figure A.12.**  $^1\text{H}$  NMR result of 5,8-bis(4-hexylthiophen-2-yl)-6-fluoro-2,3-diphenylquinoxaline



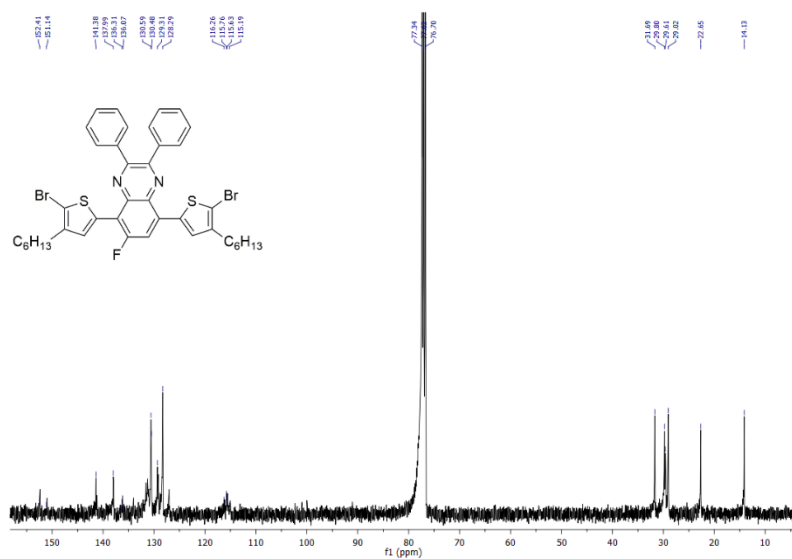


**Figure A.15.**  $^{13}\text{C}$  NMR result of 5,8-bis(5-bromo-4-hexyl-2yl)-6-fluoro-2,3-diphenyl quinoxaline

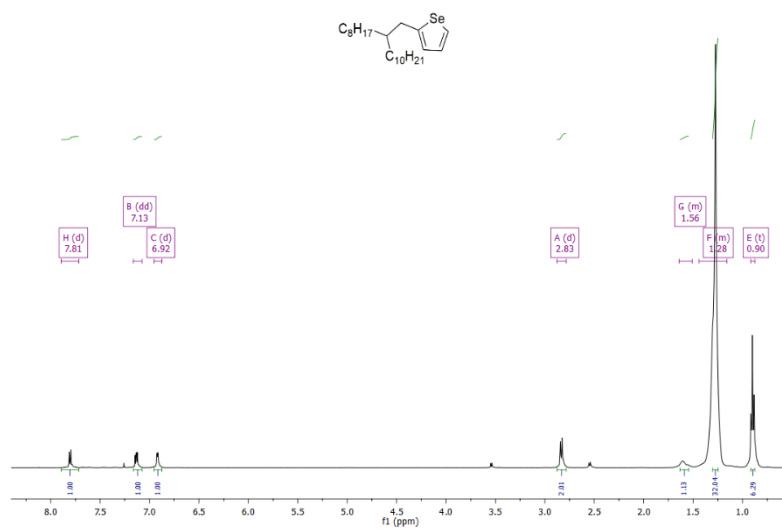


**Figure A.16.**  $^1\text{H}$  NMR result of 2-(2-octyldodecyl)selenophene

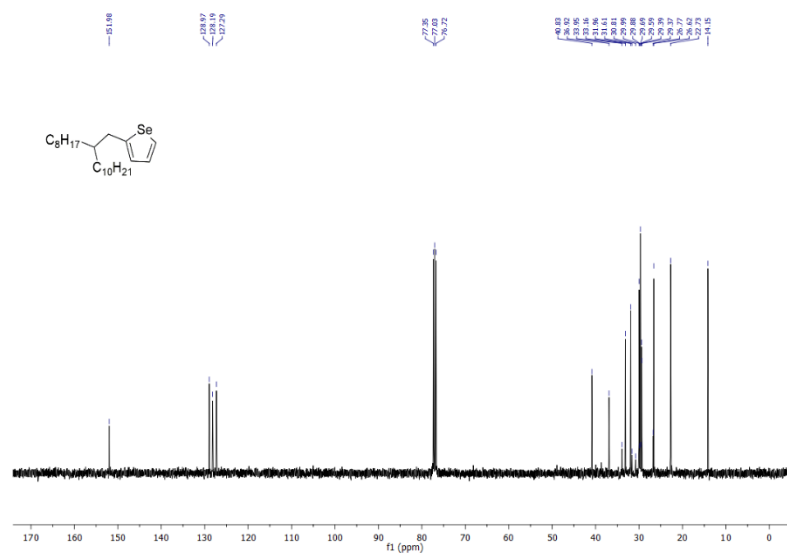


Figure A.17.  $^{13}\text{C}$  NMR result of 2-(2-octyldodecyl)selenophene

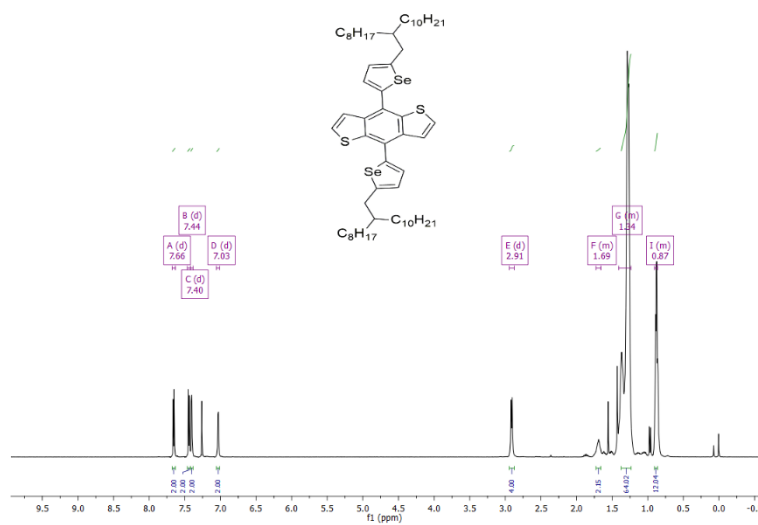
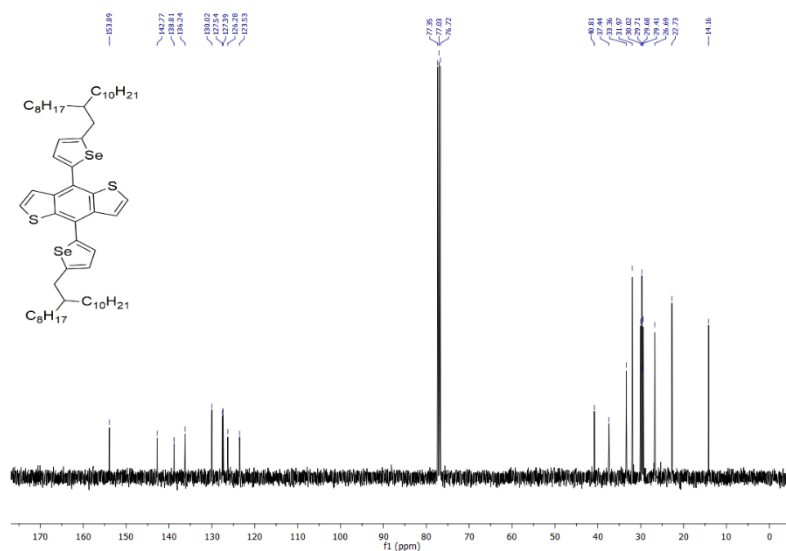
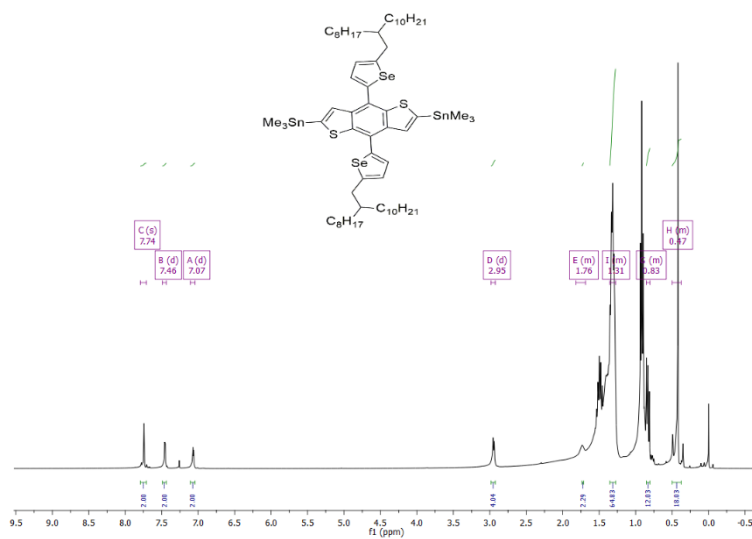


Figure A.18.  $^1\text{H}$  NMR result of 4,8-bis(5(2-octyldodecyl)selenophen-2-yl)benzo[1,2-b:4,5-b'] dithiophene



**Figure A.19.**  $^{13}\text{C}$  NMR result of 4,8-bis(5(2-octyldodecyl)selenophen-2-yl)benzo [1,2-b:4,5-b']dithiophene



**Figure A.20.**  $^1\text{H}$  NMR result of 4,8-bis(5(2-octyldodecyl)selenophen-2-yl)benzo [1,2-b:4,5-b'] dithiophene-2,6-diylbis(trimethylstannane)

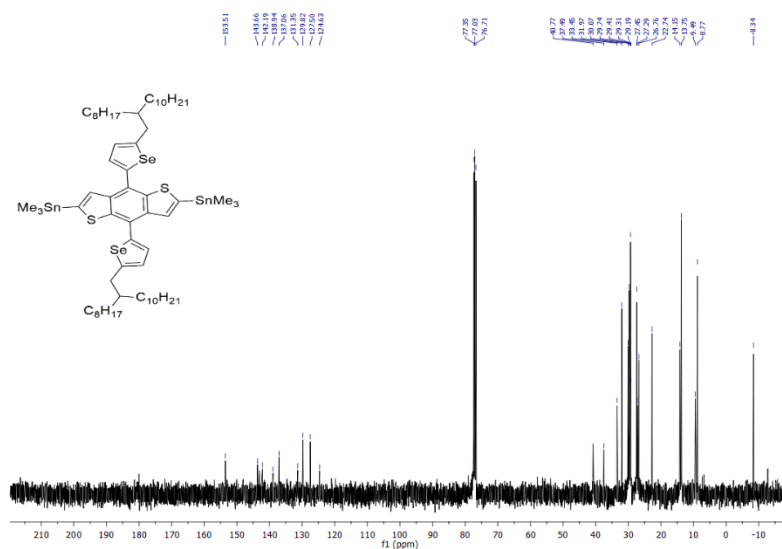


**Figure A.21.**  $^{13}\text{C}$  NMR result of 4,8-bis(5(2-octyldodecyl) selenophen-2-yl) benzo [1,2-b:4,5-b'] dithiophene-2,6-diyl bis(trimethylstannane)

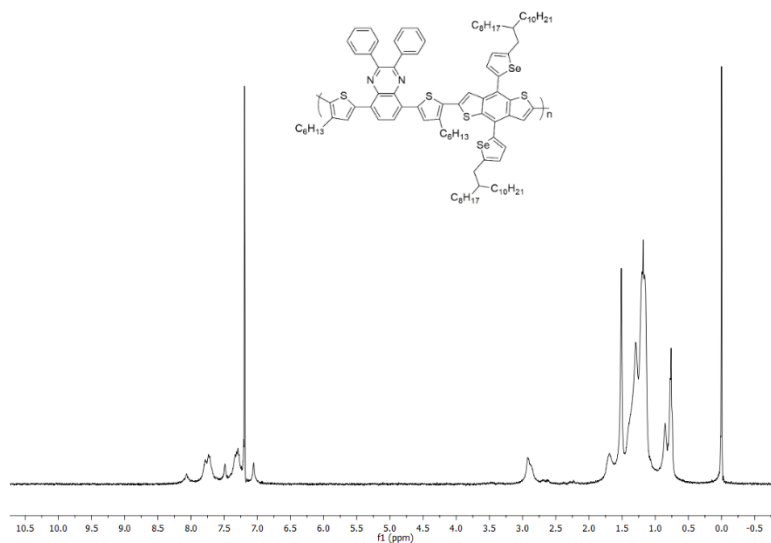


**Figure A.22.**  $^1\text{H}$  NMR result of P1

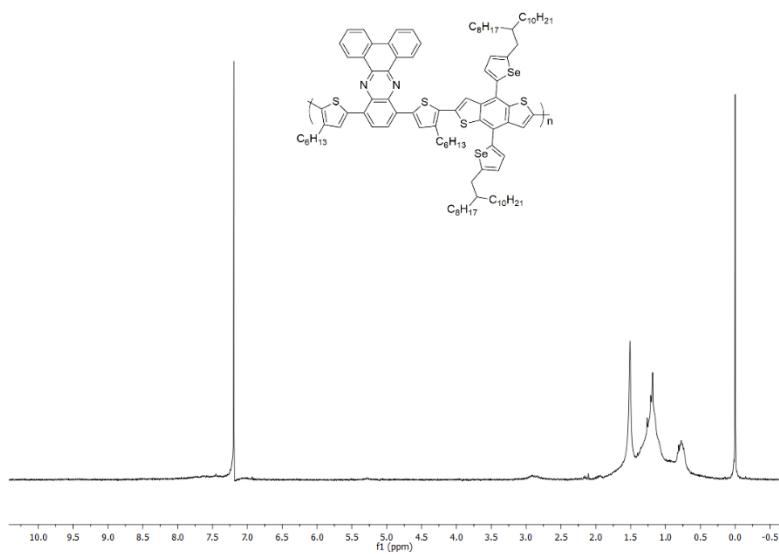


**Figure A.23.** <sup>1</sup>H NMR result of P2

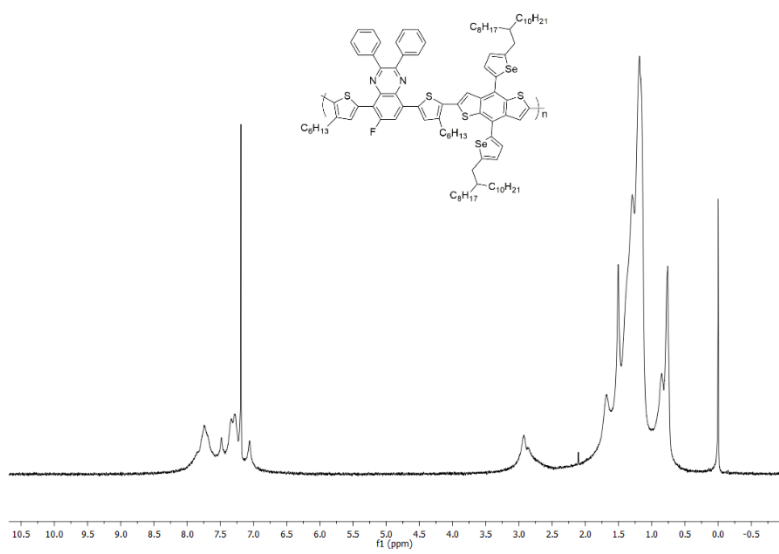


**Figure A.24.** <sup>1</sup>H NMR result of P3

## B. THERMAL ANALYSIS RESULTS

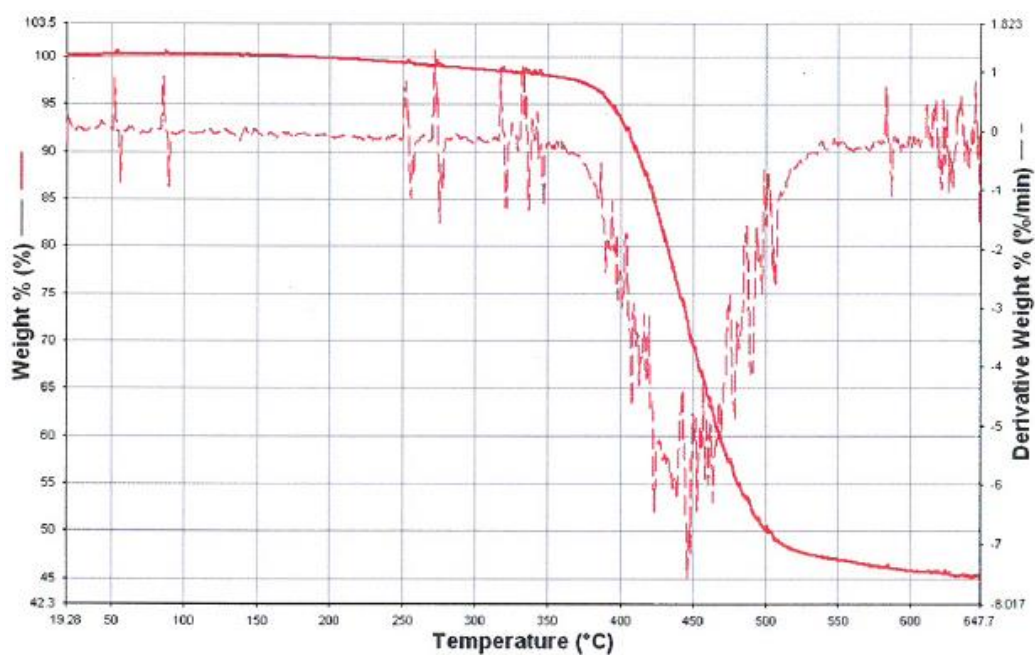


Figure A.25. Thermal studies derived from TGA for P1

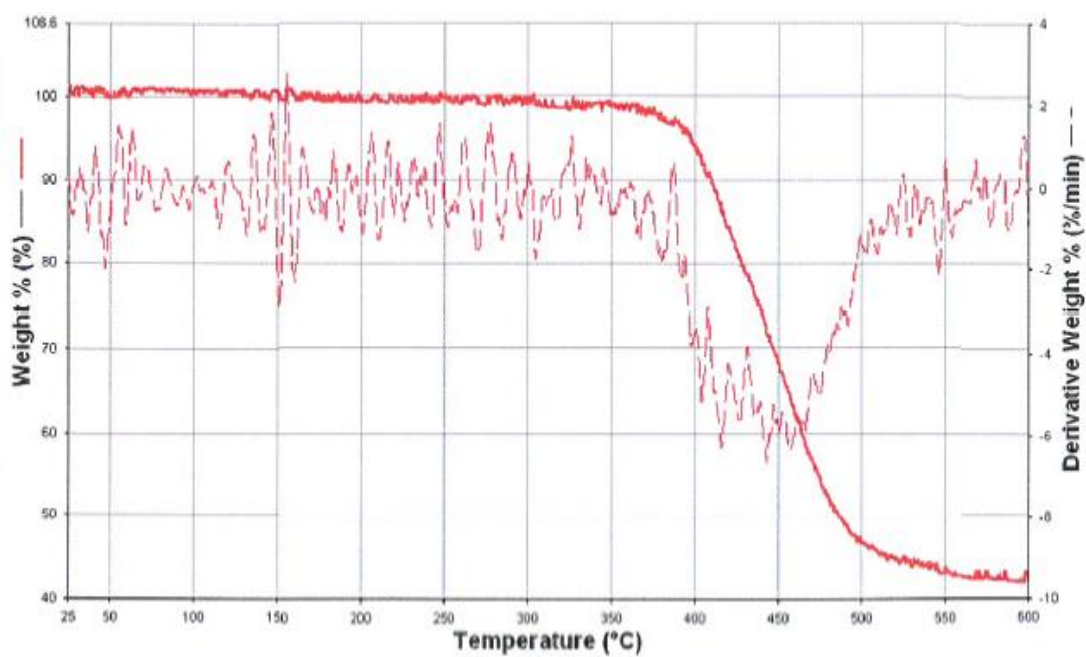
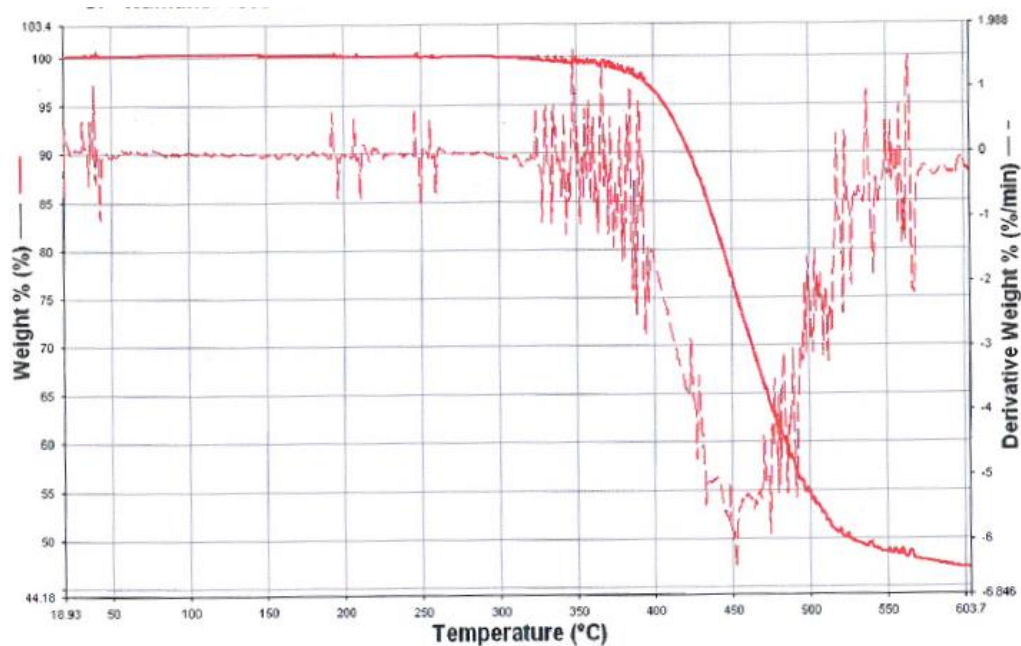
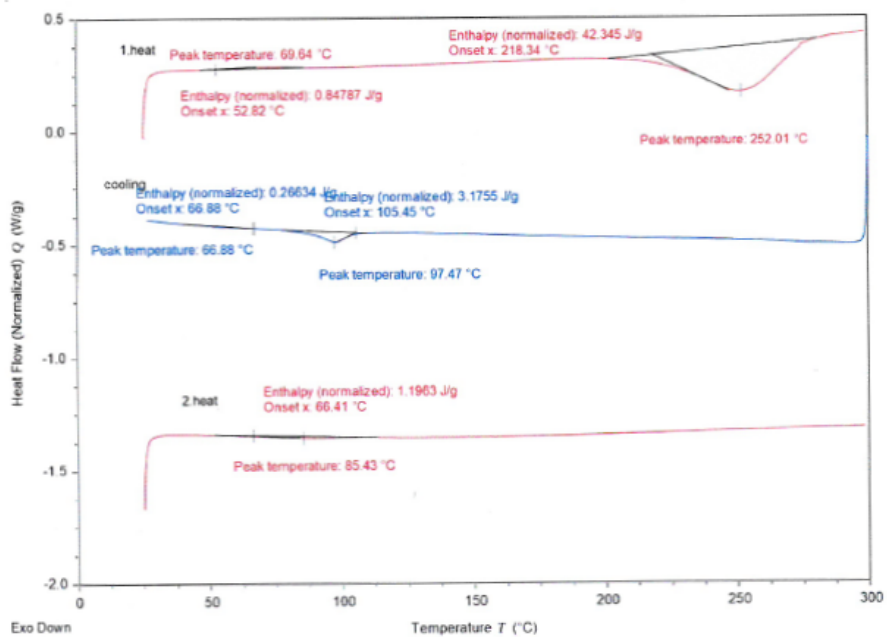


Figure A.26. Thermal studies derived from TGA for P2



**Figure A.27.** Thermal studies derived from TGA for P3



**Figure A.28.** Thermal studies derived from DSC analysis for P1

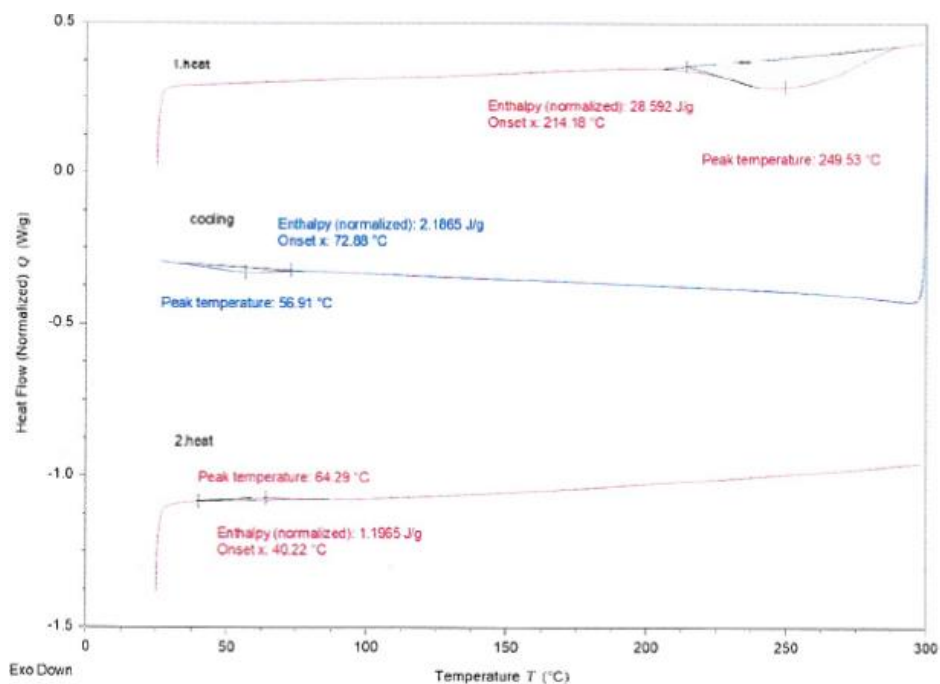


Figure A.29. Thermal studies derived from DSC analysis for P2

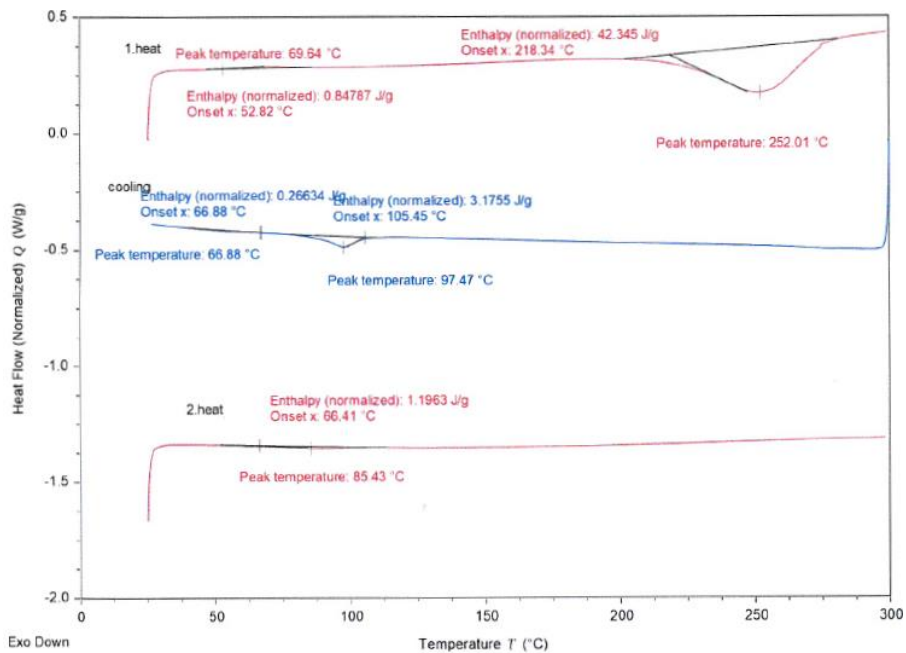


Figure A.30. Thermal studies derived from DSC analysis for P3